Contents

List of Figures

List of Tables

Todo list

Chapter 1

The secrets of nature

This chapter attempts to understand the world around us using a mathematical framework which describes the matter and its interaction. Firstly, the laws that rule the Universe will be presented. Then, it will focus on the mathematical framework itself with the description of three interactions: the electromagnetic interaction (EM), the weak and the strong interaction. Afterward, a framework that unifies the EM and weak interaction, as well as the spontaneous symmetry breaking will be studied. Finally, the limits of this theory and the possible solution to overcome these issues will be tackled.

Contents

1.1 The Standard Model

1.1.1 Introduction

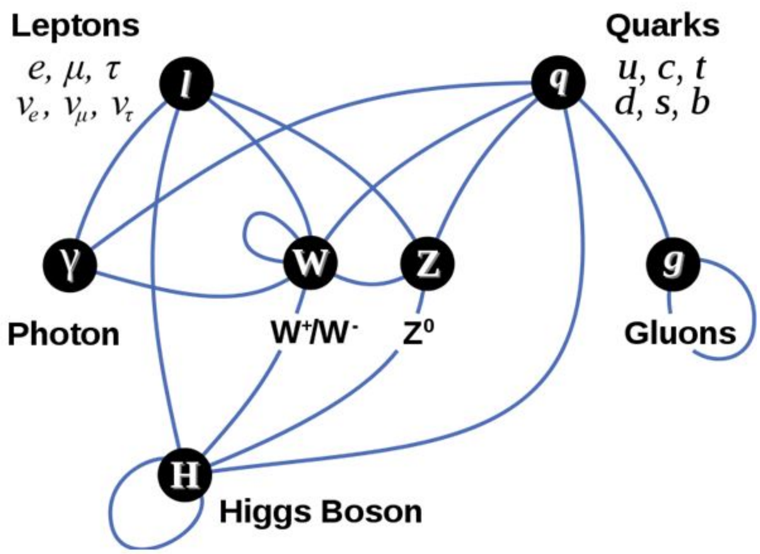

Figure 1.1 – Summary of the Standard Model particles with their interactions[41].

The Standard Model (SM) is a theory that describes the elementary structure of the matter. It is one of the most successful achievements in modern physics. The elegant theoretical framework of the SM is able to explain experimental results but is also able to predict a wide variety of phenomena. It depicts the interactions between the fundamental constituents of matter, called elementary particles. A quantum formalism describes an elementary particle with a set of quantum numbers, that are the spin, or the intrinsic angular momentum, the parity P, the electric charge...The distinction between the 'matter' particles and the 'force carrier' particles is done thanks to the quantum numbers.

Keep going to introduce all the quantum numbers

The half-integer spin particles obey to the Fermi-Dirac statistics and are submitted to the Pauli exclusion principle: they can not occupy the same quantum state at the same time. These particles are called fermions. They are the constituents of the matter and are to the number of twelve.

The fermions are divided into two categories: the leptons and the quarks. The leptons are to the number of six: three charged particles and three neutral particles called neutrino. The first fundamental particle discovered in particle physics was the electron (e^-) at the end of the 19$^{\text{th}}$ century. The two other charged leptons were discovered in 1937 for the muon (μ) and in 1975 for the tau (τ). Three neutrinos are associated to the three flavored leptons: the electron neutrino (ν_e) discovered in 1953, the muon neutrino (ν_μ) in 1962[18] and the tau neutrino (ν_τ) discovered in 2000[13].

The quarks are to the number of six. They can not be found alone in nature. They are carrying a quantum number: the color. The color quantum numbers are green, blue and red (and the anti-color associated). They are always in a bounded state to form composite particles that are colorless and are called hadrons. A quark and an anti-quark form an integer spin composite particle, called a meson. Three quarks bounded together are called baryons. The most known baryons are the proton and the neutron. They are made of the up quarks (u) and the down quarks (d). The other quarks were discovered in the second half of the 20$^{\text{th}}$ century. The strange quark (s) was discovered in 1968, followed by the charm quark (c) in 1974. Then, the bottom quark or beauty quark (b) was discovered in 1977. The last quark discovered was the top quark (t) in 1995.

The fermions are thus divided into three categories which depend on the mass of the particle. They are called generations. The first generation of particles is composed of the electron, the electron neutrino, the u and d quarks. They form the ordinary matter. The two other generations are particles found in cosmic rays or in collisions with accelerators. All the fermions and their properties are summarised in the table 1.1.

The second kind of particles are integer spins particles and are called bosons or gauge bosons. They follow the Bose-Einstein statistics. Contrary to the fermions, the bosons are not limited to a single occupancy of the same sate. The bosons are the mediators of the fundamental interactions.

The EM is mediated by the photon γ, a massless and chargeless particle of spin 1. The EM is responsible for the interaction between two charged particles. The weak interaction which is responsible for the β radioactive decay (a nucleon decays into another one with the emission of a lepton and a neutrino). The gauge bosons associated with the weak interaction are the neutral electrical charged boson Z^0, and two electrical charged one: the W^+ and W^- bosons. The strong interaction is mediated by eight gauge bosons:

Type	Family	Particle	L	B	Q_e	Mass (MeV)
Leptons	1^{st}	e	1	0	-1	0.511
		ν_e	1	0	0	$< 2 \times 10^{-6}$
	2^{nd}	μ	1	0	-1	105.66
		ν_μ	1	0	0	$< 2 \times 10^{-6}$
	3^{rd}	τ	1	0	-1	1.78×10^3
		ν_τ	1	0	0	$< 2 \times 10^{-6}$
Quarks	1^{st}	u	0	1	2/3	$2.3^{+0.7}_{-0.5}$
		d	0	1	-1/3	$4.8^{+0.5}_{-0.3}$
	2^{nd}	s	0	1	-1/3	95 ± 5
		c	0	1	2/3	$1.275 \times 10^3 \pm 2.5$
	3^{rd}	b	0	1	-1/3	$4.66 \times 10^3 \pm 30$
		t	0	1	2/3	$173.21 \times 10^3 \pm 511 \pm 711$

Table 1.1 – Summary of the 12 types fermions. L is a quantum number associated to the leptons. Its value is 1 for leptons and -1 for anti-leptons. B is a quantum number associated to the baryons. It is equal to 1 for a baryon and to -1 for an anti-baryon. [36]

the gluons. The cohesion of the hadrons and the cohesion of the atom's nucleus is lead by the strong interaction. The last force is the gravitational interaction but it is not included into the SM. Trying to find a framework where the equation of the general relativity used to describe the macroscopic world and the equation of the quantum mechanics describing the microscopic world is a difficult challenge. A quantum theory intends to associate a boson to the gravitational force. This boson is a spin 2 particle and is called graviton.

The Higgs boson (H) is a particle predicted by the SM and has been discovered in 2012 at the Large Hadron Collider (LHC) It is the gauge boson of the Higgs mechanism. This mechanism is the mass generator of particles and is presented in section 1.2.2.

The table 1.2 summarises the different bosons of the SM.

Conservation laws and invariance

The particle physics is based on the conservation laws as well as the invariance. The invariance means that the physics is the same on every point of the Universe. For example, the speed of light is always ~ 3.0 m.s^{-1}.

Force	Gauge bosons	Mass (GeV/c^2)	Electric charge	Range
Electromagnetic	γ	0	0	∞
Weak	Z^0	91.1876 $\pm$ 0.0021	0	10^{-18} m
	$W^\pm$	80.3980 $\pm$ 0.0250	±1	
Strong	g (8 gluons)	0	0	10^{-15} m
	H	125 GeV	0	

Table 1.2 – Summary of the interactions and the bosons defined in the Standard Model[36]. The range corresponds to the distance on which the interaction is still effective. As the gravitational interaction is not part of the SM, the graviton is not included in this table.

1.1.2 Quantum Field Theory

The mathematical basis of the SM is the Quantum Field Theory (QFT). All the interactions are described by the gauge group:

$$SU_C(3) \otimes SU_L(2) \otimes U_Y(1). \tag{1.1}$$

The gauge theory is invariant under a continuous set of local transformation. Taking the gauge symmetries and the least action into account, physicists were able to set up equations that describe the dynamic of the interactions by a Lagrangian. The steps to build Lagrangian for the three forces and the unification of the EM and weak interactions are going to be presented.

Subsubsection: symmetries

Quantum Electrodynamic

The Quantum Electrodynamic (QED) is the QFT that combines the electromagnetism and the quantum mechanics formalisms to describe the interaction thanks to a relativistic Lagrangian. As the charge Q_e of the electron is invariant on every part of the Universe, the QED Lagrangian should be invariant under some transformations too. The $U(1)$ gauge group is a unitary group of one dimension which is invariant under space transformations.

Firstly, the Dirac Lagrangian $\mathcal{L}_{Dirac}$ for a free fermion with a mass m is:

$$\mathcal{L}_{Dirac} = \overline{\Psi}(x)\left(i\gamma^\mu\partial_\mu - m\right)\Psi(x)\,, \tag{1.2}$$

with $\Psi(x)$ the spinor field describing the fermion and γ^{μ} are the Dirac matrices. The Lagrangian is invariant under global $U(1)$ transformation:

$$\begin{aligned} \Psi(x) &\rightarrow \Psi'(x) = e^{-i\alpha}\Psi(x) \\ \overline{\Psi}(x) &\rightarrow \overline{\Psi}'(x) = e^{i\alpha}\overline{\Psi}(x) \end{aligned} \tag{1.3}$$

The corresponding local symmetry is:

$$\begin{aligned} \Psi(x) &\rightarrow \Psi'(x) = e^{-i\alpha(x)}\Psi(x) \\ \overline{\Psi}(x) &\rightarrow \overline{\Psi}'(x) = e^{i\alpha(x)}\overline{\Psi}(x) \end{aligned} \tag{1.4}$$

Although the mass term of the Lagrangian in the equation 1.2 stays invariant under the local symmetry, the term containing a partial derivative is not anymore. A gauge field A_{μ} has to be added to the derivative to keep it invariant under local gauge transformation. The covariant derivative will be then:

$$D_{\mu}\Psi(x) = (\partial_{\mu} - iQ_e A_{\mu})\Psi(x) \tag{1.5}$$

The gauge field is not yet a dynamic field. To get a physical gauge field, a kinetic term should be added to the equation. This gauge invariant term that includes derivative from the A_{μ} field is:

$$F_{\mu\nu} = \partial_{\mu}A_{\nu} - \partial_{\nu}A_{\mu} \tag{1.6}$$

The Lagrangian, which is local invariant, is the one that describes the QED:

$$\mathcal{L}_{QED} = \overline{\Psi}(x)(i\gamma^{\mu}D_{\mu} - m)\Psi(x) - \frac{1}{4}F_{\mu\nu}(x)F^{\mu\nu}(x) \tag{1.7}$$

A mass term $mA_{\mu}A^{\mu}$ for the field A_{μ} is missing because it is not gauge invariant. That consideration matches to the fact that the photon is a massless boson.

Add details on the QED: coupling...

Weak interaction

In 1930, Pauli assumed that the continuous energy spectrum of the electron in the β decay could be explained by the existence of a new particle to respect the principle of energy conservation. It is a light particle, which does not interact so much with matter.

After the discovery of the neutron by Chadwick in 1932, Fermi wrote a theory on weak interaction to explain the β decay. [19] He postulated that the neutron is decaying into a proton by emitting an electron and a light neutral particle, called neutrino. In analogy to the electromagnetism, he proposed a current-current Lagrangian to describe the β decay.

$$\mathcal{L}_{weak} = \frac{G_F}{\sqrt{2}} \left(\overline{p}\gamma_\mu n\right) \left(\overline{e}\gamma_\mu \nu\right) \tag{1.8}$$

where the G_F is the Fermi constant $G_F = 1.166\dot{1}0^{-5} GeV^{-2}$.

Nevertheless, the non-relativistic limit leads to an incomplete theory. The interaction considered with a 2-components spinor transforms a proton into a neutron without changing the position, the spin or the parity. However, Lee and Yang have postulated in 1956 that the weak interactions violate the parity after analysing the decays of the τ and θ particles [30]. The Wu experiment [44] confirmed this hypothesis in 1957 by studying the decay of ^{60}Co.

The Fermi interaction was modified by Feynman and Gell-Mann[20] to a $V - A$ theory[1]. The vector current is now subtracted by an axial vector current. For example, the neutrino current is replaced by:

$$\begin{aligned} \overline{e}(x)\gamma_\mu\nu \quad \rightarrow \quad & \overline{e}\gamma_\mu(1-\gamma_5)\nu \\ & = \overline{e}\gamma_\mu\nu - \overline{e}\gamma_\mu\gamma_5\nu \end{aligned} \tag{1.9}$$

It was established that the weak current has the form $V - A$ instead of $V + A$. The weak interaction is only coupling left-handed particles and right-handed anti-particles.

The lagrangian describing the weak interactions can be written as a currents interaction:

$$\mathcal{L}_{weak} = -\frac{G_F}{\sqrt{2}} J^\mu J^\dagger_\mu \tag{1.10}$$

[1] V stands for vector and A for axial-vector

and J^{μ} is a combination of leptonic and hadronic currents.

Contrary to the QED, the weak interaction obeys to a non-Abelian symmetry group[2], the SU(2) symmetry group. The matter field could be represented as a doublet Ψ_L and a singlet Ψ_R of this group.

$$\Psi_L = \begin{pmatrix} \nu_{eL} \\ e_L \end{pmatrix}, \quad \Psi_R = e_R \tag{1.11}$$

The generators of the group are the three Pauli matrices σ_i, associated with a gauge field W^i_μ. The bosons of the weak interactions are the $W^\pm$ and Z.

As the left-handed leptons are combined into a doublet, a quantum number called weak isospin (I_3) is associated with them. The charged leptons have a weak isospin $I_3 = \frac{-1}{2}$ and for the neutrinos $I_3 = \frac{1}{2}$. Concerning the gauge bosons $W^\pm$ and Z, the weak isospin is respectively $I_3 = \pm 1, 0$.

Quantum Chromodynamics

The Quantum Chromodynamics (QCD) is the quantum field theory of the strong interaction. In this model, the interaction is due to an $SU(3)$ gauge group. It produces 8 gauge fields called gluons. The spinors of this theory are the six quarks that form a triplet with respect to the gauge symmetry.

The SU(3) gauge group is a group of $9 - 1 = 8$ real parameters and of 8 generators. Those generators are the Gell-Mann matrices. The normalised generators are defined by:

$$T^a = \frac{1}{2}\lambda^a \tag{1.12}$$

The structure constant f^{abc} can be expressed as:

$$if^{abc} = 2Tr([T^a, T^b]T^c) \tag{1.13}$$

Each of them is considered as a triplet state with respect to the SU(3) group:

[2] A group is non-Abelian when the elements of the group are not commutating.

$$q_i = \begin{pmatrix} q_i^1 \\ q_i^2 \\ q_i^3 \end{pmatrix} \tag{1.14}$$

where q_i are the six quarks. These quarks can appear in three different states, called color and that are named red, blue and green.

The local gauge symmetry U(1) should be included into the SU(3) group.

The gauge field A_μ can be introduced in the group:

$$A_\mu = g_S A_\mu^a \frac{\lambda^a}{2} \tag{1.15}$$

with a = 1,...,8 and corresponds to the 8 gluons. A mass term $m_g A_a^\mu A_\mu^a$ would not be gauge invariant, it implies that the gluons have to be massless.

The covariant derivative is then:

$$\begin{aligned} D_\mu &= \partial_\mu - iA_\mu \\ &= \partial_\mu - ig_S A_\mu^a \tfrac{\lambda^a}{2} \end{aligned} \tag{1.16}$$

The QED field $F_{\mu\nu}$ is not gauge invariant in QCD. Nevertheless, an additional term to obtain gauge invariant field tensor can be introduced:

$$G_{\mu\nu}^a = \left(\partial_\mu A_\nu^a - \partial_\nu A_\mu^a\right) + g_S f^{abc} A_\mu^b A_\nu^c \tag{1.17}$$

Finally, the QCD Lagrangian is given by:

$$\mathcal{L} = \sum_{i=1}^{6} \bar{q}_i \left(i\gamma^\mu D_\mu - m_i\right) q_i - \frac{1}{4} G_{\mu\nu}^a G_a^{\mu\nu} \tag{1.18}$$

1.2 The Glashow-Weinberg-Salam model

Rephrase the section title

Late 1960, a model of unification was postulated by Glashow, Weinberg, and Salam to describe the electroweak interaction (EW). The theory rests on a $SU(2)_L \otimes U(1)_Y$ symmetry group. It is the simplest group which conserves the properties of EM charge conversion and parity violation of weak interaction.

For the EW unification, the $U(1)_{EM}$ symmetry group describing the EM has to be rewritten. As the fermions are considered by left-handed doublets and right-handed singlets, the $U(1)_{EM}$ breaks the gauge invariance. The weak isospin group $SU(2)_L$ is combined with the EM charge to create the hypercharge give by the Gell-Mann-Nishijima relation:

$$Q = I_3 + \frac{1}{2}Y \tag{1.19}$$

The I_3 term is the third component of the weak isospin. With the introduction of the hypercharge, the EM gauge invariance is conserved.

The EW Lagrangian is:

$$\mathcal{L}_{EW} = \mathcal{L}_{YM} + \mathcal{L}_{fermions}\textbf{??} \tag{1.20}$$

The first term $\mathcal{L}_{YM}$ is the Yang-Mills Lagrangian that describes the bosons gauges interactions (kinetic term + interaction between bosons). It has the form below:

$$\mathcal{L}_{YM} = -\frac{1}{4}\mathbf{W}^a_{\mu\nu}\mathbf{W}^{a\mu\nu} - \frac{1}{4}\mathbf{B}_{\mu\nu}\mathbf{B}^{\mu\nu} \tag{1.21}$$

With

$$\mathbf{W}_{\mu\nu} = \partial_\mu \mathbf{W}_\nu - \partial_\nu \mathbf{W}_\mu - ig[\mathbf{W}_\mu, \mathbf{W}_\nu] \tag{1.22}$$

$$\mathbf{B}_{\mu\nu} = \partial_\mu \mathbf{B}_\nu - \partial_\nu \mathbf{B}_\mu \tag{1.23}$$

In the equation 1.22, $\mathbf{W}_\mu = \sum W^i_\mu \sigma^i/2$ is a vector of three gauge fields associated to $SU(2)_L$ and σ^i are the Pauli matrices. The term $[\mathbf{W}_\mu, \mathbf{W}_\nu]$ is associated to the interactions between the gauge fields. In the equation 1.23, $\mathbf{B}_\mu$ is the only gauge field associated to the $U(1)_Y$.

The Lagrangian describing the fermions field is given by:

$$\mathcal{L}_{fermions} = \overline{\Psi}_L \gamma^\mu D_\mu \Psi_L + \overline{\Psi}_R \gamma^\mu D_\mu \Psi_R \tag{1.24}$$

With $D_\mu \Psi_L = \left(\partial_\mu + ig\mathbf{W}_\mu - i\frac{g'}{2}Y\mathbf{B}_\mu\right)\Psi_L$ and $D_\mu \Psi_R = \left(\partial_\mu - i\frac{g'}{2}Y\mathbf{B}_\mu\right)\Psi_R$ (1.25)

In the equation 1.25, the covariant derivative has two forms. The weak interaction does not allow coupling of the W bosons to right-handed fermions whereas the γ and Z bosons do.

With the EW Lagrangian described above, the gauge bosons are considered as massless fields. The electroweak interaction does not allow a $m\overline{\Psi}\Psi$ term because it does not transform as a scalar under $SU(2)_L \otimes U(1)_Y$. Moreover, the $m^2 \mathbf{W}_\mu \mathbf{W}^\mu$ violates the $SU(2)_L$ gauge invariance of the Lagrangian. The mass terms associated with the physical fields of the gauge bosons are given by spontaneous symmetry breaking via the Higgs mechanism.

1.2.1 Symmetry Breaking mechanism and Goldston theorem

Before introducing the Higgs mechanism, we will study the spontaneous symmetry breaking for a global symmetry. This phenomenon is also seen in phase transitions or laser theory.

Let's consider first the Lagrangian density for a complex scalar field ϕ:

$$\mathcal{L} = \partial^\mu \phi^* \partial_\mu \phi - \mu^2 \phi^* \phi - \lambda(\phi^* \phi)^2 \tag{1.26}$$

The first component of the Lagrangian density corresponds to the kinetic term of a complex scalar field, while the second component is related to a scalar potential. The coefficient μ^2 is a real parameter. Nevertheless, depending on its sign, the potential can take two forms.

If $\mu^2 > 0$, the symmetry is unbroken and the potential has a minimum at $\phi = 0$ which does not degenerate. It describes a particle with a mass μ and a quartic self-coupling. As the transformation $\phi \rightarrow -\phi$ is respected, this solution is a symmetric one.

When $\mu^2 < 0$, there is not a unique ground state for this system but multiple states with the same vacuum energy. The minima is located on a circle of radius:

$$v = \sqrt{\frac{-\mu^2}{2\lambda}} > 0 \tag{1.27}$$

By choosing a particular solution as the ground state, the symmetry gets spontaneously broken.

A parametrisation of the excitations around the ground state is possible by introducing a new field ϕ:

$$\phi(x) = \frac{1}{\sqrt{2}} \left(v + \rho(x) + i\Theta(x) \right) \tag{1.28}$$

The value v is given by one of the solution from equation 1.32, $\rho(x)$ and $\Theta(x)$ are real fields.

By adding the new field in the equation 1.26, the Lagrangian becomes:

$$\mathcal{L} = \frac{1}{2}(\partial_\mu \rho)^2 + \frac{1}{2}(\partial_\mu \Theta)^2 - \lambda v^2 \rho^2 - \lambda v(\rho^3 + \rho\Theta^2) - \frac{\lambda}{4}(\rho^2 + \Theta^2)^2 \tag{1.29}$$

The field $\rho(x)$ describes a state of mass $m_\rho = 2\mu^2$, coupled to the massless field $\Theta(x)$.

The field $\Theta(x)$ describes excitations around a direction in the potential. The excitations are not costing any energy, so they correspond to massless bosons called Goldstone bosons.

1.2.2 Higgs mechanism

As we have seen with the Lagrangian of the QED and QCD, the bosons generated are massless. Nevertheless, the $W^\pm$ and the Z bosons have a mass and the equation **??** of the EW interaction does not include a mass generator. The origin of the fermions masses is solved in the SM thanks to the Higgs-Englert-Brout mechanism [23][17].

Lets consider first a doublet of complex scalar fields Φ:

$$\Phi = \begin{pmatrix} \phi^+ \\ \phi^0 \end{pmatrix} \tag{1.30}$$

The invariant Lagrangian density under $SU(2)_L \otimes U(1)_Y$ gauge transformation is:

$$\mathcal{L} = \left(D^\mu \phi\right)^\dagger \left(D_\mu \phi\right) - V(\phi) \tag{1.31}$$

The covariant derivative is the one of $SU(2)_L \otimes U(1)_Y$ given by the equation 1.25 and represents the kinetic term. The Higgs potential is similar to the one considered first and has also two solutions depending on the sign of μ^2. Let's focus only on the negative solution. There is an infinite set of degenerated states with minimum energy:

$$\phi_0 = \sqrt{\frac{1}{2}}\begin{pmatrix}0\\ v\end{pmatrix} \text{ with } v = \sqrt{\frac{-\mu^2}{\lambda}} > 0 \tag{1.32}$$

Let's expand the field Φ around its minima by including a field $h(x)$ which describes quantum fluctuations and three massless Goldstone fields, denoted $\theta^i(x)$:

$$\Phi(x) = e^{i\frac{\sigma_i}{2}\theta^i(x)}\frac{1}{\sqrt{2}}\begin{pmatrix}0\\ v+h(x)\end{pmatrix} \tag{1.33}$$

A particular gauge can be defined in a way that the Goldstone fields are absorbed by the physical field of $SU(2)_L \otimes U(1)_Y$. It implies the apparition of mass terms in equation 1.31. First, we are interested in the mass generation mechanism. We consider only on the impact of the new field on the derivative covariant and omit any terms containing h and remove down the partial derivative:

$$\left|\left(i\frac{g}{2}\mathbf{W}_\mu + i\frac{g'}{2}Y\mathbf{B}_\mu\right)\Phi\right|^2 = \frac{1}{8}\left|\begin{pmatrix} gW_\mu^3 + g'B_\mu & g(W_\mu^1 - iW_\mu^2)\\ g(W_\mu^1 + iW_\mu^2) & -gW_\mu^3 + g'B_\mu\end{pmatrix}\begin{pmatrix}0\\ v\end{pmatrix}\right|^2 \tag{1.34}$$

The charged fields can be expressed as a linear combination of gauge fields:

$$W_\mu^\pm = \frac{W_\mu^1 \mp iW_\mu^2}{\sqrt{2}} \tag{1.35}$$

The eigenstates are rewritten as decorrelated terms representing the neutral fields from the EW symmetry group:

$$Z_\mu = \cos\theta_w W_\mu^3 - \sin\theta_w B_\mu \tag{1.36}$$

$$A_\mu = \sin\theta_w W_\mu^3 + \cos\theta_w B_\mu \tag{1.37}$$

θ_w is the Weinberg angle and represent a bound between the coupling g and g':

$$\sin\theta_w = \frac{g'}{\sqrt{g^2+g'^2}} \ and \ \cos\theta_w = \frac{g}{\sqrt{g^2+g'^2}} \tag{1.38}$$

The equation 1.34 becomes:

$$\begin{aligned}\left|\left(i\frac{g}{2}\mathbf{W}_\mu + i\frac{g'}{2}Y\mathbf{B}_\mu\right)\Phi\right|^2 &= \frac{1}{8}\left|\begin{pmatrix} A_\mu\sqrt{g^2+g'^2} & gW_\mu^- \\ gW_\mu^+ & -Z_\mu\sqrt{g^2+g'^2}\end{pmatrix}\right|^2 \\ &= \frac{1}{2}M_Z^2 ZZ^* + \frac{1}{2}M_W^2 W^-W^+\end{aligned} \tag{1.39}$$

With $M_Z = \frac{1}{2}v\sqrt{g^2+g'^2}$ and $M_W = \frac{1}{2}vg$, the mass of the Z boson and the $W^\pm$ bosons. The mass of the photon is consistent with the expectation and is null.

The Higgs mechanism implies the existence of a massive gauge field, the Higgs boson. It is coupled to the other bosons and also to itself. This could be shown by extending the Higgs potential with the field defined in equation 1.33:

$$-\lambda v^2h^2 - \lambda vh^3 - \frac{1}{4}\lambda h^4 \tag{1.40}$$

The first term gives the mass of the Higgs boson, $M_H^2 = 2\lambda v^2$, while the second and third terms are the Higgs self-interactions. The Higgs mass can not be predicted by the theory because it is given by a function of the parameter λ, which is one of the free parameters of the SM.

Yukawa couplings with fermions

1.3 Beyond the Standard Model

The SM constitutes one of the most successful achievements in modern physics. One of its strength is to provide an elegant theoretical framework to describe the known experimental facts about particles, but it is also able to predict the existence of a mechanism to generate the particle masses via the Higgs mechanism. Nevertheless, a lot of mysteries in the Universe are not explained by this theory.

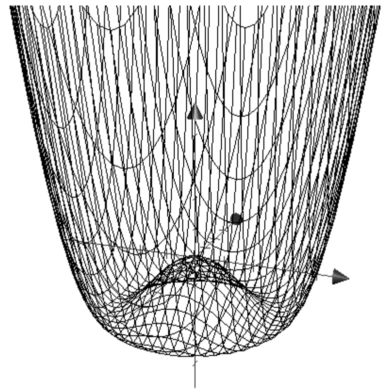

Figure 1.2 – Scalar potential: ADD A GOOD CAPTION.

1.3.1 Limitations of the Standard Model

Despite the fact that the experimental results are in good agreement with the SM predictions, this theory does not provide answers to may questions. The particle physics community tries to unify theories.

Free parameters

Up to 19 free parameters are used in the SM and this theory does not explain their existence. Even if it is not as major problem for the physics itself, the particle physics community has a lack of understanding and explaining these values. The free parameters are:

- the masses of the nine fermions
- the coupling constants g and g' of the $U(1)$ and $SU(2)$ groups
- the coupling constant of the strong interaction α_s
- the angles of the CKM matrix
- the Higgs boson mass and the *vev* parameters that allows CP violation in QCD Lagrangian.

Hierarchy problem

The hierarchy problem refers to two main energy scales problem of the SM.

First of all, the difference between the energy scale of the SM and the Planck scale is of seventeen orders of magnitude. No "intermediate" physics has been found between the two scales.

A second problem occurs while considering the Higgs boson mass. The SM does not predict its mass, but it sets some theoretical bounds with respect to Λ, the energy scale at which the SM is not valid anymore. The theoretical Higgs boson mass is higher than what it should be compared to the EW scale. The Higgs boson interacts with the particles of the SM (fermions, W and Z boson), but it also interacts with itself. Due to the scalar nature of the boson, there are quartic divergences while calculating the loop corrections. The quantum corrections, which take into account the coupling of the Higgs boson, are Λ^2 divergent and lead to a huge Higgs boson mass. To avoid that, delicate cancellations should occur between the quantum corrections. These cancellations are known as the fine-tuning problem.

Gravitation

Although particle physicists are dreaming of a "theory of everything" that will unify the electroweak, strong and gravitational interactions, there is no viable theory to describe the gravity in a quantum point of view to include it in the SM and which would be still valid at a macroscopic scale.

Neutrino mass

The neutrinos defined by the SM are assumed to be exactly massless. Nevertheless at the end of the year 1990, the Super Kamiokande experiment had surprising results[21]. The measured flux of of solar and atmosphere neutrons was lower than expected. The result was interpreted by an oscillation of neutrinos between the three leptonic flavors. However, the oscillation is possible only if the neutrino has a mass. That phenomenon could be considered as a proof of physics beyond the SM.

Matter-antimatter asymmetry

As discussed at the beginning of this chapter, the SM defines an equal number of particles and anti-particles. In the case of the Big Bang theory, it is assumed that the matter and antimatter were created in an exactly equal amount, a mechanism has favoured electrons, protons, and neutrons with respect to positrons antiprotons and antineutrons. If the amount of matter and antimatter was equal, our Universe would have been completely annihilated. The matter domination could be a local phenomenon with an antimatter surrounding the region. However, the region of contact between matter and antimatter would be a violent place of interaction, which would disturb the cosmic microwave background.

An assumption to explain the asymmetry is that the antimatter was produced in an infinity proportion compared to the matter. Hence, the annihilation as lead to create a Universe only made of matter. A mechanism which tends to prefer the matter has been observed in the study of the kaon oscillation. This particle is able to transform spontaneously to its own anti-particle and vice-versa. Nevertheless, this transformation is not symmetric: the kaon is slower to turn into an anti-kaon than the inverse transformation.

Dark Matter and dark energy

Several astrophysical observations are indicating that the Universe is made not only of visible matter but also of matter that seems to be invisible to the electromagnetic interaction and is called the dark matter. In 1933, a measurement of the galaxies velocities in the Coma cluster to determine the cluster mass gives a surprising result. The mass was more than two orders of magnitude bigger than the mass of visible stars in the cluster. It was found that the matter of the SM describes only 5% of the Universe content. The rest of the Universe is made of 22% of dark matter and around 73% of dark energy. The neutrinos are possible candidates to dark matter, as they couple to SM matter only via weak interaction, but they cannot account for the entire density of the universe. Nowadays only twelve particles (plus the anti-particles associated) have been observed.

1.3.2 Theories beyond the Standard Model

Supersymmetry

The Supersymmetry (SUSY) is a QFT, that relates the elementary fermions known to corresponding bosons, called sfermions and the bosons to corresponding fermions, called sbosons [40]. The new particles introduced are called super-partners. They have the same mass, the same quantum numbers but the spin is differing by a half factor. SUSY is a broken symmetry. This will allow the super-particles to acquire very high masses.

SUSY is a good candidate for physics beyond the SM, as it could solve the hierarchy problem without any fine tuning. For example, the loop contributions of one particle to the Higgs are cancelled by the loop contributions of its super-partner. It would be able to provide a framework for the unification of the three gauge interactions at a GUT scale. The lightest super-particle is a good candidate for the Dark Matter.

Despite it will answer many questions from the SM, there is a lack of understanding why SUSY is a broken symmetry.

Grand unification theory

After the success of the electroweak unification, the next step is to include the strong interaction to build the Grand Unification Theory (GUT), an extension of the SM. In this framework, the three forces are different manifestations of a single interaction. It includes the $SU(3)_C \otimes SU(2)_L \otimes U(1)_Y$ symmetry group into a larger $SU(5)$ group. The quarks and leptons are ordered in left decuplets and right quintets. The coupling constants are described by only one parameter. There are 24 mediators, the 12 mediators of the SM plus 6 X mediators (charge $\pm 4/3$ and 3 colors) and 6 Y mediators (charge $\pm 1/3$ and 3 colors). It predicts the existence of new particles as leptoquarks[3], multiple Higgs bosons and new currents.

Unfortunately, the theory is not validated because of its prediction of the proton lifetime. The first GUT was introduced by Georgi and Glashow in 1974 and predicted the decay of the proton. The actual experimental limit of the proton lifetime is of 5×10^{32} years, whereas the predicted lifetime defined by the SU(5) group is one order of magnitude lower. [36]

Technicolor

The technicolor is a theory that explains the mass generation. Contrary to the EW symmetry, the masses of particles are not generated by the spontaneous symmetry breaking but they are generated by a strong gauge interaction. This interaction is strong and confined at the energy that has been experimentally probed. The approach of the theory avoids the hierarchy problem induced by the SM.

[3] Coupling between a lepton and a quark

String theory

The particle physicists have the dream of unifying the forces of the nature to have only one single interaction with four different manifestations. The string theory proposes a framework for the "theory of everything". The basic unit of matter is no more considered as particles but one-dimensional strings of which particles are various vibrational modes.

The string theory is a theory of quantum gravity. It tries to unify the gravitation to the quantum Extra dimensions of 10 -11 space-time dimensions. Possible explanation for the hierarchy problem.

1.4 Conclusions

Along this chapter, the successes and limits of the SM were discussed. The high energy physics community is trying to study as far as possible the limit of the SM and is also trying to find some proof of new physics beyond the SM. The Large Hadron Collider (LHC) at CERN has permitted in 2012 to point out the existence of a Higgs boson. Nevertheless, the beam structure of the LHC is not efficient enough to perform very precise measurements. Because of the collision between protons, the energy of the collision can't be exactly known. The next chapter deals with a future experiment in high energy physics, where electrons and positrons are used to probe the matter instead of protons and anti-protons.

Chapter 2

The future of high-energy physics: the International Linear Collider

Since 2008, the LHC is actually the most powerful tool in high-energy physics to have a better understanding of the universe, particularly with the discovery in 2012 of a new particle compatible to the boson predicted by the spontaneous symmetry breaking of the SM [3, 12]. Although the LHC is an impressive machine able to reach the highest energy scale of collision available on Earth with a centre-of-mass energy of 13 TeV, the complex environment of the events generated hides the access to some fundamental parameters. To achieve more precise measurements of the Higgs boson, but also to test the validity of the SM and other physics theories introduced in the chapter 1, the high energy physics community has merged on the necessity to build a linear electron-positron collider, that will work as a complementary accelerator to the LHC.

This chapter will explain the motivations to invest a huge amount of money in a new great world project. It will present the complementary nature of the lepton and hadron colliders and the main advantages of the lepton collisions will be discussed. After giving an overview of the ILC with its basic design and the experiment models, we will focus on the design of one of the detectors: the International Large Detector (ILD).

Contents

2.1 To a linear lepton collider

The most impressive accelerator ever built is located at CERN in Geneva, Switzerland. It is the world largest particle accelerator, with a circumference ring of nearly 27 kilometers, straddling the Swiss and French borders. It is designed to collide two counter rotating beams of protons or heavy ions, with a possibility to reach centre-of-mass energies of 13 TeV with a high peak luminosity of 10^{34} cm^{2}s^{-1}. The goals of the LHC are to perform further tests on the SM, search for new forces or produce dark matter candidates. Indeed, the collider covers a wide energy range at the constituent level while running at a fixed beam energy. Unfortunately, due to the nature of the particles used, the experiment can not reach the highest precision measurements needed.

Complementary to a discovery machine such as the LHC, a machine to perform precise measurement should be built: the linear lepton collider.

2.1.1 Advantages of a linear lepton collider

First of all, during each collision at an hadron collider, only a part of the total centre-of-mass energy is available for the process evolved, therefore the initial four-vector momentum is not known. By colliding leptons, which are structureless objects, the full centre-of-mass energy is available for the elementary process. The initial four-vector momentum of an interaction is exactly known, hence the event can be fully reconstructed.

Secondly, with a lepton collider, the beam energy is tunable and both electron and positron beams can be polarised. The selection of an appropriate polarisation can boost the signal and suppress the background cross-section.

Thirdly, as seen in the first point, at the LHC, only a fraction of the partons are contributing to the interesting process. The proton-proton interaction cross section is dominated by inelastic background QCD processes. The signal event is then accompanied by large backgrounds produced by the interaction of other parton collisions. This background masks the elementary process of interests, in order that it has an impact on the detector design, that should have a high radiation tolerance and implement a selective trigger to reduce the data rate. The lepton colliders do not suffer from this kind of background and at similar energies, the event rate is lower as those of hadron colliders. Moreover, the interaction of electrons and positrons is purely electroweak. In consequence, the detector does not have to handle extreme data rates and can be used without any trigger. Hence, the sensitivity to any possible signature of new physics is improved.

Although the leptons, in particularly the electron and positron, have clearer advantages on hadrons to perform a precise measurement, the choice of a linear collider comes from the physics of accelerating charged particles. While charged particles are moving in a circular accelerator, they lose some energy by emitting photons via synchrotron radiation. The equation 2.1 describe the energy loss via synchrotron radiation:

$$\Delta E_{sync} \sim \frac{E^4}{m^4 r} \tag{2.1}$$

The radiative energy loss is proportional to the radius r of the accelerator, the energy of the particle E to the power of the fourth and its mass m to the power of the fourth. As the electron mass is $\sim 1.8 \times 10^3$ smaller than the proton mass, the energy loss radiated by the electron is bigger than the energy loss radiated by proton at the same centre-of-mass energy. To compensate the energy loss, a circular electron-positron accelerator should have an extremely big radius (bigger than the actual LHC), increasing the cost to build the experiment. Another solution to overcome the synchrotron radiation is to accelerate the particles in a linear collider. Nevertheless, the centre-of-mass energy has to be reached in only one path, whereas the bunch of particles in a circular collider is accelerated many times in the ring until the desired energy of collision is reached. To still get an "affordable" experiment, the centre-of-mass energy obtained at a linear collider is below to the one from a circular collider. Indeed, to work at the same energy scale, a linear collider would require a bigger number of accelerating cavities and would make a much bigger and more expensive collider than a circular one.

2.1.2 Future linear lepton collider

As it was mentioned before, the precise measurements offered by lepton collider is one of the key points to constrain the limits of the SM and to characterise precisely all the known particles. Since the 1980's, several linear collider technologies have been developed, leading in the 1990's to five major accelerator technologies: Superconducting Radio-Frequency (SRF), the Compact LInear Collider (CLIC) technology and three different normal conducting technologies (S-band, C-band, and X-band)[15]. At the beginning of the 2000's, a committee for the future linear collider was formed and has chosen in 2004 the SRF technology[24] and since then all the efforts are done in that direction to build the International Linear Collider (ILC). The technology developed for this future experiment is also used for the XFEL at DESY in Hamburg and at KEK in Japan. Another linear collider project led by the CERN is being prepared: the CLIC. It has a more challenging technology to aim a nominal energy of 3 TeV instead of 1 TeV for the ILC. Contrary to the ILC, CLIC plans to use radio-frequency structures and a two beam concept. Another idea would be to develop a muon collider instead of electron-positron collider[32]. As the electron, the muon is a pointlike particle, therefore the centre-of-mass energy can be easily adjusted to perform a precise study. The muon mass is 207 times much bigger than the electron ones and suffers less of energy loss by synchrotron radiation. Hence, a circular collider could be more adapted and the beamstrahlung effects would be smaller in a muon collider than in an e^+e^- machine. Nevertheless, the muon has a lifetime of only 2.2 μs making up a more challenging acceleration design.

Paper on ILC

Paper on CLIC

For the purpose of this thesis, the CLIC and muon colliders will not be described more to focus on details on the ILC.

2.2 The ILC machine

The ILC should be the next lepton collider experiment and will be situated in Japan. During 2016, the physicists community is waiting for an official decision of the Japan government concerning final site where the experiment will be held. At the time this thesis was written, the most likely site candidate is located in the north of Japan, in the region of Kitakami.

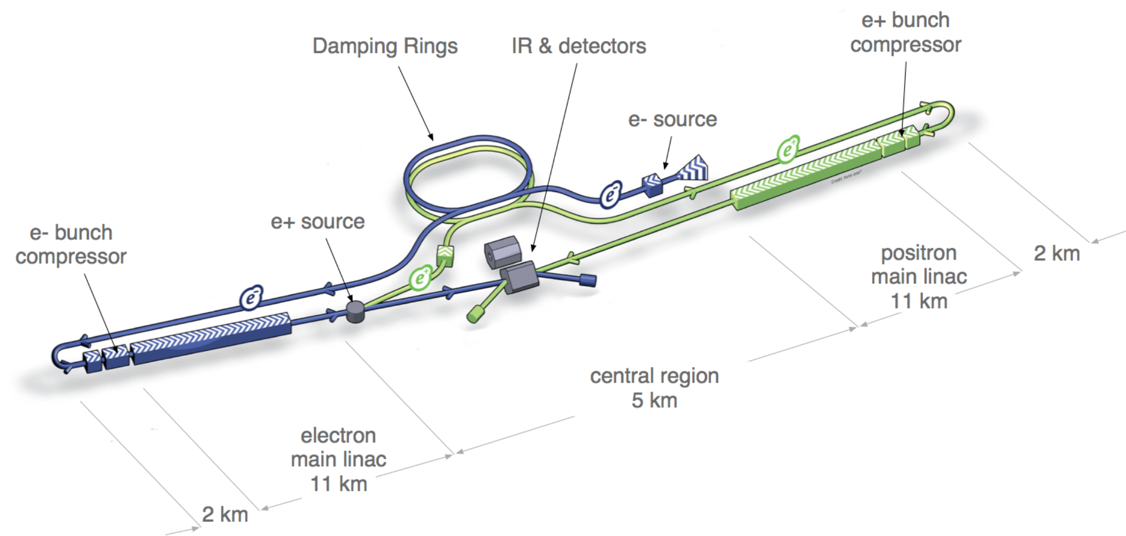

Figure 2.1 – Schematic layout of the International Linear Collider (ILC).[9]

2.2.1 Baseline design

The ILC is planned to collide electrons and positrons at a center-of-mass energy up to 500 GeV, with an energy variability down to 200 GeV for 31 kilometers long accelerator. An upgrade to reach the centre-of-mass energy of 1 TeV is also possible, but the accelerator should be extended to achieve a total length of 50 kilometers. It is designed to generate a total of 500 fb^{-1} of data during the first four years of operation. The luminosity will reach a peak of $2 \times 10^{34}\text{cm}^{-2}\text{s}^{-1}$ at $\sqrt{s} = 500$ GeV.

The main components of the ILC are presented in the following order: first of all, an overview of the electron source and their acceleration via the conducting and superconducting structures, then the role of the damping rings, the injection into the main linacs, followed by the positron source and the Beam Delivery System (BDS) to finally present the interaction region (IR). A detailed description of the ILC could be found in the Technical Design Report[4].

2.2.2 Machine design and beam parameters

The polarised electrons are produced by a laser firing a strained GaAs photocathode in a Direct-current (DC) gun. To implement a redundancy, the electron generation system is made of two lasers and DC guns, providing bunches with a polarisation of 90 %. The electrons are then pre-accelerate to 76 MeV thanks to non-superconducting accelerating structures. Thereafter, they are injected into a 250 m long superconducting linac to reach the energy of 5 GeV. Nevertheless, the dimension and density of bunches are quite extended, thus their emittance is too wide. Before to inject the bunches into a damping ring, which is used in order to decrease the emittance and reach the desired luminosity, superconducting solenoids rotate the spin vector into the vertical direction, while SRF cryomodules are used for an energy compression.

The damping ring is 6.7 km length and made of magnets and wrigglers that are going to force the particles to get a bent track. This system is used to dump the electrons with large transverse and longitudinal emittance to the low emittance required for the luminosity production. The reduction of the emittance should be achieved within 200 ms between the machine pulses. Although the positron source was not yet introduced, their bunches suffer from the same problems as the electron ones. A second damping ring, placed in the same cavern as the electron one, is also in charge to get the desired emittance.

The bunches are then extracted from the damping rings and transferred via the Ring To the Main Linac (RTML) structure, the longest continuous beam line at the ILC. It is divided into five subsystems to transport the bunches from the damping rings to the BDS, in order to orient the beam in the desired polarisation by rotating the spin of the particle, but also to compress the beam bunch length from several millimeters to a few hundred microns thanks to a two-stage bunch compressor. At the same time the bunches are compressed, sections of SRF technology accelerate the bunches from 5 GeV up to 15 GeV. One of the challenges of the RTML is to preserve the emittance obtained after the damping rings, while the length and the energy of the bunches are tunned. Then, the particles are delivered to the main Linac, an 11 km long accelerator using 1.3 GHz SRF cavities, made of niobium.

Before to reach the interaction region, the primary electron beam is transported through a 147 m superconducting helical undulator to produce photons from $\sim$ 10 up to $\sim$ 30 MeV, depending on the energy of the primary beam. This primary beam is separated from the photons and sent back to the BDS with an energy loss of $\sim$ 3 GeV. The photons are directed onto a rotating Ti-alloy target to create e^+e^- pairs that are separated. The positrons collected are accelerated to 125 MeV thanks to a normal conducting linac and then accelerated to 5 GeV with a superconducting boost linac. Finally, they are introduced into the damping ring to reduce their emittance.

The two beams are transported from the high energy LINACS to the IR by the BDS, in charge to focus the beams to the sizes required to meet the ILC luminosity wanted. It is divided into five main subsystems. First, in the direction of the beam, a system is in charge to perform some emittance measurement and matching, to give a trajectory feedback, and provide a polarimetry and energy diagnostic. Then the beam is collimated to remove the beam-halo particles that would generate a huge amount of background in the detector. Muons generated during the collimation process are deflected by magnetised iron shielding. Thereafter, strong compact quadrupoles focus the beam to the sizes required to meet the desired luminosity. Before the collisions, crab cavities rotate the bunches in the horizontal plane for effective collisions and to achieve a 14 mrad total crossing angle. After the collisions, an extraction line is dedicated to transport the beams into the main beam dump.

Although two experiments will run at the ILC, there will be only one interaction region due to cost reasons. Indeed, to have two experiments running at the same time, it requires two separate BDS of 4 km long each. Thanks to a push-pull scheme, the detectors will work alternatively: while one is taking data, the other one is sitting in the garage to be maintained. The two detectors will be presented in more details at section 2.3.

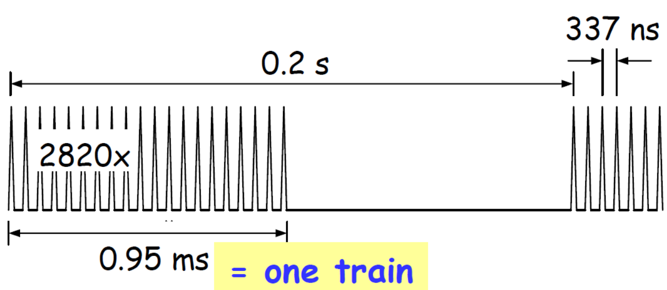

Figure 2.2 – Representation of the bunch structure at the ILC. One bunch train is made of 2625 bunch crossings and lasts 0.95 ms. Each bunch crossing is spaced out by 337 ns. Two bunch trains are of 0.2s apart from each other.[31]

The accelerator described above will create bunch trains at a repetition rate of 5 Hz. Each train is composed of 2625 bunches that contain 2×10^{10} particles and lasts 0.95 ms. The interval between two trains is 2 ms long. This structure is a feature key to develop detectors able to be switched off during the dead time in order to reduce the power consumption.

2.2.3 Beam backgrounds

To design the detectors of the ILC, the backgrounds must be understood and taken into account to give optimal performances. Tthe event reconstruction becomes more complicated with hits caused by background particles. They are two kinds of background, the one created by the BDS and the one related to the interaction point. As it was discussed in the subsection 2.2.2, the collimator placed closed to the interaction point (IP) to purify the beam can produce muons by an electromagnetic shower. To sweep them away, iron spoilers are used to create a magnetic field and deflect the muons. A side effect is to increase the number of neutrons created in photo-nuclear reactions. A concrete wall placed at the entrance of the experimental hall vanishes the neutron background.

Contrary to the LHC, the ILC will not suffer from the QCD background, as mentioned in subsection 2.1.1 Nevertheless, due to the nature of electrons and positrons, the two beams will interact each other before they collide. The electromagnetic beam field of each bunch is high and causes the focusing of the opposite bunch. It is bending the electron/positron trajectories near the IP. On the one hand, this effect helps to focus the incoming beams and enhance the luminosity. On the other hand, as the charged particles have bending track, they are emitting hard photons via beamstrahlung, creating e^+e^- pairs background. The hard photon is strongly focused in the forward region and do not contribute strongly to the background in the detector. However, the e^+e^- pairs created contribute to the background directly or through backscattered particles. In consequence of the beamstrahlung, the beam particle energy is reduced, hence the collisions occur at different energies from the nominal one and this affects the physics cross-section. The beamstrahlung photons can also produce neutrons by hitting components. The other source of hard photons is the initial state radiation. With the beamstrahlung, they contribute reducing the luminosity[34].

Different kinds of soft pairs background can be expected at the ILC: the coherent and incoherent pair production. The coherent pair production appears when beamstrahlung photons are interacting with the strong electromagnetic field of the beams. In the ILC environment the coherent pair background are negligible, whereas the incoherent pair production is dominant. It corresponds to e^+e^- pairs created by the interaction of only two particles. They are to the number of three depending on the nature of the scattered photons creating the e^+e^- pair. The Bethe-Heitler process corresponds to the scattering of one real photon while the second one is virtual. It contributes to approximately two of the third pair production. The second process is the Landau-Lifshitz, where the two scattered photons are virtuals and contribute to approximately to the third of the pair creation. The last production occurred via two real photons (Breit-Wheeler process) and contribute only to a percent level. The incoherent e^+e^- pairs are produced at a relatively low transverse momentum and are emitted in the forward direction.

2.3 The ILC detectors concept

2.3.1 Overview of the two experiments

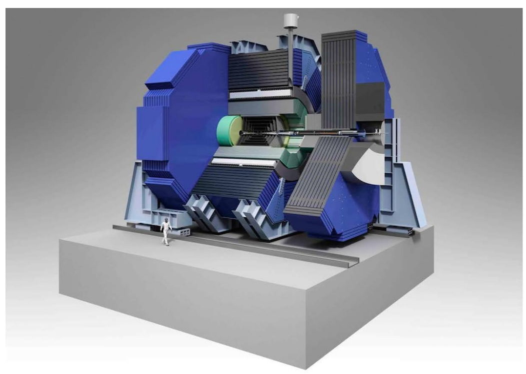

(a) The Silicon Detector

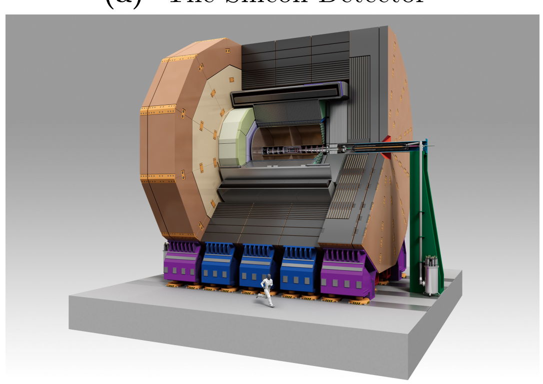

(b) The International Large Detector

Figure 2.3 – Overview of the two detectors designs at the ILC. The figure a represents the SiD design while the figure b shows the ILD approach.[10]

As it was presented in the subsection 2.2.2, the ILC will be built with only one interaction region due to cost reasons, whereas two detectors are expected. The push-pull operation scheme will allow for data taking of one detector, while the second one is out of the beam in a close-by cavern for maintenance. The interval to switch the detectors should be short enough and of the order of one day. This time efficient implementation sets specific requirements for the beam structure but also for the detector design. The detectors should be placed on platforms to preserve the alignment and to distribute the load equally onto the floor. Another requirement on the detector design is that the magnetic fields outside the iron return yokes must be small enough to not disturb the second detector on the parking position. It is assumed that a limit of 5 mT at a lateral distance from the beam line should be sufficient.

The motivation to build two detectors with a different approach is mainly to provide a cross-checking and a confirmation of results and complementary strengths. Both detectors are optimised to study a broad range of precision measurements and search of new physics drove by the ILC expectations. Their performances are driven by the Particle Flow Algorithm (PFA) to be able to measure the final states of events with a high accuracy. To do so, both detectors should have a high hermeticity, high granularity calorimeters and excellent tracking and vertexing. The PFA is shortly presented on subsection 2.3.2.

The Silicon Detector (SiD) is a compact detector made of a silicon tracking and 5 T magnetic field. The tracking system should provide robust performance thanks to the time-stamping on single bunch crossings. The calorimeters should be highly granular to perform the PFA.

The second detector is the ILD. In contrast to the SiD, the tracking system is based on a continuous readout Time-Projection-Chamber (TPC) surrounded by silicon tracking detectors. The magnetic field will be only of 3.5 T combined with granular calorimeters for a good particle-flow reconstruction

2.3.2 Particle flow algorithm

The main purpose of the ILC (or the CLIC) is to achieve precise measurements of physics processes that produce final states with multiple jets. The jet energy resolution at the ILC should be sufficient to cleanly separate W and Z hadronic decays. Typically, the jet energy resolution is deduced from the equation 2.2, where α is the stochastic term usually greater than $\sim 60\%/\sqrt{E(GeV)}$.

$$\frac{\sigma_E}{E} \simeq \frac{\alpha}{\sqrt{E(GeV)}} \oplus \beta \tag{2.2}$$

The PFA approach is the extended version of the Energy Flow approach (used at H1, D0, CMS) for a highly granular detector. The goal of this framework is to achieve a stochastic term for the energy resolution greater than $30\%/\sqrt{E(GeV)}$, not reachable with a traditional calorimeter. Each sub-detector should be efficient enough to separate and to reconstruct the four-vectors of all visible particles in an event. The energy of charged particle is measured in the tracking detectors, while the energy measurements for photons are done in the electromagnetic calorimeter and neutral hadrons are done in the hadron calorimeter.

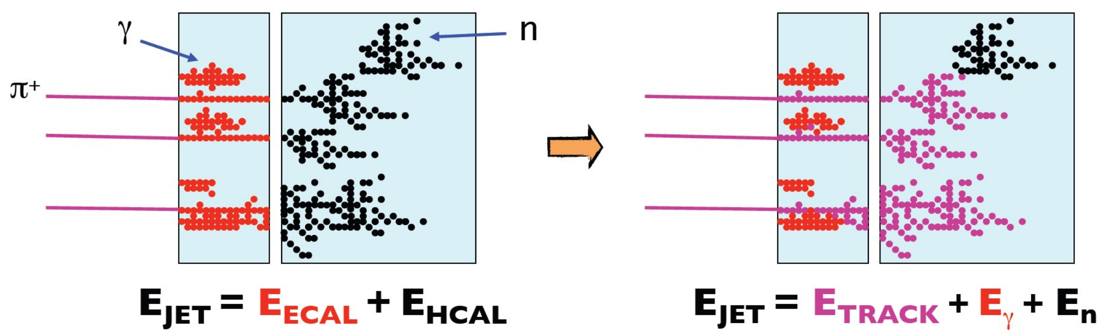

Figure 2.4 – Two different approaches for calorimetry. On the left is the traditional calorimetry method used on most of the experiments, the right one is the particle flow approach for calorimetry. The particle track is taken into account to calculate the jet energy.[22]

The PFA requirements drive the design of the detectors at the ILC. For both experiments, the electromagnetic and hadronic calorimeter have to be located inside the solenoid. Moreover, each sub-detector must be able to distinguish single particle signals, imposing a better tracking precision and higher granular calorimeters than the traditional detectors in high energy physics.

2.3.3 The ILD detector

The design of ILD follows the requirements for optimal PFA performance. In summary, the detector should be highly granular to have a robust three-dimensional imaging capability. It will combine a high-precision Vertex De-

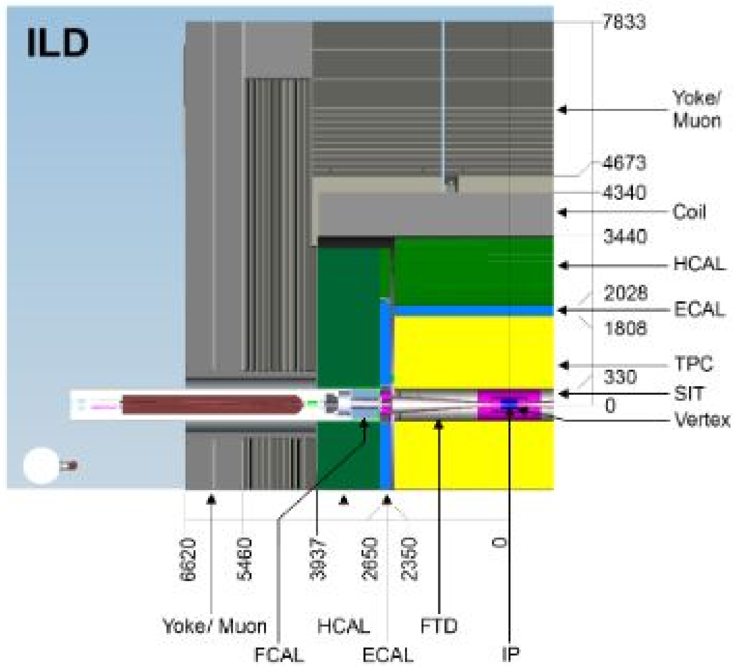

Figure 2.5 – Quadrant view of the ILD detector concept with its subdetector system [10]

tector (VXD) system, a hybrid tracking system and calorimeters inside a 3.5 T solenoid. On the outside, a coil and iron return yoke will be instrumented as a muon system and a tail catcher.

Vertex detector

The VXD is the closest detector to the interaction region and it is in charge to the measured to track particles and to measure the decay vertices of the particles. For the moment, two vertex detector design are under study, but both of them have a pure geometry barrel. One geometry is made of five single sided layers, whereas the other one has three double-sided detection layers. The chapter **??** will introduce in more details the vertex detector requirements for the ILD, such as the material budget and the measurements precision aimed. The different design proposals will be presented.

Tracking

The main tracking system for the ILD is performed by the TPC. It is a gaseous detector with a low material budget designed to measure the particles' trajectory. When a particle traverses through the TPC, it ionises the gas, creating electrons that are drifting to the anode thanks to a high voltage. The anode is the part where the readout plates are installed. It provides a 3D position of the particles tracks thanks to the wires and the anode (give x-y) and the z coordinate is given by the drifting time. In addition to the exact position measurement, this detector is also able to measure the energy $\frac{dE}{dx}$ deposited by the particle and would be the first step for a particle identification.

The requirements to design a TPC at the ILC are given by two main values:

- The single point resolution $\sigma_{s.p.}$ which should be lower than 100 μm in the $r\phi$ direction and less than 500 μm in the z direction;
- The minimum distance to separate two hits which should be lower than 2 mm.

The TPC thought for the ILD is constituted of a central barrel part, with an inner radius of $\simeq$ 33 cm and a outer radius of $\simeq$ 180 cm and two endcaps with a detection area of 10 m^2. The solid angle coverage is up to $|\cos\theta \simeq 0.98|$. The barrel will be filled with a gas mixture called T2K (3 % of Ar-CF4 and 2 % of isobutane). Due to the low material budget and the ability to cope with a high magnetic field, the TPC is compliant with the PFA 2.3.2.

To improve the track reconstruction, the TPC is surrounded by high silicon detectors: two barrel components, the Silicon Internal Tracker (SIT) and the Silicon External Tracking (SET); an end-cap component, the Endcap Tracking Detector (ETD) and the Forward Tracking Detector (FTD). The SIT is linking the tracking between the VXD and the TPC, whereas the SET is giving an entry point to the Electromagnetic CALorimeter (ECAL) after the TPC. Both systems provide precise space points and improve the overall momentum resolution. The goal of the SIT is to improve the momentum resolution, the reconstruction of low p_T charged particles and the reconstruction of long-lived particles. The coupling of the SIT and SET provide also a time-stamping information.

The ETD is located within the gap separating the TPC and the endcap calorimeter. It improves the momentum resolution for charged tracks with a reduced path in the TPC. It also reduces the effect of the material of the TPC end-plate. The material budget of this end-plate is estimated to 15 % of X_0.

As the TPC does not provide any coverage in the forward region, seven silicon disks ensure efficient and precise tracking down to very small angles, whereas the ETD and the FTD make sure to get a full tracking hermeticity.

To simplify the system layout and the maintenance, the SIT, SET and ETD are made of single-sided strip layers tilted by a small angle with respect to each other. They are placed in a so-called false double-sided layers. The SIT has two layers of microstrip, instead of one layer for the SET. The technology studied are microstrip sensors with an area of 10x10 cm^2, with a pitch of 50 μm, a thickness of 200 μm and an edgeless. The dead area of the sensors will be reduced down to few microns instead of 100 μm. The spatial point resolution aimed for this detectors is $\sim$ 7.0 μm in the $r\phi$ direction. The table 2.1 gives the single point resolution aimed, as well as the angular coverage and the material budget.

Detector	Single point resolution (μm)	Coverage	material budget X_0 (%)
SIT	$\sigma_{R-\phi} = 7.0$ $\sigma_Z = 50.0$	$\cos\theta \sim 0.91$	0.65
SET	$\sigma_R = 7.0$	$\cos\theta \sim 0.79$	0.65
ETD	$\sigma_X = 7.0$	$\cos\theta \sim 0.799 - 0.985$	0.65

Table 2.1 – Parameters aimed for the silicon tracker using micro-strips sensors.

The FTD is placed in the forward direction, between the beam pipe and the inner field cage of the TPC, where the magnetic field becomes less and less useful to bend charged tracks and so the determination of a precise momentum is more difficult. It consists of seven tracking disks: the two firsts are pixel detectors to cope with expected high occupancies and the five others are strip detectors. The pointing resolution will vary between $3.0 - 6.0$ μm for the two firsts layers and 7.0 μm for the five other ones.

Check the table and values....

Calorimeters

The calorimeters design is driven by the particle flow requirements. Each particle must be reconstructed individually in the detector with a jet energy measurement equal to:

$$\frac{\Delta E}{E} = 30\%/\sqrt{\frac{E}{GeV}} \tag{2.3}$$

The energy resolution obtained in equation 2.3 is obtained thanks to a combination of information from the tracking system and the calorimeters. The choice of technology used for the calorimeter will be determined by the pattern recognition performance. One of the ILD detector's goal is, for example, to be able to get a jet energy resolution sufficient to clean separate W and Z hadronic decays.

The average jet energy distribution is roughly:

- 62% of charged particles (mainly hadrons)
- 27% of γ
- 10% of long-lived neutral hadrons
- 1.5% of ν

The ECAL is the first calorimeter right after the tracking system. Its role is to identify photons and leptons and measure their energy, nevertheless, it is also the first section to develop the hadron showers. The fine segmentation makes an important contribution to hadron-hadron jet separation. For the ILD, a compromise between the performance and the cost has led to use a sampling calorimeter realised with tungsten absorber. They are three options under study for the active area. The first one called SiW-ECAL, is made of silicon pin diodes with a pitch of $5 \times 5\text{mm}^2$. It has the advantage to cover a large area, to be reliable and simple to operate, to have thin readout layers and can be operated in 3.5 T magnetic field. The second option is made of scintillator strips readout by photo-sensors and is called ScECAL. It has an active area of $5 \times 45\text{mm}^2$ arranged in alternative directions to achieve an effective granularity of $5 \times 5\text{mm}^2$ The weakness of this technology happened in dense jets environment, where the reconstruction becomes more and more complicated. Some alternatives are also thought, like the Micromegas chambers. Nevertheless, this technology is less advanced compared to the others. One other good candidate could be the use of Monolithic Active Pixel Sensor (MAPS) sensors. They have the advantage to get the signal sensing and processing on the same substrate and by choosing standard CMOS processes, the cost of fabrication would be reduced.

The HAdronic CALanalogue HCALorimeter (HCAL) has the role to separate the deposits energy of charged and neutral hadrons and to precisely measure the energy deposited. It is also a sampling calorimeter using stainless steel instead of tungsten as an absorber. The rigidity of stainless steel makes possible to get a self-supporting structure limiting the dead areas. Two baseline technologies for the active medium area are studied. The Analogue HCAL (AHCAL) is made of scintillator tiles, whereas the semi-digital, called Glass Resistive Plate Chamber (GRPC), is based on the Semi-Digital HCAL (SDHCAL).

In order to monitor the luminosity and the beamstrahlung, the calorimeter system is completed in the very forward region by three different subsystems covering very small angles also for neutral hadrons: the LumiCal, the BeamCAL, and the Low angle Hadron CALorimeter (LHCAL). The LumiCAL is placed in a circular hole of the end-cap ECAL and covers polar angles between 31 and 77 mrad. It serves as luminosity monitor by measuring the Bhabha scattering $e^+e^- \rightarrow e^+e^-$ via emission of virtual γ. Indeed, the luminosity $\mathcal{L}$ is determined by measuring the ratio of the number of counted events N_B in a considered polar angle ranged and the integral of the differential cross-section σ_B in the same region. The measurement precision should be better than 10^{-3} at 500 GeV. After each bunch crossing, the beamstrahlung pairs hit the BeamCal. This would permit to get an estimation of the bunch-by-bunch luminosity, but also to determine the beam parameters. It is placed in front of the final focus quadrupole and covers polar angles between 5 and 40 mrad. The third system, the LHCAL, ensure the coverage of the hadron calorimeter to small polar angles.

Magnetic Field and yoke

By applying a high magnetic field inside the detector, the charged particles have a bent track helping in the identification and the energy measurement. At the ILD, the nominal magnetic field is 3.5 T and should have a high homogeneity inside the TPC. Moreover, as mentioned in subsection 2.2.2, the magnetic beyond the coil has to be reduced to avoid any perturbations with the second detector in its parking position. A superconducting coil surrounding the tracking and calorimetric system generate the magnetic field. It has a diameter of 6.88 m, a length of 7.35 m and made of three modules.

Surrounding the coil, an iron yoke ensures to return the magnetic flux. It is constituted by a barrel of 2.88 m thickness and 2 end-caps of 2.12 m thickness. Muon detectors are inserted inside the iron yoke in a sandwich-like structure. They're performing measurement on muons but they are also used as tail catchers, to improve the energy resolution of high energetic jets escaping the calorimeters.

2.4 Conclusions

In this chapter, the reasons to build a linear electron/positron collider were discussed by introducing the pros and cons of such a big experiment. In order to reduce the costs, only one interaction region is planned but two detectors are going to operate alternately. The design of the detectors is driven by the particle flow approach to reach a ... energy resolution. In particularly, the onion structure of ILD was peeled. The different sub-detectors and the technology options were introduced, except for the vertex detector. Indeed, the chapter 4 will be dedicated to the vertex detector at the ILD.

The next chapter will introduce the physics cases at the ILC, especially by describing an approach to a physics analysis to study the $H \rightarrow c\bar{c}$.

Chapter 3

Physics at the ILC

In the chapter 1, the framework of particles physics was described. Since the beginning of High Energy Physics, different experiments have been done to confirm the exactness of the SM but also to find new physics beyond the SM. The beam structure of the different colliders allow to perform different measurements with different precision. For example, the LHC has a high luminosity and high energy beam, able to reach new energy scales on earth, whereas the ILC is trying to reach more precise results, with less energy. Along this chapter, the physics scenarios that are going to be studied at the ILC are discussed. Afterward, the emphasis will be on the Higgs physics and the measurement that would be performed at the ILC. The last section aims to introduce a physics analysis scenario to study the processes which have a Higgs boson and two neutrinos in the final state.

Contents

3.1 Potential studies

As seen in chapter 2, the ILC will have a vast and variable tunable centre-of-mass energy. Due to the features of an e^+e^- collider, the initial state of collision is well defined. Contrary to the LHC, there are no strong interaction backgrounds and the electroweak background is controlled and calculable. This conditions will help to perform precise measurements and looking for new physics. The different measurements which will be performed are presented below.

First of all, a study of the Z boson at the centre-of-mass energy of $\sqrt{s} = 91$ GeV around the Z resonance is scheduled. This program called *GigaZ* will be able to collect more Z boson events than the Large Electron Positron collider (LEP) did, because of a luminosity two to three times higher than what was achieved. The data collected will allow a study on the asymmetries of the Z boson couplings. A second program, called *MegaZ*, will be performed at the centre-of-mass energy of $\sqrt{s} = 160$ GeV reaching the WW production threshold and trying to measure the W boson mass with a precision of MeV/c^2. At higher energy, it will also be possible to measure more precisely the W boson couplings.

Afterward, the centre-of-mass energy will be adjusted to $\sqrt{s} = 250$ GeV to perform a study on the Higgs boson couplings, as well to measure its the quantum numbers. At this energy, the Higgs boson is mainly procduced via Higgs-strahlung. The measurement is done thanks to the recoil mass independently of the Higgs decay products.

Then, for a centre-of-mass energy between 350 and 400 GeV, two studies are achievable. The WW-fusion process starts to rise and permits to measure the couplings of the Higgs boson to the W ones in order to look for deviation from the Standard Model. Moreover, this channel allows to study some rare decays. This energy range corresponds also to the threshold of the top quark pairs production. Because of the top quark life-time, the two quarks created are not in a bounded-state. By performing a threshold scan, the mass of the top quark can be measured with a precision reaching 100 MeV/c^2.

The nominal energy of the ILC is achieved at $\sqrt{s} = 500$ GeV. This energy scale is suitable to look for supersymmetry candidates and possible extended states of the Higgs boson.

An upgrade of the ILC to reach the centre-of-mass energy $\sqrt{s} = 1$ TeV is also scheduled. Up to 1 TeV, new measurements are possible, such as the coupling of the Higgs boson to the top quark, the Higgs boson self-coupling, or is compositeness. Although, search for new exotic particles and physics beyond the SM is possible.

The table 3.1 summarises the different physics programs at the ILC for the different energy reachable.

Energy (GeV)	Reaction	Physics Goal
91	$e^+e^- \to Z$	ultra-precision electroweak
160	$e^+e^- \to WW$	ultra-precision W mass
250	$e^+e^- \to Zh$	precision Higgs coupling
350 - 400	$e^+e^- \to t\bar{t}$	top quark mass and couplings
	$e^+e^- \to WW$	precision W couplings
	$e^+e^- \to \nu\bar{\nu}h$	precision Higgs couplings
500	$e^+e^- \to f\bar{f}$	precision search for Z'
	$e^+e^- \to t\bar{t}h$	Higgs coupling to top
	$e^+e^- \to Zhh$	Higgs self-coupling
	$e^+e^- \to \tilde{\chi}\tilde{\chi}$	search for supersymmetry
	$e^+e^- \to AH, H^+H^-$	search for extended Higgs states
700-1000	$e^+e^- \to \nu\bar{\nu}hh$	Higgs self-coupling
	$e^+e^- \to \nu\bar{\nu}VV$	composite Higgs sector
	$e^+e^- \to \nu\bar{\nu}t\bar{t}$	composite Higgs and top
	$e^+e^- \to \overline{t}t^*$	search for supersymmetry

Table 3.1 – Summary of the major processes that will be studied at the ILC for different energies[6].

3.2 Higgs physics

The Higgs boson found at the LHC has to be characterised more precisely. One of the goal study at the ILC is to determine if the particle found is compatible with the one defined by the Standard Model, or if other states exist. The measurement of the Higgs boson couplings to the Standard Model particle is one of the key to verify the exactness of the mass generation mechanism described by this theory and to open the door to any proof of physics beyond the Standard Model. The production, the decay modes of

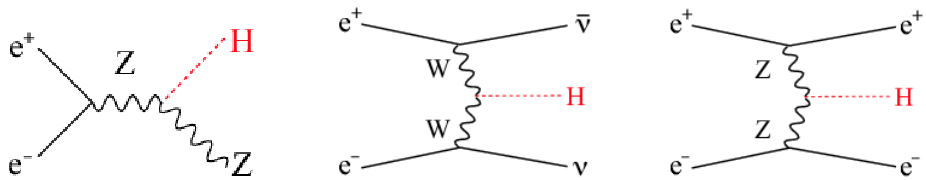

(a) Higgs-Strahlung **(b)** WW-fusion **(c)** ZZ-fusion

Figure 3.1 – Feynman diagrams of the main Higgs production at the ILC[5][42].

the Higgs boson, as well as the measurement feasible are presented below in the case of the ILC.

3.2.1 Production of the Higgs at the ILC

Due to the beam structure at the ILC, the Higgs boson is accessible by direct measurement. The production of the Higgs boson defined by the Standard Model is done via three major processes: the Higgs-strahlung (see figure 3.1a), the WW-fusion (see figure 3.1b) and the ZZ-fusion (see figure 3.1c).

$$\textbf{Higgs-strahlung:}\ e^+e^- \to ZH \to f\overline{f}X$$

$$\textbf{WW-fusion:}\ e^+e^- \to \nu\overline{\nu}W^+W^- \to \nu\overline{\nu}H$$

$$\textbf{ZZ-fusion:}\ e^+e^- \to e^+e^-ZZ \to e^+e^-H$$

The figure 3.1 summarises the different Feynman diagrams of the Higgs boson production.

At the centre-of-mass energy $\sqrt{s} = 250$ GeV, the Higgs-strahlung is the dominant process and occurs via a s-channel. Its cross-section falls off as $1/s$ as the centre-of-mass energy $\sqrt{s}$ increases. Contrary to the Higgs-strahlung, the WW-fusion and the ZZ-fusion are t-channel processes which have a cross-section growing logarithmically with the centre-of-mass energy. Thus, at 250 GeV, the cross-section of the WW-fusion is one order smaller than the Higgs-strahlung and the ZZ-fusion is negligible. Nevertheless, around 500 GeV, the WW-fusion and the Higgs-strahlung have the same cross-section, which is around 120 fb. The figure 3.2 shows the cross-section production of the Higgs at the ILC regarding the energy of the collision.

The WW-fusion occurs only with left-handed electrons associated to right-handed positrons. Thus, by modifying the beam's polarisation, the signal mixture can be changed, as well as the background processes.

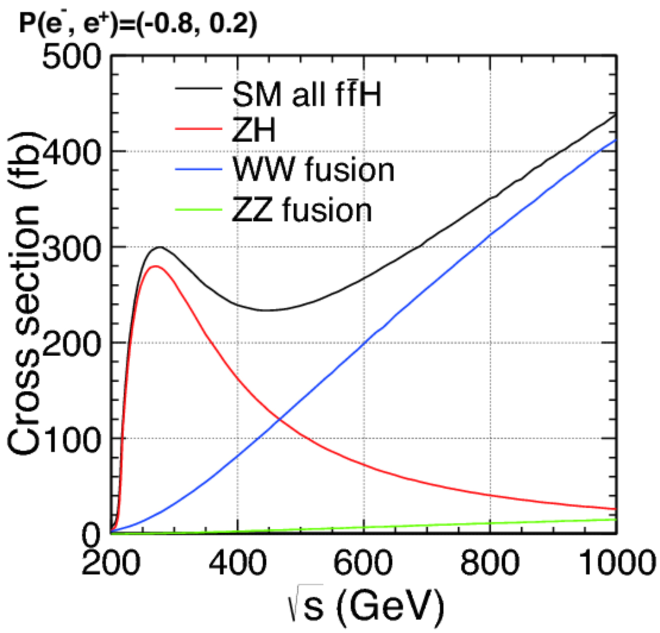

Figure 3.2 – The cross section production of the Higgs boson with a mass of 125 GeV[5].

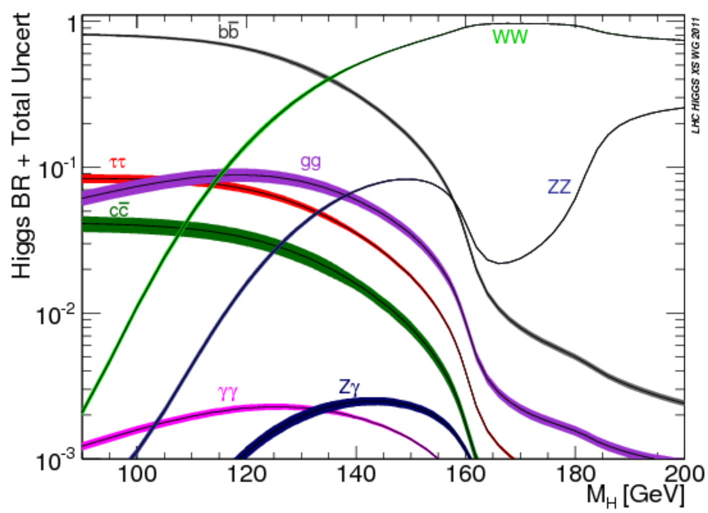

Figure 3.3 – The Higgs branching ratio with the branching ratio uncertainties for the Higgs mass varying from 80 to 200 GeV[14].

3.2.2 Decays of the Higgs

At the LHC, only the decay $H \to b\bar{b}$ is observed under special kinematics. The other decay states are challenging to separate from the background. Thanks to the properties of the ILC beams, the couplings of the Higgs to the particles of the SM is measurable. Thus, the following decay are available: $b\bar{b}$, WW, ZZ, gg, $c\bar{c}$, $\tau\tau$, $\gamma\gamma$, γZ. The observation of the $H \to c\bar{c}$ is one of the constraint parameter to build the detectors, specifically, the vertex detector that should be able to distinguish the vertices coming from the b-quarks to the ones coming from the c-quarks. The figure 3.4 depicts the mass-coupling relation of the Higgs boson to the particles of the SM. The SM nature of the Higgs boson will be tested by looking for any deviations from its fermionic coupling. A deviation might indicate multiple states for the Higgs boson.

Not clear enough

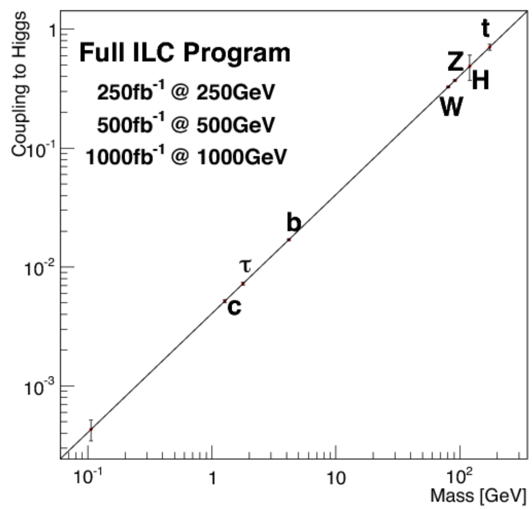

Figure 3.4 – Mass-coupling relation of the Higgs boson to the particles defined in the standard model[42].

3.2.3 Higgs studies

The first study will be at the peak production of the Higgs-strahlung. The well defined four-momentum initial state allows to measure the Higgs boson mass regardless its decay products. The Higgs invariant mass M_H can be calculated by using the recoil technique:

$$M_H^2 = s + M_Z^2 - 2\sqrt{s}\,(E_1 + E_2) \tag{3.1}$$

Where M_Z is the mass of the Z boson, E_1 and E_2 are the energy of the Z decay products. This technique works well for the Z boson decaying into leptons at the centre-of-mass energy $\sqrt{s} = 250$ GeV. However, at this centre-of-mass energy, this method can not be performed for a Higgs decaying into quarks. The Z boson and the Higgs boson are produced almost at rest, thus, the identification of the jets coming from the Z boson to the ones coming from the Higgs boson is more difficult. Nevertheless, at higher energy ($\sqrt{s} = 500$ GeV), the two bosons are enough boosted to separate their jets and ten to apply again the recoil mass. Depending on the decay channel of the Z bosons, the statistical precision on the mass measurement varies between 40 MeV (for $Z \rightarrow \mu^+\mu^-$) to 80 MeV (for $Z \rightarrow e^+e^-$) and can reach 32 MeV by combining the two results.

The spin and CP measurement are also going to be performed. The LHC has excluded the possibility of spin 1 boson, thanks to the measurement of the di-photon channel. At a centre-of-mass energy $\sqrt{s} = 250$ GeV, the cross-section of the higgs-strahlung depends on the spin and CP numbers. For example, if the spin is 0 and the CP even, the cross-section s If spin 0 and CP-odd: cross section

3.3 Analysis of simulated data

Due to the restricted time to conduct the thesis, this section is introducing the tools to perform an analysis of some simulated data at the ILD. The results shown are not the latest and were already demonstrated. Nevertheless, the philosophy to perform a study of the Higgs production at the center-of-mass energy $\sqrt{s} = 350$ GeV and a luminosity of 250 fb^{-1} is here presented.

3.4 Simulation set-up

Monte Carlo simulation and analysis software framework were developed for the linear collider community.

ILCSoft

The ILCSoft provides a large variety of software packages which were developed for the linear collider community[25]. It includes software for Monte-Carlo simulation, as software for test beam analysis (see section ??) and other tools. The main package is the Linear Collider I/O (LCIO), a persistency framework and event data model for the linear collider detector studies[29]. It provides a common data format and event data model for both the simulation studies and the analysis framework in order to share results and compare reconstruction algorithms. A C++ software framework called Modular Analysis and Reconstruction for the LINear collider (Marlin) is used for the reconstruction and the analysis by using the LCIO data format. Each tasks are structured into module called processors. A steering file written in XML is used to select the processors to use and the order of their execution time. An other package is GEometry Api for Reconstruction (GEAR). It is use as a geometry detector toolkit. A steering file is in charge to perform the interface of the detector geometry during the data reconstruction and the analysis.

The Monte-Carlo simulation is performed in three steps. The first one consists to generate the physics events of electron/positron collisions. The generation of Mont-Carlo events are performed with WHIZARD. This software includes Standard Model processes, as well as a large variety of BSM models. For the purpose of the ILC, it can simulate the beamstrahlung, the Initial State Radiation (ISR) and the beam polarisation. Although the hard interaction are simulated thanks to WHIZARD, the hadronisation and fragmentation are implemented via PYTHIA.

Afterward the physics events are generated, the particle interaction inside the detector is simulated with MOKKA. The software is based on GEANT4 simulation toolkit and is par of the ILCSoft. For the analysis, the detector model used is ILD_o1_v05. This model simulates the dead areas due to cabling, cooling system and mechanical structure and has a silicon-tungsten electromagnetic calorimeter, as well as an analog hadronic calorimeter.

Finally, the events are reconstructed thanks to Marlin.

3.4.1 Signal

The $\nu\nu H$ final state is produced via Higgs-Strahlung and WW-fusion. The leading order Feynman diagrams are shown on figure 3.1a and 3.1b.

3.4.2 Background processes

The hypothesis is to have a final state consisting of two jets coming from the decay of the Higgs boson plus missing energy from two neutrinos. Are considered as background, the events with the same final states as the signal and the events with a similar detector response.

W-boson pair production
- Semi-leptonic decay
- Hadronic decay

Z-boson pair production
- Hadronic decay
- Leptonic decay
- Hadronic decay with missing energy

Single W-boson production

Single Z-boson production
- Hadronic decay
- Hadronic and electron/positron decay

Higgs-strahlung
- Hadronic decay
- Leptonic decay

3.4.3 Event reconstruction

- Identification of isolated leptons to remove some of the background processes
- Look for jet-like objects in the forward region corresponding to low pT hadrons coming from $\gamma\gamma$ interactions.
- Jet clustering and flavor tagging

3.4.4 Event selection

Chapter 4

Double-sided VXD: PLUME

Since the end of the 1960's, the development of position sensitive silicon sensors has permitted to confirm the prediction of the Standard Model (SM) with a high precision, as well as the discovery of the top quark. These sensors, called Vertex Detector (VXD), are in charge to track the particles down to their decay vertices. The design of such device is driven by the physics requirement of the experiment and is playing a crucial role at the International Linear Collider (ILC). For example, one flagship measurement is the study of the Higgs boson couplings to the fermions and other bosons. This can be achieved only with a precise heavy flavor tagging and the ability to separate the b quarks from the c quarks. Actually, the lifetime of the two quarks is of the same magnitude (1.3^{-12} s for the b quark and 1.1^{-12} s for the c quarks), leading to very close decay vertices.

Along this chapter, the role of the vertex detector and the physics requirements to develop one for the ILC environment will be presented. Then, the different options of the International Large Detector (ILD) are shown, to focus on the double-sided ladders developed by the Pixelated Ladder with Ultra-low Material Embedding (PLUME) collaboration. To finish, the principle of Complementary Metal Oxide Semi-conductor (CMOS) sensors and their use in physics are described.

Contents

4.1 The ILD vertex detector specifications

The VXD is the closest sub-detector to the interaction point (IP) in charge of reconstructing the vertex by extrapolating particles back to their origin of production. This detector should be optimised to track particles in a high-density environment and to be able to extract the tracks from the different particles, especially the b and c quarks in the case of the ILC. The reconstruction of the displaced vertices should be efficient enough to perform a good flavour tagging. Therefore, the detector has to measure particles with a lifetime in the picosecond regime, representing a decay length between 150 and 500 μm. The minimum distance of the first VXD layer is determined by the beam pipe radius, and the background induced by beamstrahlung, to limit the pixel occupancy. This sub-detector has a central role in the tracks' reconstruction. Depending on the option chosen, the VXD has to provide five or six points of measurement with a very high precise spatial resolution. For the studies requiring vertex charge identification, it should be able to reconstruct low-momentum and very forward tracks.

4.1.1 Physics requirements

The ideal VXD should be made of sensors with a fine granularity in order to increase the ability to distinguish two nearest particles. The mechanical structure of the detector should provide a good stiffness and stability of the whole system but has to be at the same time as light as possible to reduce the interaction of the particles traversing it, before they reached another part of the main detector. As well, in order to reduce the unwanted interactions, the sensor technology used has to have a low power consumption to avoid any special cooling system which can have a bad impact on the material budget. The design of such detector, like the minimal distance of the first layer to the IP and the spacing between different layers, is determined by both the beam background and the physics to study. The flavour tagging ability, the vertex charge measurement and tracking, and the displaced vertices reconstruction are the main physics parameters driving the design. The distance of closest approach of a particle to the colliding beam is called the impact parameter and the resolution achievable by the detector is described by the formula 4.1[7].

$$\sigma_{IP} = a \oplus \frac{b}{p \sin\theta^k}, \text{ with k} = \begin{cases} \frac{3}{2} & \text{in the } R-\Phi \text{ projection} \\ \frac{5}{2} & \text{in the z projection} \end{cases} \tag{4.1}$$

Where θ is the track polar angle, a and b are explained in the following.

The first term a is the impact parameter resolution of the sensors used for the VXD, which is linked up to the radius of the inner R_{int} and outer R_{ext} layers and the single point resolution $\sigma_{s.p.}$, as described in equation 4.2.

$$a = \sigma_{s.p} \frac{R_{int} \oplus R_{ext}}{R_{ext} - R_{in}} \tag{4.2}$$

In the case of the ILD, the single point resolution should not be higher than $\sigma_{sp} \simeq 3\mu$m, leading to an impact parameter with a resolution of the order of $a \simeq 5\mu$m.

The second term presented in the equation 4.3, is related to the multiple scattering inducing an uncertainty on the impact parameter. It depends on the charge Z of the impinging particle, the material crossed by the particle $\frac{x}{X_0 \sin\theta}$ and the distance of the innermost layer to the IP. Depending on the momentum or the crossing angle of the incoming particles, the two parameters are more or less important. For low momentum particles or crossing particles with a shallow angle, the b parameter becomes important, while for higher momentum a dominates.

$$b = R_{int} \frac{13.6 MeV/c}{\beta c} Z \sqrt{\frac{x}{X_0}} \left[1 + 0.036 ln \left(\frac{x}{X_0 \sin\theta} \right) \right] \tag{4.3}$$

For the ILC purpose, the ILD-VXD should reach an impact parameter resolution better than 5 μm and a b parameter better than 10 μm GeV/c. This precision on these parameters were never obtained before in other experiments. As a comparison, the resolution parameters for the LHC are: $a = 12$ μm and $b = 70$ μm GeV/c.

4.1.2 Layout of the vertex detector

The VXD will be made of 12 cm long ladders arranged cylindrically in concentric layers to form long-barrels surrounding the IP, contrary to the SiD vertex detector with a design based on a 5 layers barrel, four endcap disks and three additional forward pixel disks[10]. Two different geometries are under consideration for the ILC-ILD, nevertheless, they are both based on long ladders. The first option is based on five single-sided layers with a material budget not exceeding 0.11 % of X_0 per layer. The five layers are in a radius range varying from 15 mm for the first layer to 60 mm for the last one. The second option is based on three double-sided layers. The material budget should be less than 0.16 % of X_0 for one detecting face. The mechanical structure, which holds the two layers, is 2 mm thick and will be in a radius range varying from 15 to 60 mm.

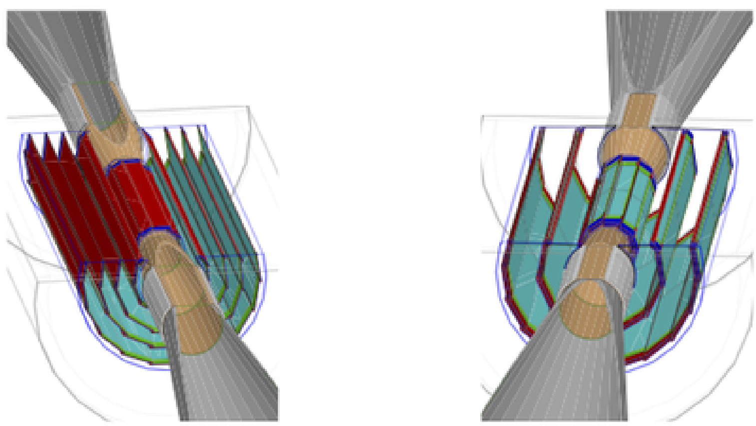

Figure 4.1 – Overview of the two vertex detector option for the ILC. On the left, it is made of five single sided layers, whereas the right one represents three double-sided layers.

Both geometry designs are based on pixel sensors instead of strips detectors. A non-exhaustive list of the possible technologies are presented below:

FPCCD

The Fine Pixels Charged Coupled-Device (FPCCD) [11] is based on the Charged Coupled-Device (CCD) processes. The sensor is using small pixels size (approximately $\sim 5\mu$m) to provide a sub-micron spatial resolution and an excellent capability to separate two nearby tracks. Its thickness is 50

μm and the epitaxial layer (15 μm thick) is completely depleted to limit the charge spreading around pixels and to reduce the number of hits per pixel. However, the CCD architecture provides slow readout and the matrix will be read between consecutive bunch trains, helping to reduce the power consumption and avoiding beam induced RF noise. The FPCCD are planned to be operated at -40°C.

DEPFET

The Depleted P- Channel Field Effect Transistor (DEPFET) [38] is an Active Pixel Sensor (APS) in which field effect transistors are incorporated into each pixel. The single point resolution is ~ 3 μm for pixels with a size of 20 μm. The silicon itself is used as sensitive part but also as a mechanical structure, minimising the support and services. The sensor is completely depleted of free charged carries thanks to a voltage applied to the thickness. The rolling-shutter approach is used for reading each row and the column readout is done by two auxiliary Application-Specified Integrated Circuits (ASICs).

The DEPFET technology is the one chosen to build the vertex detector of the BELLE-II experiment[2].

CMOS

Different options for CMOS pixel sensors are studied, such as the 3D integrated CMOS, but due to the context of this thesis, the work will focus on the CMOS sensors based on the Minimum Ionizing MOS Active pixel sensor (MIMOSA) architecture developed by the IPHC of Strasbourg. This technology is described in section 4.3.

For all the technologies, the sensors' power consumption has to be minimised in a way to reduce the cooling system and in the same time the added material budget in the sensitive detector volume. As it was shown on the figure 2.2 of the chapter 2, the bunch train will last less than 1 ms for a dead time of 200 ms. Two possibilities are envisaged to benefit from the beam structure. The first one consists to store the hits information thanks to a time stamp during the bunch crossing and to read out the data after the last collision. This method might be used by the FPCCD technology due to the slow integration time of the CCD. Another solution is to use power-pulsing. Right after the last collision, the sensors are switched off or the power consumption is reduced as mush as possible, and before the first collision, the sensors is switch on again. This pulsing method is studied by different collaborations.

Another aspect not discussed yet is the radiation tolerance of the detector, which is directly related to the beam background. The first layer is the most affected by the background and it should have a high radiation tolerance. The required radiation tolerance is about 1 kGy for the total ionising dose and a fluence of $10^{11} n_{eq}/cm^2$[9].

The efficiency of the VXD has also to be excellent in order to maximise the tracking performances. The efficiency is defined here as the ratio of detected particles over all the particles crossing the detector. If one layer of the vertex detector misses a hit, the track reconstruction will be less accurate

Cooling system, integration time, radiation tolerance, electromagnetic interference

To summarise, the expected parameters expected for the ILC are:

- An excellent impact parameter resolution: $a \sim 5\mu$m and $b \sim 10\mu$m
- A material budget not exceeding 0.1 % X_0 per layer for the single-sided option (0.16 % X_0 for the double one)
- Radius of the first layer $\sim$ 15/16 mm

4.2 PLUME

The Pixelated Ladder with Ultra-low Material Embedding (PLUME) project aims to produce double-sided ladder prototypes with respect to the ILC requirements[37]. Three labs in the Europe are involved: the IPHC-PICSEL in Strasbourg, the University of Bristol and DESY in Hamburg. The collaboration is studying the feasibility to build such vertex detector using MAPS thinned down to 50μm and is exploring the benefits of this design. Strasbourg is in charge to develop and mount the sensors on the modules, to take care of the readout and the Data AcQuisition (DAQ), and to provide a cooling system. The mechanical design, stability measurements and building the ladders are done by the University of Bristol, while DESY has studied the ladder mock-up, performed power-pulsing tests and is now characterising and validating the modules in the lab. In 2016, DESY has provided the opportunity to test the ladder in real conditions thanks to the test beam facility and the possibility to use the DAQ software developed at DESY: EUDAQ.

REF: EUDAQ

4.2.1 Design and goals

The figure 4.2 illustrates the design of a PLUME ladder. The ladder structure is defined by the sensors arrangement on the mechanical structure (positioned next to each other). In this design, the stiffener is a 2 mm thick Silicon Carbide (SiC) foam which has a density varying between 8 % and 4 % (depending on the ladder version) and could be reduced to only 2 or 3 %. The choice of this foam is a good compromise between the stiffness and the thickness compare to other materials. The figure 4.3 is representing the structure of this foam. It is macroscopically uniform and has the advantage to be easily machinable. Nevertheless, it has a low thermal conductivity (50 W/m/K) and can't be used to dissipate the heat. On each side, a low mass flex-cable is glued, which is used to connect the sensors for powering and managing them. It is made of copper traces coated in Kapton, but new prototypes using aluminum traces are developed and currently tested in order to reduce the material budget. The ladder embeds twelve sensors, six on each face, that are glued and connected to the flex cable. On one edge of the flex-cable, a single Zero Insertion Force (ZIF) connector is used to link the ladder to the external board servicing, via a jumper cable. For the moment, the design is dedicated to the MIMOSA-26 sensors thinned down to 50μm but it can be adapted to any kind of MAPS sensors having the same thickness. Although the MIMOSA-26 has a spatial resolution better than 3μm (see subsection 4.3.4), the integration time is not suited for the bunch train structures of the ILC.

REF Joel paper

The aims of the collaboration are to build ladders with a material budget better than 0.35% of X_0 for a spatial resolution better than 3μm, and thus to evaluate the benefits of a double-sided measurement.

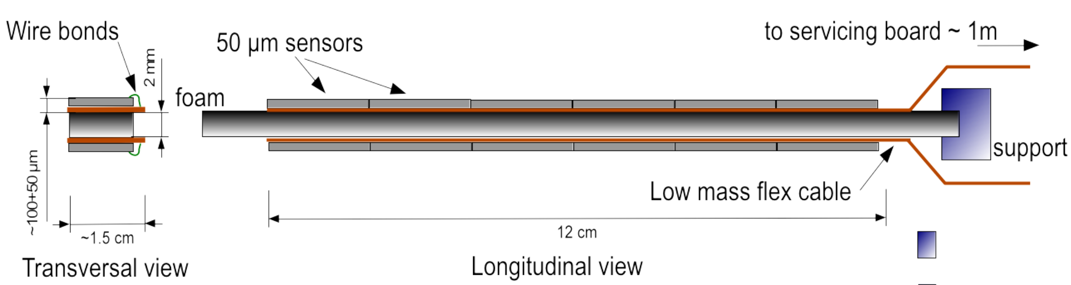

Figure 4.2 – Side view (transversal and longitudinal) of the PLUME mechanical structure.

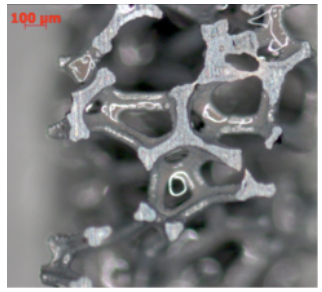

Figure 4.3 – Microscopical view of the silicon carbide foam structure.

4.2.2 Prototypes

Since 2009, the collaboration is studying the design, the production, the impact of the mechanical structure on the ladder's performances, but also how to power and control the sensors together. The first ladder prototype, called version-0 (V-0) was developed and tested in 2009. The purpose of this prototype was to settle the fabrication and the test beam procedures, without trying to reach the desired material budget goal. Two MIMOSA-20 analog output sensors were mounted on each side of a stiffener, providing a 1×4 cm^2 sensitive area. The prototype was tested in 120 GeV pion beam at the CERN-SPS and the results have demonstrated the benefits of the double-sided measurement on the spatial resolution, which is improved by about 25%[35].

Then in 2010, a second prototype featuring a design closer to the wanted goal, called version-1 (V-1), was developed. Each module of the ladder was made of Kapton flex-cable with a thickness of 0.14 mm, using copper traces. They are denoted Optiprint-Kapton-Flex-cable (OKF), where Optiprint is the vendor of these flex-cable. It is the first version to embed six MIMOSA-26 binary output sensors working simultaneously on each side of the stiffener. The material budget is estimated to be 0.65 % of X_0 in the sensor's sensitive area. The aim of this prototype was to validate the operation of multiple sensors in a chain. Two ladders were tested in real conditions. The first one was tested with 120 GeV pions at CERN-SPS in 2011, while the second ladder was tested in April 2016 with up to 5 GeV positrons at DESY in Hamburg. The DESY test beam results are presented in chapter ???, while a specific study of the sensor's deformation observed at CERN is discussed in chapter ???.

At the beginning of 2016, the third prototype versions were mounted but have not yet been completely tested. In fact, this new version is divided into two sub-versions: one using copper traces and the other one aluminum

Figure 4.4 – Front view of the ladder version-1 made in 2010 in its holding box. On the left, there is the connector to the output board servicing, on the right a connection to blow air on the module. As this version was not made with a mirrored design, the flexible cables are not entirely overlapping and the SiC foam can be seen (in black here).

traces. Nevertheless, both sub-versions have a new design featuring reduced traces thickness to have a narrower flex-cable (18 mm width) adjusted to the sensors width in order to minimise the dead areas. The flex-design has slightly changed to have a mirrored geometry (figure 4.5) and a straight geometry in order to minimize the dead area too and have a better alignment solution. The stiffener is made of a lower density SiC foam reducing the global material budget.

The table 4.1 summarises the material budget reached by the different prototypes.

4.2.3 Perspectives

Although the collaboration has shown their expertise to build light mechanical structures, more tests and optimisations have to be done. MIMOSA-26 sensors are not designed to match the ILC specs. The integration time of this sensor is 115.2 μs, whereas the bunch train last only 0.95 ms (bunch

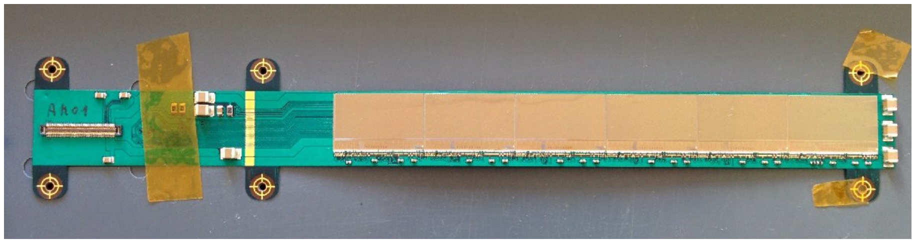

Figure 4.5 – Picture of the first mirrored module made with aluminum traces. The cable width is adjusted to the size of the sensor.

Layer	budget (% X_0)		
	V-0	V-1	Goal
Sensor	0.053	0.053	0.053
Flex-cable	0.524	0.150	0.034
Passive components	0	0.033	0.033
Stiffener (foam)	0.764	0.175	0.087
Total	1.926	0.654	0.334

Table 4.1 – Estimation of the material budget for the different prototypes of the PLUME ladder.

crossing spaced out by 337 ns), a new CPS with a faster integration time has to be integrated. Another problem of the MIMOSA-26 sensors is that they are not suited for a power pulsing. As a reminder, the principle of the power pulsing is to reduce the consumption of the sensor during the 200 ms dead time. Nevertheless, a power-pulsing study on a single Mi-26 sensor has been done and the results have shown that the nominal supply voltage of the MIMOSA-26 can be lowered from 3.3 V to 1.85 V without losing the sensor's registers. The fake hit rate measured was close to the one obtained in normal conditions after the sensor reaches a stable operation. Moreover, the power consumption was reduced by a factor 6.34[28].

A complete power-pulsing study of the whole ladder in the lab has to be done in order to make sure that the sensors are still behaving correctly. If the first results are comforting, the power-pulsing will be tested under real conditions with a high magnetic field. The impact of the Lorentz forces due to the coupling of the power-pulsing and the magnetic field is going to be studied, especially is this structure will induce unwanted deformations or vibrations.

The collaboration is considering to embed the sensors directly inside the multi-layer micro-cable[8]. The chips are glued on the first polyimide substrate layer, then the metal layer is deposited on top of it and the metal traces are directly connected to the chips pads. Then an insulator is added to the module. The advantages of this technique are, firstly, the direct connection of metal traces to the pads that avoid wire-bonding and can reduce, at the same time, the width of the module. And secondly, this structure has the advantage to apply the mechanical stress on the polymer wrapping, thus reducing it on the sensor.

A closer perspective for the collaboration is to integrate two ladders in the physics commissioning of the BEAST experiment at KEK. The version-2 ladder will be used but a second option is foreseen. MISTRAL sensors will be mounted on the flex-cable instead of the MIMOSA-26. These sensors have a bigger sensitive area, a faster integration time ($\sim 20\mu$s) but a worth spatial resolution ($< 10\mu$m) due to the pixel size (pitch of $36\text{x}62.5\mu\text{m}^2$).

4.3 Integration of CMOS sensors

The PICSEL group of the IPHC at Strasbourg is developing since 1999 CMOS sensors called MIMOSA for *Minimum Ionizing MOS Active pixel sensor*. They are semi-conducting pixel sensors based on the APS, an alternative to the CCD developed at the beginning of the 1990's by the imaging industry and used nowadays for the smartphone's cameras. One particularity of the sensors developed by Strasbourg is that the different region of the CMOS, such the sensitive area or the electronic layer where the signal is processed, are made of the same material. This device is called then Monolithic Active Pixel Sensor (MAPS) and the different layers are:

- A substrate providing a mechanical stability;
- An epitaxial layer which is the sensitive volume of the sensor;
- An electronic layer where are located the diodes collecting the charges and the microelectronic processing the signal.

The motivation to use this technology or any other silicon sensor in particle physics is due to the minimum energy needed to create an electron/hole pair by a traversing particle. In silicon, this minimum energy is only 3.6 eV, while for a gaseous detector, it is close to 30 eV.

4.3.1 Charges creation and signal collection

The CMOS sensor can detect crossing particles thanks to their structure, but also to the interaction of particles with matter. When a particle is traversing a layer of matter, it loses energy via interactions with electrons and nuclei. Due to the size of a MAPS, it loses only a small fraction of its energy, and the energy loss can be described by a Landau. A Minimum Ionizing Particle (MIP) creates 80 electrons per microns inside the silicon.

At the beginning, the microelectronic industry has insulated the transistors from the substrate thanks to a high resistivity layer, called the epitaxial layer. The development of CMOS sensors was accelerated due to the properties offered by these semiconductors.

The CMOS sensors developed by the IPHC at Strasbourg are called monolithic MAPS sensors because the different layers of the sensor are made in one block of the same material, but with different doping. The structure of the sensor is a highly doped P+ substrate made of a moderate quality silicon. The crystal structure contains a lot of defects, hence the recombination rate of charge carriers is high. Above the bulk, a low-doped P- layer is grown. The silicon used has a good quality, thus the charge carriers have less chance to recombine. It is the sensitive part of the sensor and is called the epitaxial layer. On top of it, an N-well implant has the role of the charge collection. The interface between the N-wells and the epitaxial layer forms a P-N junction called a collection diode. A depleted area is created by this junction, on which the charge carriers are attracted. Nevertheless, this P-N junction is only one part of the pixel. Next to the N-well implants are sitting highly doped P-well in charge to reflect the charge carriers to the implants. The difference of doping between the bulk and the epitaxial layer is also used to reflect the charge carriers to the collection diode.

The typical doping concentration are $10^{15}\mathrm{at/cm^3}$ for the epitaxial layer, $10^{19}\mathrm{at/cm^3}$ in the substrate and $10^{17}\mathrm{at/cm^3}$ for the other layers. The doping concentration defines the size of the depleted region. For this doping concentrations, only a small region around the P-N junction is depleted, while the epitaxial layer is mainly undepleted. As no external voltage is applied to the sensor to increase the depleted region, the charge carriers created by crossing particles are thermally diffused into the epitaxial layer to the diode. Nevertheless, the different doping levels produce a built-in voltage defined as:

$$V_b = \frac{kT}{q} ln \left(\frac{N_{p+}}{N_{p-}} \right) \tag{4.4}$$

The built-in voltage depends on the Boltzmann constant k, the temperature T, the elementary charge q and the different concentrations doping $N_{p\pm}$ of the interface. Due to the different doping levels, the electrons are restricted to diffuse inside the sensitive volume, to be then guided towards a collection diode. One effect of the thermal diffusion is that the average path of the electrons in the epitaxial layer is longer than the one they would have in a fully-depleted sensor. Hence, the probability of recombination between an electron and a hole is increasing. Also, the charges tend to spread more around neighboring n-well. Therefore, the charge collection efficiency is lower than the fully-depleted sensor.

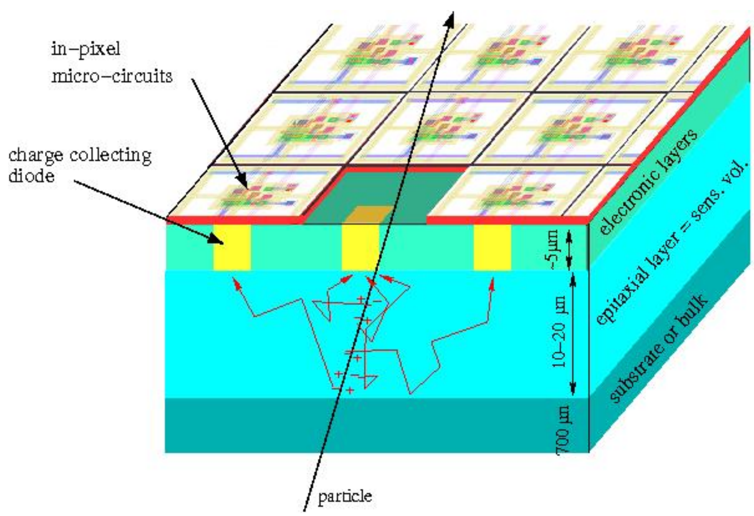

Figure 4.6 – Drawing of MAPS structure representing the different layers of the sensor and the path of charge carriers in the epitaxial layer.

4.3.2 Pros and cons of the technology

The CMOS sensors have several interesting properties. First of all, the fabrication cost is lower than other pixel technologies due to the industrial processes used to build the sensors. Therefore, many prototypes and bigger matrices can be built, while benefiting from the industrial experience. For example, the imaging industry has developed smaller and smaller grid size and a pitch size of ten microns can be achieved.

Secondly, due to the size of the depleted area, the charge carriers tend to spread more over neighboring pixels. On the one hand, the signal collected per pixel is smaller, but on the other hand, the reconstruction of the hit position with a centre of gravity algorithm is improving the spatial resolution. To give an idea, a binary output sensor with a pitch of 18.4 μm can achieve a spatial resolution better than 3 μm.

Thirdly, the distinct doping of the different layers is responsible for the reflection of the charge carriers to the collection diodes. However, only the interface between two different doped regions is responsible for this reflection. Thus, the substrate can be thinned down to few microns leading to a sensor with a thickness of 50 μm, while keeping the possibility to manipulate them. In this way, the material budget can be reduced down to 0.053% X_0.

Nevertheless, the thickness of the epitaxial layer (usually between 10 and 15μm) and the small depleted region are responsible for a small charge collection. As a matter of fact, a MIP is creating 80 electron/hole pairs per microns, so the number of charges collecting by the diode is of the order of a thousand electrons. Hence, the signal created is only a few millivolts and low noise electronics have to be used for processing the signal.

CMOS sensors are sensitive to ionizing and non-ionizing radiations that degrade the sensor properties. The non-ionizing radiations are damaging the crystal structure of the epitaxial layers, creating defaults in the lattice. The recombination rate is increasing and reduces the signal collected. To avoid this effect, two solutions are possible. The first one is to reduce the size of the pixels in order to decrease the path of the particles from the epitaxial layer to the collection diodes. Nevertheless, the cost to build sensors with a smaller pitch is increasing. The second solution is to increase the resistivity of the epitaxial layer to expand the depleted area.

The ionizing radiations are responsible for charges accumulation in the electronic layer. The leakage current is increasing in the pixel and diode collection. To reduce the leakage current, smaller diodes can be used to reduce the impact of the leakage current but as it was explained before, the cost of fabrication is increasing.

4.3.3 Signal processing

If no charge is collected by the pixel, the voltage at the equivalent capacitor of the diode is evolving because of the leakage current inherent in the junction. The pixel reading can be done in two different ways, depending on the method used to minimise the leakage current effect. Currently, two pixel's architectures are used to compensate the diode's leakage current: the *3 Transistors pixel design*, mainly used in imaging, and the *self-biased pixel design*. The circuit diagram which is shown on the figure 4.7 represents the two methods to design pixel.

The first one, presented on figure 4.7a, consists to reinitialise the collection diode's voltage to a reference voltage thanks to a *reset* transistor, denoted M1 on the diagram. This method works in two steps. Firstly, the M1 transistor is closed and the charge of the equivalent capacitor C_d associated to the junction P-N, represented by a diode on the diagram, is slowly decreasing because of the diode's leakage current. During this phase, the pixel is sensitive and is read. After a time interval equivalent to the integration time of the sensor, the transistor M1 is opened to recharge C_d to its initial voltage. During this time, the pixel is not sensitive. While M1 is used for the reset, M2 is used as a pre-amplifier of the signal created by the diode and M3 link up the voltage to the output of the circuit. Although this compensation method is fast, it generates a dead time for detection between two readings.

The figure 4.7b depicts the *self-biased pixel design* method[16]. It is using a P-N junction (symbolised here by a diode mounted on the other side) coupled to the N-well implant to absorb the leakage current. The inverted diode is continuously compensated the diode's leakage current, thus the dead time vanishes. While no particle is crossing the sensor, an equilibrium appears between the leakage and recharge current. A particle going through the sensor disrupts this equilibrium. The charges collected by the pixel lead to a discharge of the diode's capacitor C_d, followed by a recharge of this capacitor thanks to the second diode to reach again the equilibrium. Nevertheless, if the recharge procedure is too fast compare to the integration time, the physics signal is masked and the passage of the particle is never notified. Even if the time interval to recharge the capacitor C_d is set properly, an important charge collection per pixel could disturb the recharge phase and the pixel will reach a stable level again only a long time interval of the order of 10 ms.

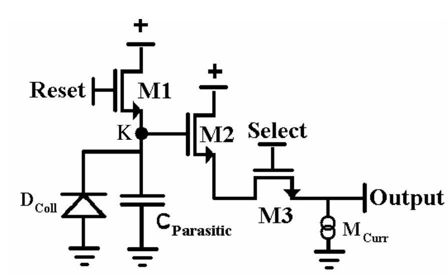

(a) Three transistors (3T) pixel design.

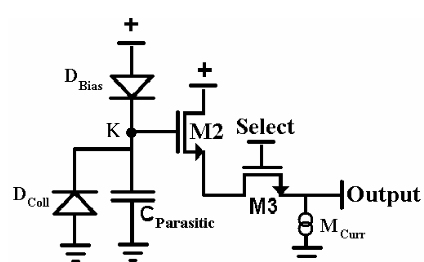

(b) Self-biased pixel design.

Figure 4.7 – Two different architectures of pixel.

Integration time and readout

For a non-depleted epitaxial layer, the charge carriers are thermally diffused to the collection diodes. The time to collect these charges in a pixel is ~ 100 ns, setting a maximal limit to read the signal. This integration time is not reachable due to other factors, like the pixel occupancy or the time needed to obtain the information of all the pixels. Also, a compromise to reach fast integration time has to be done. Faster is the sensor, more important is the power consumption of the electronic. Moreover, to reduce the integration time, a solution consists of increasing the size of the pixels. In consequence, the pointing resolution of the device is impacted. For the case of the ILC, the integration time is dictated by the pixel occupancy that should not be bigger than a percent, to stay in the using sensor's range and to be able to reconstruct the impact.

The first sensors developed were using an analog output. With this approach, the pixels were addressed sequentially and their output was multiplexing in one bus line. The advantage of such method is that the discrimination can be adjusted offline for each pixel, thus compensating the nonuniform response. Nevertheless, the integration time is depending on the operational frequency of the bus (usually 50 MHz) and the number of pixels contained in a matrix. For a sensor having millions of pixels, the integration time is then of the order of the millisecond. An analog output is then too slow for a ILC purpose.

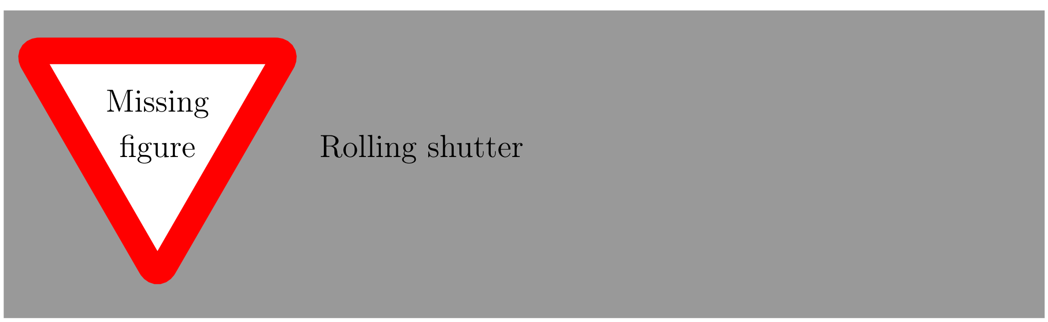

Figure 4.8 – Parallel column readout.

To overcome this problem, an approach is to group the pixels in columns and to read them in parallel. The figure 4.8 depicts the principle of this method called *column parallel readout* or *rolling-shutter*. Instead of having one bus line for the whole matrix, each column has its own bus and a data sparsification logic is integrated on the periphery of the sensor. One row is read out between 100 ns and 200 ns, independently to the number of pixels contained in it. In consequence, a matrix containing thousands of rows has an integration time of $\mathcal{O}(100\mu\text{s})$. Moreover, to increase the integration time an output memory is duplicated at the periphery of the sensor. Hence, when one line is read, the precedent one is processed by the electronics at the end of each bus line of each column. To minimise the data bandwidth, only the pixels above certain thresholds are read thanks to discriminators coupling to a zero suppression logic, called Suppression de zéro (SUZE). In this way, only the address of the first pixel hit in a row and the number of the adjacent fired ones are stored. This memory is duplicated to be able to process one row, while the previous one is read out by the outside world. In order to increase the readout speed, two techniques are conceivable[43]. The first one provides elongated pixels in the vertical direction in order to reduce the number of rows, thus degrading the spatial resolution in the same direction. The second one consists of dividing the columns into two distinct parts, which have its dedicated output.

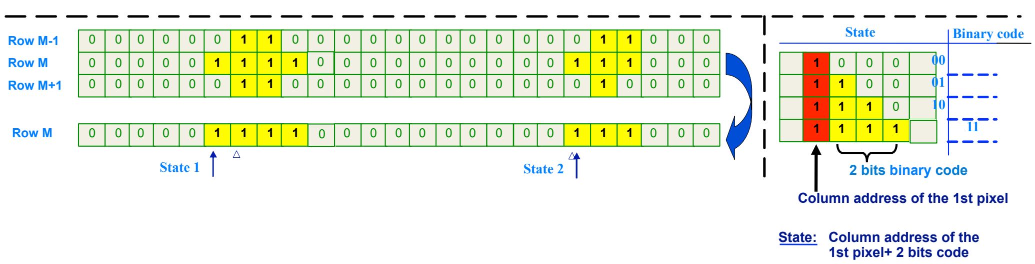

Figure 4.9 – Principle of the zero suppression logic.

Noise

The CMOS sensors are sensitive to the noise. Many factors are causing it and the different kind of noise is divided into two categories: the Fixed Pattern Noise (FPN) and the Temporal Noise (TN). The non-uniformity responses of the pixel in a sub-array is responsible for the FPN and is regarded as an offset or pedestal, which is subtracted from the pixel response to reduce the impact of this noise. The TN has different origins, as the shot noise, the pink noise or the thermal noise. The different operational phases to read the signal are contributing to the noise.

One contribution to the TN appears in the *3T pixel design* only during the reset phase. This noise arises when the transistor is open restoring the

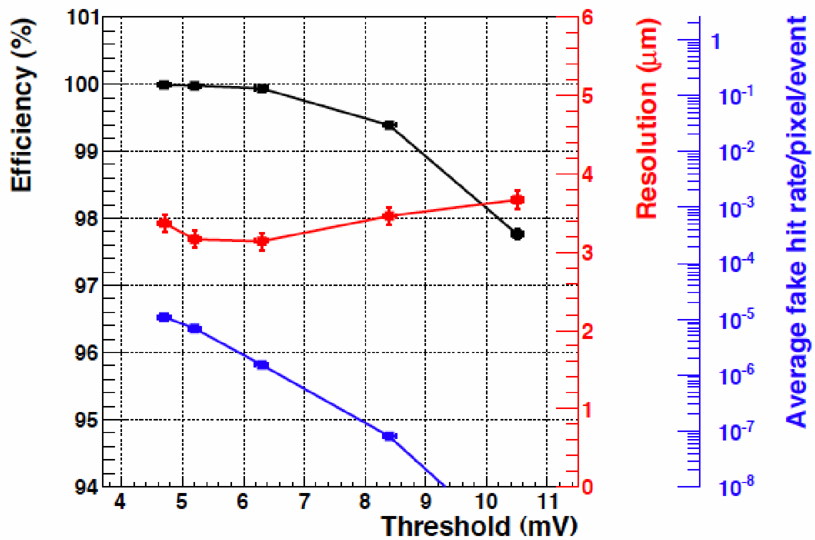

Figure 4.10 – Plots representing the efficiency, the fake hit rate per pixel and the spatial resolution as a function of the discriminator threshold.

charge of the capacitor associated with the collection diode. It is dependent on the temperature and the diode's capacitance.

The second one is the noise during integration and is caused by statistical fluctuations of the leakage current (shot noise). Faster is the integration time, slower is the shot noise contribution.

Finally, the third one arises from the readout, while the column switch and the source follower capacitors are working. This noise depends on the contribution of each capacitor.

To remove the FPN and the reset noise, a Correlated Double Sampling (CDS) is performed inside the pixel or at the bottom of the column. It consists to acquire two frames and to subtract the first one to the second one to search for possible signals. The chapter 5 describes the steps to characterise the FPN and TN and to select an appropriate Signal to Noise ratio (SNR) in order to minimise the noise contribution, and to find a range on which the sensor is working properly.

4.3.4 State of the art in high energy physics

The first full-scale digital sensor developed by the PICSEL group was the MIMOSA-26. They were designed to equip the reference planes of the EUDET beam telescope and are used since 2010 to build the PLUME prototypes. It is fabricated in the AMS 0.35μm technology, and has a matrix containing approximately 6.6×10^5 pixels, distributed in 1152 columns and 576 rows. The pixel pitch is 18.4μm and the sensitive area represents 21.2×10.6cm^2. The readout of the matrix is ensured by a rolling-shutter working at 80MHz frequency, hence the integration time is 115.2μs. The signal produces by the charge collection inside the pixel is firstly amplified. Then, the CDS technique is used to subtract successive frames before to send the signal at the bottom of the pixel array, where the signal processing circuitry is placed. Analog to digital conversion is done, coupled to a second double sampling, in order to reduce the FPN. The output of the discriminators is then connected to a zero suppression logic, in which an output memory is duplicated to ensure a continuous readout. The signal is finally transmitted to the outside world. The architecture of the MIMOSA-26 is represented by a block-diagram on figure 4.11b. The power consumption is 1.1μW/pixel and the sensor is thinned down to 50μm in order to minimise the multiple scattering inside the volume. The performances obtained with a MIMOSA-26 are shown on the figure 4.10.

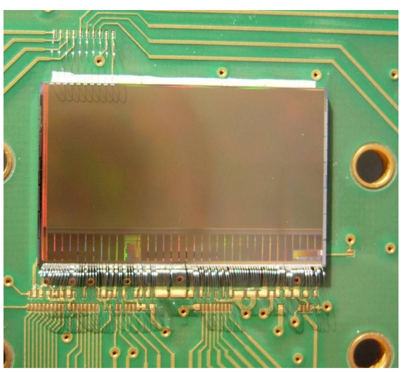

(a) Picture of a MIMOSA-26 mounted on a PCB.

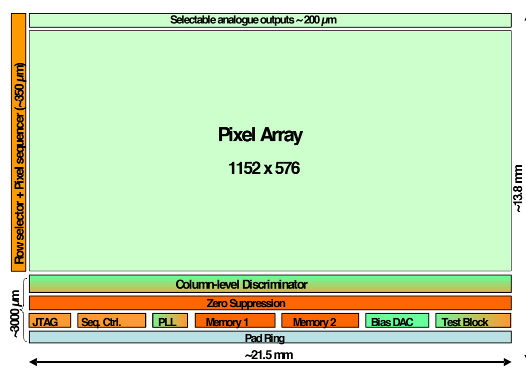

(b) Layout of the MIMOSA-26 matrix.

Figure 4.11 – Block-diagram and a picture of the MIMOSA-26

The PICSEL group has then developed digital output sensors for the pixel vertex detector at the START experiment at Brookhaven National Laboratory[]. The figure 4.12 is showing a half-section of the STAR vertex detector (subfigure 4.12a) and a MIMOSA-28 bounded on a PCB(subfigure 4.12b). They are based on the architecture of MIMOSA-26 with some modifications. The matrix contains 960 columns and 928 rows for a pitch of $20.7 \times 20.7\mu$m^2. The sensitive area is 19.7 x 19.2 cm^2, for an integration time of less than 200μs. The sensor can reach a particle detection rate of 10^6 particles/cm^2/s.

Finally, their power consumption is lower or equal to 150 mW/cm^2. The spatial resolution obtained for ULTIMATE is less than 4 μm.

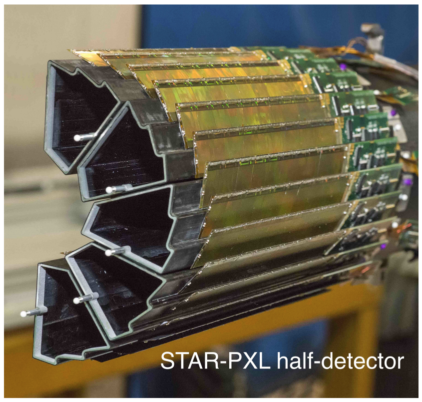

(a) Half part picture of the pixel vertex detector at STAR.

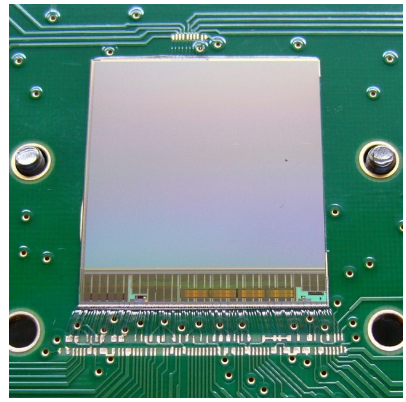

(b) ULTIMATE chip mounted on a PCB.

Figure 4.12 – Pictures of the STAR vertex detector and an ULTIMATE chip

This chapter has depicted the purpose of the vertex detector for the ILD. Different technologies were introduced, to focus specifically on the CMOS sensors and their use in high-energy physics. The PLUME collaboration aims to integrate MAPS onto light double-sided ladders, in order to reach the requirements of the ILC. The collaboration has reach different steps to produce the first full-scale ladder, which have only a material budget of only 0.35%X_0 and a spatial resolution better than 4μm. The principle of the CMOS technology was presented. The next chapter is focusing on the electrical validation of this sensors mounted onto a PLUME ladder.

Chapter 5

Basic assessments

The chapter 4 has described the PLUME project with the different prototypes that were built. Since the version-1 of PLUME, the detector is more complicated due to the six sensors on a module that have to be synchronised and the flex-cable which has a lot of thin metal traces to pilot and read the sensors. Before to perform a test in real conditions at CERN or at DESY, the device has to be validated and characterised first in the lab. This chapter is introducing the different steps from the assembly procedure performed at Strasbourg (for the module) and Bristol (for a complete ladder), to the final tests to study the sensors response, and include electrical functionality tests.

Contents

5.1 PLUME assembly procedures

The ladders are built in two steps. Firstly, two independent modules are mounted at Strasbourg, then tested at DESY, afterward, they are shipped to Bristol where the modules are glued together on a SiC foam. The assembly procedures are introduced below, as well as the visual inspection between the mounting steps.

5.1.1 Module and ladder assembly

Module assembly

The module assembly is performed at the IPHC by the microelectronics group and is done in three steps. First of all, the passive components are soldered onto a flex-cable. Then, an epoxy layer with a thickness of 300 μm is glued under the connector side. Due to the force applied by pulling and pushing the jumper cable on the ZIF connector, the epoxy layer has the role to reinforce this area and to avoid the flex-cable to be damaged. The module is then placed on a metal jig to ensure its flatness thanks to a vacuum suction. The next step consists of gluing the six sensors onto the flex. The positioning of the chips was used to be done manually, but a programmable robot which has a maximum mismatch alignment reaching approximately 20 μm is in charge of this procedure. As the sensors are thin and fragile pieces, the manipulation is done thanks to a vacuum sucker. Few drops of glue are dispensed on the flex and then, the sensors are gently pressed one by one on top of it to be glued. Afterward, the glue is cured in an oven and the chips can't be removed anymore. If a sensor is not working properly, it can't be replaced by a new one because the force needed to un-glue it might break the fragile flex-cable. On the worse case scenario, a new sensor can be glued on top of it, but this solution can't be envisaged for a real ladder as it increases the material budget locally. In order to avoid this situation, the sensors are probe-tested at the IK in Frankfort, to select only the good ones before the module assembly. The final step consists of soldering the 540 wire-bonds (a single MIMOSA-26 requires 90 wire-bonds) thanks to a semi-automatic machine. The wire-bonds can be protected by applying a glob-top epoxy. It has the advantage to offer a protection against moisture or contaminants, an electrically insulation and prohibits their movement during other manipulations (see 5.1.2 for the utility of the glob-top epoxy). Nevertheless, it increases the material budget locally and if an electrical problem occurs, the wire-bonds can't be disconnected. When the module is assembled, it is finally transferred onto a plastic sole, which has alignment pins. This sole helps to manipulate the modules, but

Citation to a glob-top paper

also reduces the stress on the flex-cable, by holding it as flat as possible. During shipping, a plastic cover is screwed on top of the sole to protect completely the module.

Ladder assembly

The ladder assembly is performed by the Bristol team. It consists of group two modules together on a spacer (SiC) and a bate (an aluminum plate). The operation is done entirely by hands. Each module is placed on a separate jig containing grooves and alignment pins to ensure the positioning. The sensitive side of the module is facing the jig to have an access to the rear of the flex-cable for the gluing procedure. Then, the foam is placed on one module below the sensors, while the bate is glued below the connector with an overlap on the foam. The second module receives some glue on the backside before the jigs are assembled together. The glue is then cured for one day. The amount of glue needed for the assembly was studied carefully. Indeed, the surface of the foam is irregular, so if not enough glue is used, the foam will not be glued on the module. On the other hand, using too much glue might stick the jigs together. When the ladder is finally ready, it is placed into an aluminum box used for shipping but also testing.

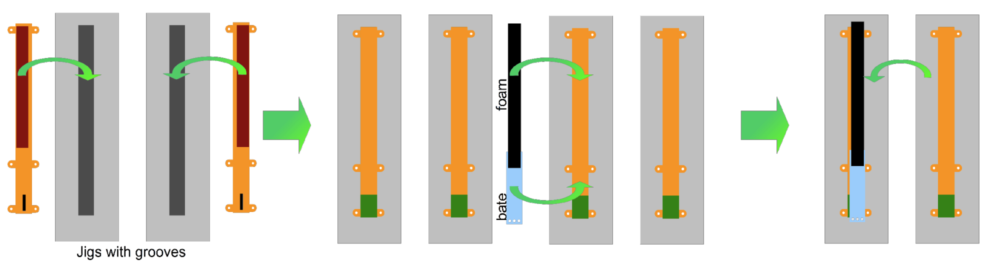

(a) (b)

Figure 5.1 – Drawing of the ladder assembly. The modules are first placed on the jigs, sensors facing the grooves 5.1a, then the foam and the bate are glued between the two modules 5.1b.

5.1.2 Visual inspections

As explain in subsection 5.1.1, the sensors positioning was performed firstly manually and later was switched to an automatic procedure. To tune properly the robot which is in charge of gluing the sensors on the flex-cable, the

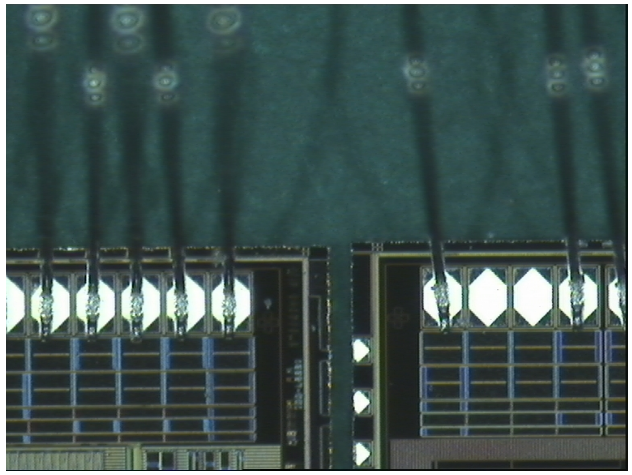

Figure 5.2 – Visualisation of the alignment. The distance between the two edges is approximately 51μm.

microelectronic group needs a position feedback. The modules are then inspected under a microscope to measure the gap between two sensors, and their position relatively to each other. The distance between the last pixel of a sensor to the neighboring one should be less than 500μm, taking into account the 20μm robot's mismatch. The figure 5.2 is a picture taken with a microscope showing the relative position of two sensors on the bottom of the matrix for an aluminum straight module. The gap between the two edges is approximately 51μm.

The visual inspection is also needed to check if the wire-bonds are correctly connected to the right sensor's pad, to verify that the gluing of the sensors on the flex-cable did not break the matrix due to some dust and also to control that the shipping of the module between the labs (for example between Strasbourg and DESY) did not damage it. The modules are fragile objects that have to be manipulated with care. Any wrong manipulation can damage severely the vital functionality. For example, the figure 5.3 shows a picture taken with a microscope of wire-bonds crashed due to a falling cable on it. The sensitive part and the electronics were not damaged, but some wires were touching leading to a shortcut. Fortunately, the microelectronic group at Strasbourg was able to unbend the wires and repair the most damaged one. This module is fully operational and working correctly. By using the glob-top method, the wire-bonds can survive to falling cable, but if they are not assigned to the right pad, there is no possibility to correct it anymore.

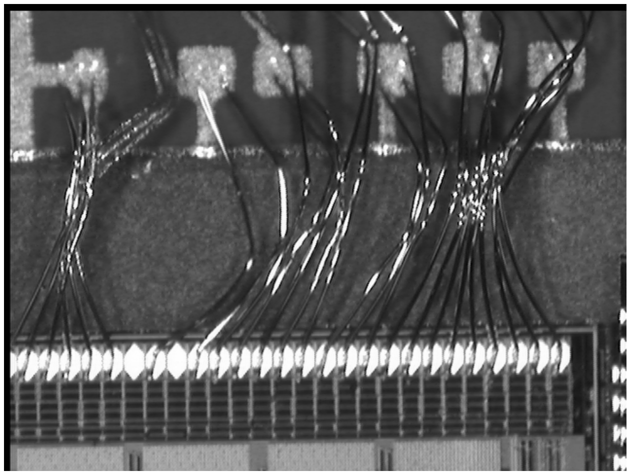

Figure 5.3 – Picture taken with a microscope showing wire-bonds crashed due to a falling cable. Some of the wire-bonds are in contact leading to a shortcut and a non-functional module.

5.2 Electrical validation

The electrical validation of a PLUME module or ladder is performed in two steps. The first one consists of checking that all the system controlling and powering the module is working. Then, the module is connected and its consumption, as well as the communication, are checked.

5.2.1 Auxiliary board

A module or a PLUME ladder is connected to the outside world thanks to a jumper cable plugged on a ZIF connector at one edge of the module. This jumper cable is linked to an auxiliary board which is in charge to power the sensors of the module, but also to pilot them and to transfer the data to the data acquisition system. This auxiliary card is connected to a power supply board which is in charge to provide the nominal voltages needed by the sensors. The power supply board delivers the digital and analog voltages (V_{DD_D} and V_{DD_A} are set to 3.3 V thanks to two independent potentiometers), the buffers voltage V_{CC} fixed to 3.3 V, as well for the temperature measurement diodes, a ± 5 V for trigger and a power pulsing signal. For the lab tests to validate the module, the power pulsing is deactivated by connecting this pin to the $+5$ V pin of the trigger. The clamping voltage V_{clp} used for the polarisation of the pixel has to be in the range $[2, 2.2]$ V. On the first version of the auxiliary board, it was provided by an external power supply, but the new version delivers the 2.1 V needed, thanks to an I2C chips or a potentiometer (the user can select which methods to use thanks to a jumper). The auxiliary board is also connected to a computer in charge of the sensors' slow control. Two RJ45 are providing the JTAG registers, as well as the start and reset signal. For a complete ladder, the two modules have to be synchronised and the clock can be injected by a clock distribution board. One RJ45 connector is dedicated to the JTAG slow control and the signals delivered are:

- **Test Data In (TDI)**: received the serial data input feed to the test data registers or instruction register
- **Test Mode Select (TMS)**: controls operation of test logic (for example, by selecting the register)
- **Test Clock (TCK)**: uses to load test mode data from TMS pin and test data on TDI pin at the rising edge, while at the falling edge, it is used to output the test data on the TDO pin.
- **Test Data Out (TDO)**: the output data feed the input data of the next sensor and the last sensor sends the information back to the computer

The second RJ45 connector is providing signal coming from the DAQ:

- **Clock**: has a rate of 80 MHz and is provided by the clock distribution board to synchronise two modules together
- **Start**: signal provided by the DAQ software to start and synchronise multiple sensors (the JTAG start works only for one sensor).
- **Reset**: reset the registers to default value.

The principle of the connection between the auxiliary board and the different components to operate one module is depicted on the figure 5.4.

Before to connect a PLUME module to the auxiliary board, the voltages have to be set and the JTAG communication has to be checked on the auxiliary card. Two external power supplies are delivering 8 V D.C. to the power supply board and are giving an information on the consumption of the whole system. The empty auxiliary board has a current consumption about 350 mA. Then, the V_{CC}, V_{DD_d} and V_{DD_a} should be at 3.3 V, but only the two last voltages can be adjusted thanks to two potentiometers on the power supply board. The V$_{clp}$ is set to 2.1 V and should not be outside the range $[2, 2.2]$ V. The JTAG communication is verified thanks to a probe linked to an oscilloscope. The observed signals should be:

TDI:

TDO:

TMS: by default is fixed to 1 when it is not used

TCK: this clock is slower (30 kHz) than the 80 MHz needed by the sensors and is only dedicated for the slow control

Reset: by default is fixed to 1 and should change to 0 every time the reset is called by the JTAG software

Start:

Clock: Independently of the method used, the 80 MHz clock has to be correctly distributed along the auxiliary card

5.2.2 Smoke test

After the validation of the auxiliary board (and the power supplies switched off), the module can be linked to it via a jumper cable. The voltages applied to the device have to be adjusted again due to the dissipation inside the flex-cable and the jumper cable. The V_{DD_D}, V_{DD_A} and V_{clp} can be measured on different pads of the ladder: three pads are closed to the connector, while the three others are at the edge of the flex-cable, as seen on the figure 5.5

Two versions of the jumper cable were produced, one very flexible with a high resistivity and the second one stiff with a low resistivity. The most flexible cable was not used because of an important voltage drop between the auxiliary board and the module, but also because of a wrong fabrication. Indeed, after setting the voltages to the nominal value and plug in the module, a short-circuit happened. The auxiliary board tests were correct and were proofed one more time without the module. Then, a thermal camera was used to find if a sensor was responsible for the short-circuit. One sensor was hotter than the others, nevertheless, the wire-bonds were correctly assigned. The problem was coming from a short-circuit between the V_{DD_D} and the V_{clp}. By passing this two lines on the jumper cable and by connecting them directly to the module, the short was gone. Instead of this flexible jumper

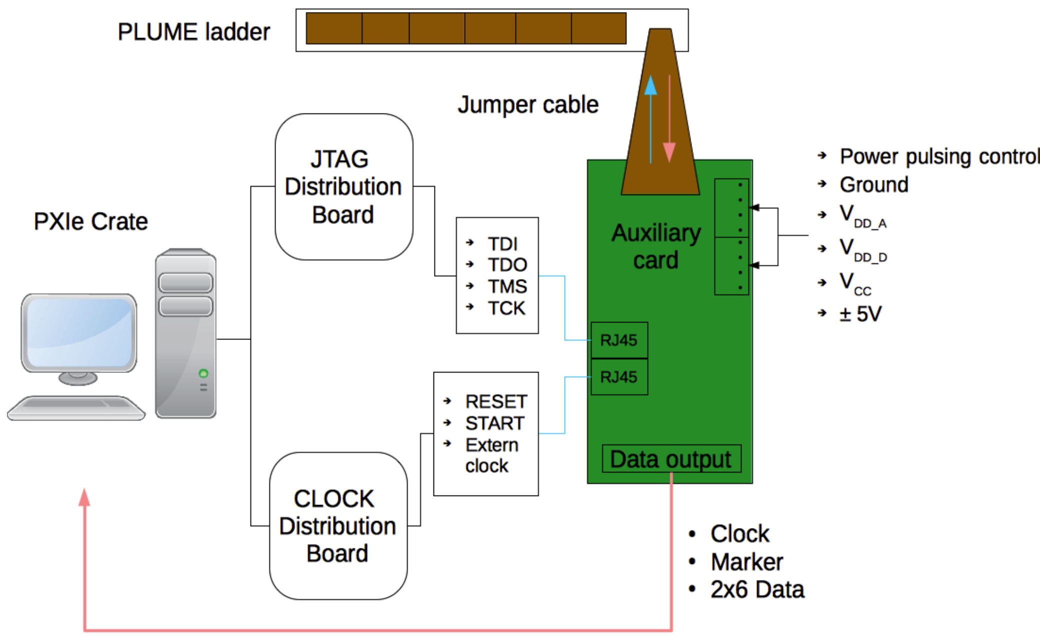

Figure 5.4 – Sketch of the PLUME connection.

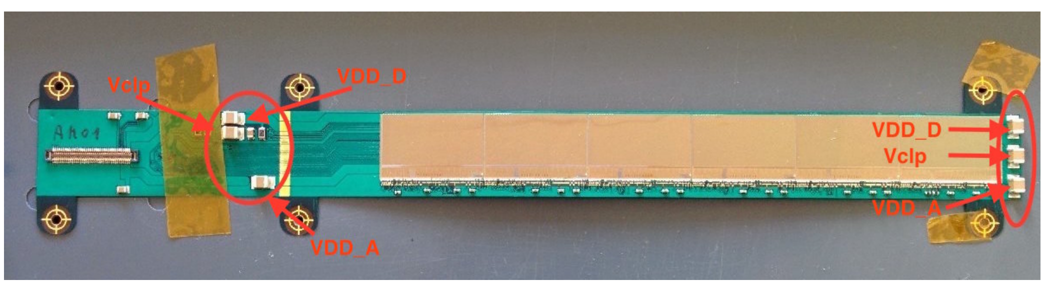

Figure 5.5 – Picture of a aluminum mirrored module with the points of measurement for V_{DD_D}, V_{DD_A} and V_{clp}.

cable, a stiffer one was used. Nonetheless, any movement of the auxiliary board causes a too important stress on the connector and on the flex-cable. To avoid any damage, a support was built to hold the auxiliary board and the module on the same frame, thus reducing the risk to break anything.

The module consumption is checked at every JTAG steps to make sure that no short-circuit occurs. Right after powering-on the system, the six sensors are starting in a random state and the consumption at this stage can not point out any electrical problem. After the reset of the registers, the total consumption should be around 33 mA. Then, the registers are loaded and the consumption should be around 750 mA. They are read-back by the JTAG software, which indicates if errors occur. If during the reading step no error was discovered, the sensors can be operated and their consumption should be around 1300 mA.

An inspection of the output with an oscilloscope is performed to check the slow control and to estimate the response of the sensor. For the normal mode data format with SUZE enable, the output data of the last frame is sparsified and transmitted during the acquisition of the current one. The information provided by the MIMOSA-26 is contained in four output lines. The first output line corresponds to the *clock* which is always running even if the data transmission is finished. Its rate depends on the clock rate register. For the normal output mode, it is 80 MHz. The second output line is the *marker*, which is available in all mode. It is set during four clock's rising edge cycle and might be used to detect the beginning of the data transmission. Then, the two last output lines are dedicated to the data. They contain multiple information. First of all, the beginning and the ending of the data transmission is determined by the *header* and *trailer*. They can be used to detect a loss of synchronisation. They corresponds to 2×16 bits (*header0-header1* and *trailer0-trailer1*) and are totally configurable through the JTAG software. The *header* is followed by the *frame counter* which corresponds to the number of frames since the chip was reset. The information is separated into two words (*FrameCounter0* corresponding to the least significant bit and *FrameCounter1* corresponding to the most significant bit). Then, the *data length* gives the number of 16 bits words of the useful data. The useful data is split into *states/line*, which contains the address of the line which has a hit and an overflow flag if the number of states is bigger than the memory limitation. It is followed by the *state* giving the number of consecutive hits and the address of the first column. Finally, the *trailer* is ending the data transmission followed by 32 bits of zero. The figure 5.6 is a picture of an oscilloscope output of a MIMOSA-26 data output. From the top to the bottom, it shows the 80 MHz *clock*, the four clock's cycle *marker*, the *data0* and *data1* with the *header* and the *frame counter*. More information about the MIMOSA-26 can be found in the MIMOSA-26 user manual[26].

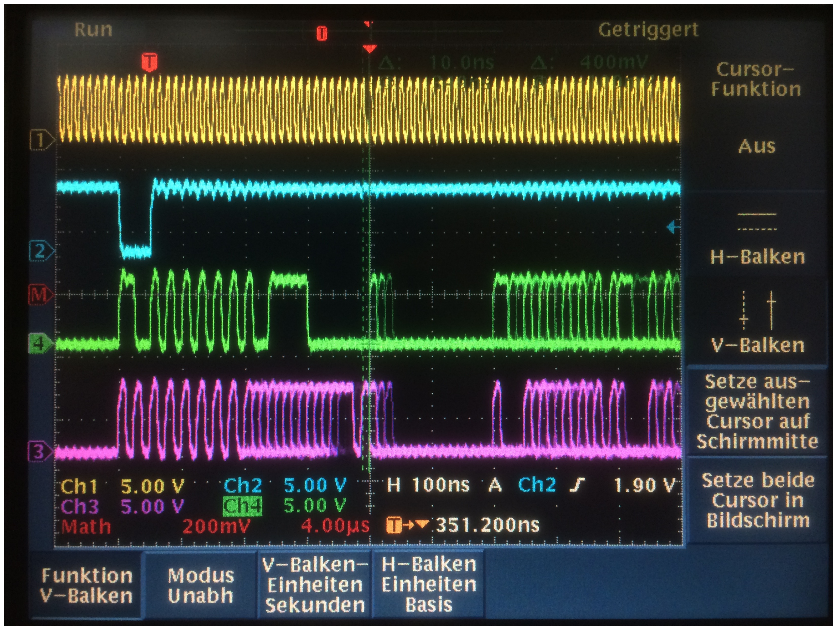

Figure 5.6 – MIMOSA-26 output from oscilloscope. The top yellow line corresponds to the clock, the blue line below to the marker (which last 4 clock cycles), and the green and purple line are the data output containing the hit information

5.2.3 JTAG communication

After adjusting the voltages and looking for any short-circuits, the next step is to control the JTAG communication for every sensor. As in the PLUME module, all the sensors are synchronised, only the *clock* and *marker* from one sensor is read back. On the oscilloscope, the trigger is set on the *marker*. The sensors are configured in the normal mode data format (80 MHz with zero suppression output) and the output is checked in three steps. First of all, the sensor is reset, the registers are loaded and read back and then the start signal is sent. Through the JTAG software, the *header* and *trailer* are modified several times and are checked thanks to the oscilloscope. Then, the discriminators' response is visualised, specifically to find pixels always sending data even if the discriminators are closed. The number of defective pixels and their position is then estimated. After that, an estimation of the threshold discriminator values to get few hits are determined and the response is then checked. Nevertheless, using light to estimate the response of the sensor can impact the pixels' baseline and modify the normal behavior of the matrix. For example, instead of sending more information, the pixels are less responsive. Thus, using a radiation source is a better solution.

5.3 Noise measurements

In the chapter 4, the principle of the CMOS sensors was described and the noise of this technology was discussed. As a reminder, the two noise contributions are the Temporal Noise (TN) and the Fixed Pattern Noise (FPN). The FPN is determined as an offset to subtract from the pixel response to reduce its non-uniformity response, while the TN is coming from the contribution of different noises during the reset, the integration and the readout of the pixel. These noises have to be measured in the lab in order to find the optimum configuration to detect physics signal and reduce the noise impact on the measurement.

5.3.1 Characterisation bench

The noise is estimated thanks to a bench of characterisation composed of a National Instrument PXIe crate equipped with a 6562 digital card, two power supplies, a power distribution board, an auxiliary and a JTAG card, as well as the module to test. The procedure described here is applied to a single MIMOSA-26, or a PLUME module, as well as an MIMOSA-28 sensor. Nevertheless, the data acquisition software used during the characterisation is slightly different to match the clock speed, depending on the sensor technology. The four data outputs are connected from the pins on the auxiliary board to the digital card thanks to a National Instrument spider cable. Firstly, a test pattern, which loads automatically a JTAG file for this test, is done to read the *header* and *trailer* during several frames with a determined data length. It has been observed that the *clock* output cable has to be eighty centimeters longer than the three other cables to ensure the synchronisation on the rising edge. If this is not done or if one of the cables has a wrong polarity, the software is not able to read the *header* and *trailer* and the characterisation can't be done.

Then, the sensors are configured in the discriminator output mode. The zero suppression mode is bypassed, pixels and discriminators are in normal mode (the whole matrix read in 115μs), but the readout frequency is lower (10 MHz) via 2 LVDS output pads. The control of the discriminators is divided into four sub-matrices, each containing 288 columns. Thus, for one sub-matrix a threshold value in DAC units in the JTAG software is driving all the discriminators, depending on a baseline value. For one line, usually one located in the middle of the matrix, its baseline response is studied to find the "middle-points" by looking for the threshold of each sub-matrix, in which the discriminators are reaching a half activation. When this "middle-points" are determined, the homogeneity of the matrix is checked, as shown on the figure 5.7. Due to the structure of the sensor, the homogeneity is not perfect and some dispersions in the discriminator response are observed between the beginning and the end of a sub-matrix. Moreover, to reduce this dispersion, the reference baseline, and the clamping voltage have to be adjusted.

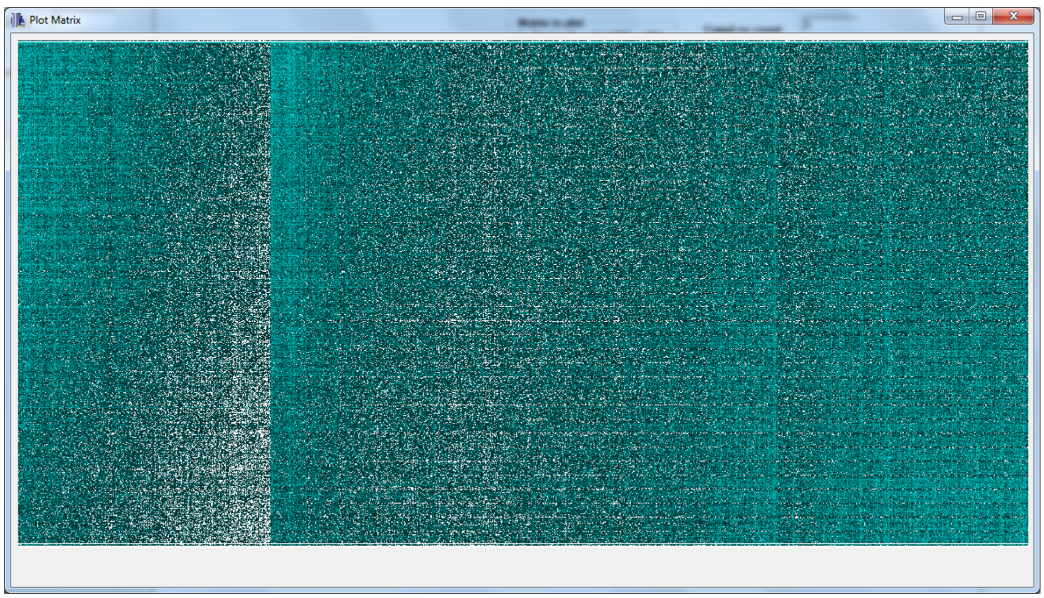

Figure 5.7 – Matrix response for the discriminators half activated.

Afterward, the thresholds are set to the lowest and highest value to look for defect pixels in the matrix. On the one hand, few pixels can be always activated even if the discriminators were closed. The figure 5.8 depicts the matrix output for all the discriminators closed. Therefore, a line is always activated, as well as few pixels in a column and they are increasing the fake hit rate of the matrix. A solution exists to disconnect some discriminators in order to reduce the noise of defect columns thanks to the JTAG program, nevertheless, no solution during the sensor programming exists to remove the defect lines. On the other hand, few pixels can be always deactivated even if the discriminators are completely opened, thus, they are not able to detect any physics signal. This behavior is represented on the figure 5.9 and no solution exists to make them working properly.

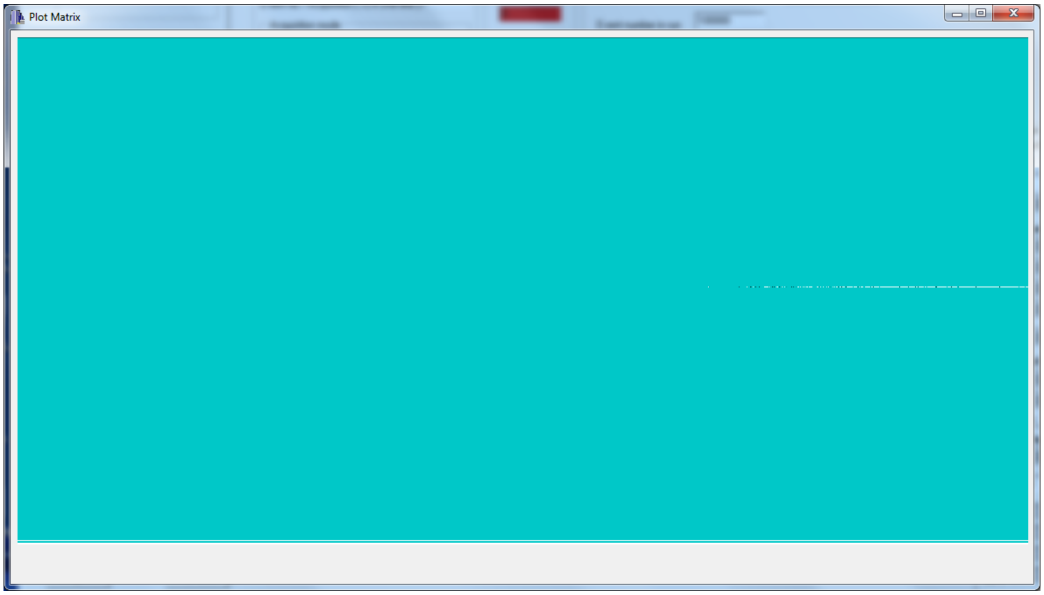

Figure 5.8 – Matrix response in discriminator mode, where all the discriminators are opened. On the right of the matrix, one line is not working correctly and some pixels are never activated

5.3.2 Threshold scan

The noise performance of the sensor is determined thanks to a threshold scan around the "middle-point" found before. This consists to record the normalise response of the discriminators or the discriminators and the pixels for different threshold values. For the first possibility, an external voltage is injected into the discriminators, while the matrix output is disconnected. Only the noise contribution coming from the discriminator is thus determined. In this work, the noise performance results presented were done without injected an external voltage, but rather with the sensitive system connected to the discriminators. Usually, 29 runs containing between 50 to 1000 are stored. The files created are used to firstly, build a configuration file containing the DAC values of each sub-matrix for the different thresholds applied. The threshold is here defined has the voltage applied to the discriminators. Afterward, this file is analysed and converted to create an output file containing a hit average picture of each sub-matrix for each step. Then, a macro based on C++ and ROOT framework is reading the hit average

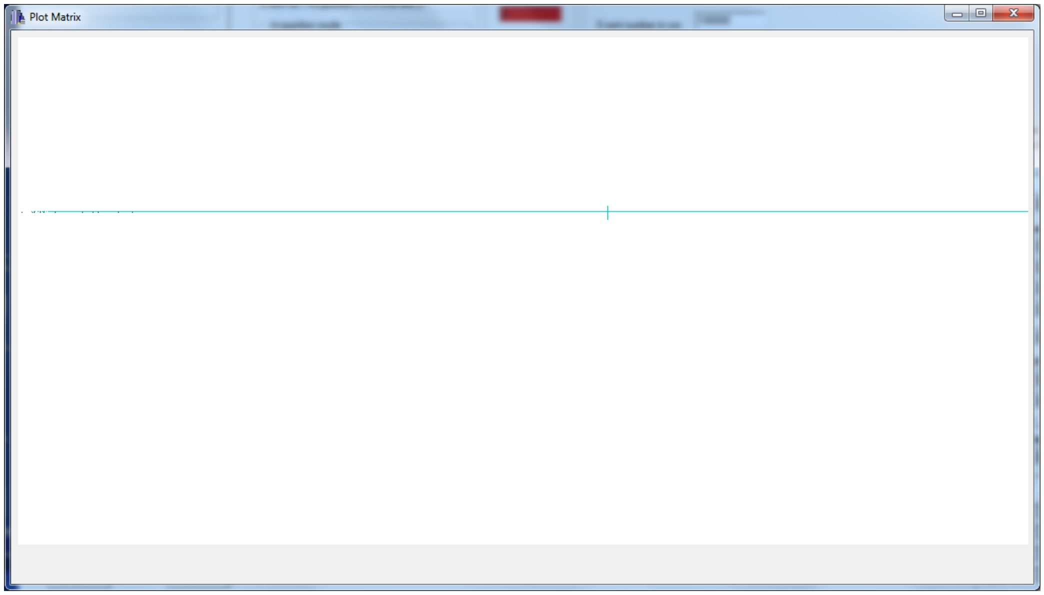

Figure 5.9 – Matrix response in discriminator mode, where all the discriminators are closed. One line of pixels is always activated, as well as few pixels in the same column. This will increase the fake hit rate of the sensor.

picture to plot the transfer function, also called "S" curve, as represented on the figure 5.10. It shows the normalised response of the 288 discriminators and the pixels contained in this sub-matrix as a function of the threshold applied in millivolts. The temporal noise of each pixel is calculated from the derivative of the "S" curve and is represented here in the left plot of the figure 5.11. The mean value of the distribution obtained the mid-point threshold of a pixel. The dispersion of the mid-point threshold corresponds to the fixed pattern noise, represented on the right plot of the figure 5.11.

The one on the left represents the temporal noise, while the right one represents the fixed pattern noise. The systematic offset of the discriminator is extracted from this measurements (the mean value of the temporal noise, the mean value and the sigma value of the fixed pattern noise). To calculate the discriminator thresholds of each sub-matrix for a given SNR, the total noise is determined as:

$$\text{Total noise} = \sqrt{< TN >^2 + < FPN >^2} \tag{5.1}$$

For a given S/N cut σ, the thresholds are determined by:

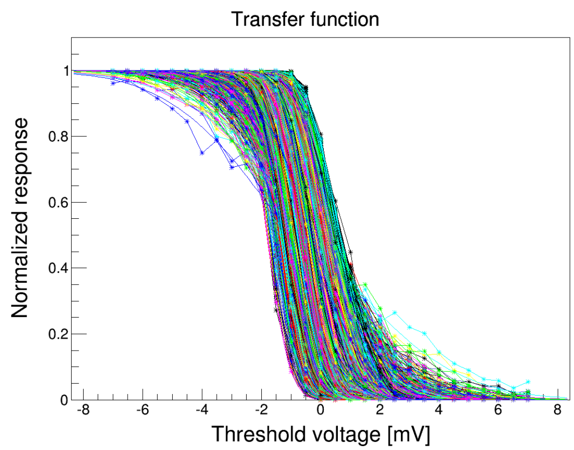

Figure 5.10 – Pixels response of a threshold scan around the middle-point of discriminators for a sub-matrix.

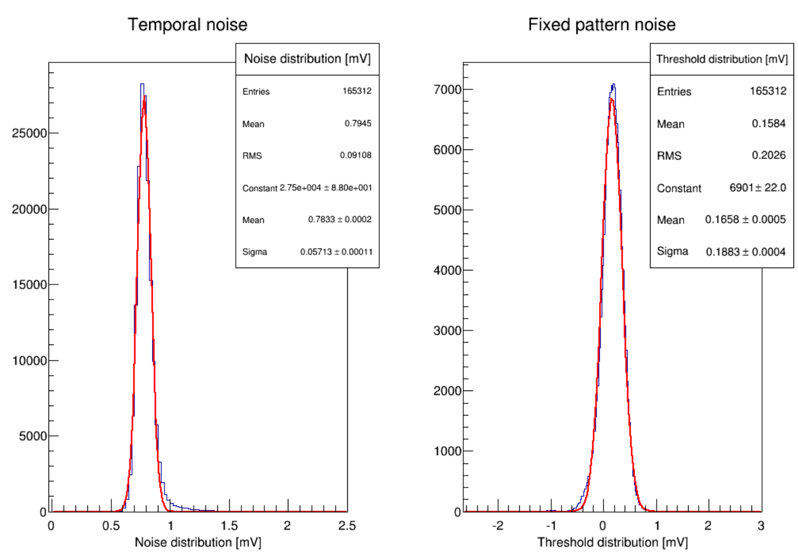

Figure 5.11 – Noise performances of a sub-matrix for the discriminators and the pixel array output. The temporal noise is plotted on the left plot, whereas the fixed pattern noise is represented on the right plot.

$$\text{Threshold (mV)} = \text{Total Noise} \times \sigma + \text{offset} \tag{5.2}$$

This is converted into the DAC values by taking into account the DAC offset and the DAC slope, which is assumed to be 0.25 mV:

$$\text{Threshold (DAC)} = \frac{\text{Threshold (mV)} - \text{DAC}_{offset}}{\text{DAC}_{slope}} \tag{5.3}$$

5.3.3 Noise measurements

Once the thresholds are defined for the different cuts, the fake hit rate of the matrix, as well as the detection homogeneity is determined. A quick step consists of using the DAQ software and acquiring ten-thousands events in the dark to determine the noise qualitatively. The fake hit rate per event per pixel is then considered as:

$$\text{F.H.R} = \frac{\text{Number of hits}}{\text{Number of events} \times \text{Number of pixels}} \tag{5.4}$$

The figure 5.12 is representing the accumulation in the dark of ten thousand events for a threshold five times bigger than the noise. The measured fake hit rate was below 10^{-4} hits/pixel/events.

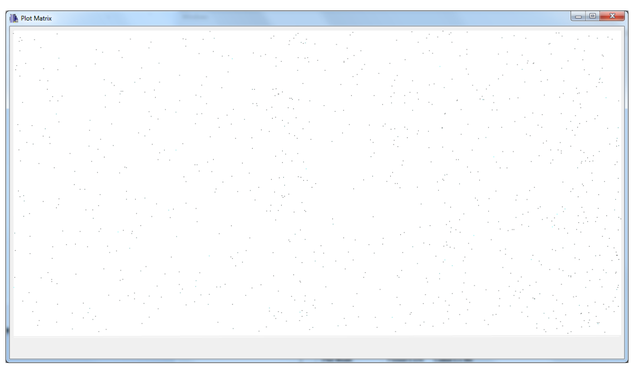

Figure 5.12 – Accumulation of 10k events at a thresholds of 5 times the noise acquired in the dark.

Then, an iron 55 source is used to control the homogeneity of the thresholds determined before. The figure 5.13 represents the accumulation of ten thousand events for a threshold five time bigger than the noise with an iron source on top of the sensor.

Finally, in order to validate the sensor, the acquisition system used during the test beam is used to calculate quantitatively the fake hit rate. The

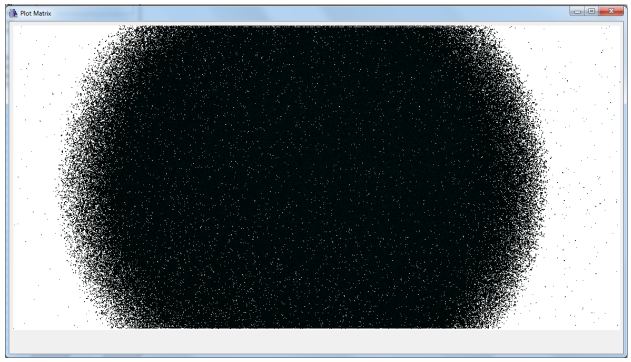

Figure 5.13 – Accumulation of 10k events at a thresholds of 5 times the noise with Fe55 radiation source.

auxiliary board is connected to a Flex RIO board instead of the digital card. The test beam DAQ software developed by the IPHC is using a LabVIEW interface for the run control. It provides several useful information, such as the number of events acquired, the *header*, the *trailer* and the *frame counter* of the sensor. This helps the user to know if the acquisition is running properly. If the *frame counter* is different for each sensor, this points out a loss of synchronisation during the acquisition. Also, a different *header* or *trailer* such as the ones set in the JTAG software might point out a wrong connection. A second software is used to store the data into three files: a parameter file containing the run number, the event number, an index file and a binary file containing the raw data. Two acquisition modes are available. The first one, used in test beam, acquires data only when a trigger is sent. The second one, stores all frames regardless the trigger status. This acquisition is the one used in the lab, as only the noise of the sensor is measured.

Several runs containing each one million events are acquired for different thresholds. The data stored are analysed with a software developed by the IPHC and is called TAPI Analysis Framework (TAF)[27]. It is based on C++ and the ROOT framework. The software reads the information of the hit pixels, reconstructs the clusters of hit pixels and in the case of a test beam is able to reconstruct tracks from the hit information.

A method is in charge to determine the fake hit rate with respect to the number of pixels hit per event. From the distribution shown on the figure 5.14, which represents the number of pixels fired per event, the average fake hit rate is calculated as the mean of this distribution divided by the total number of pixels contained in the matrix. The error on the measurement is

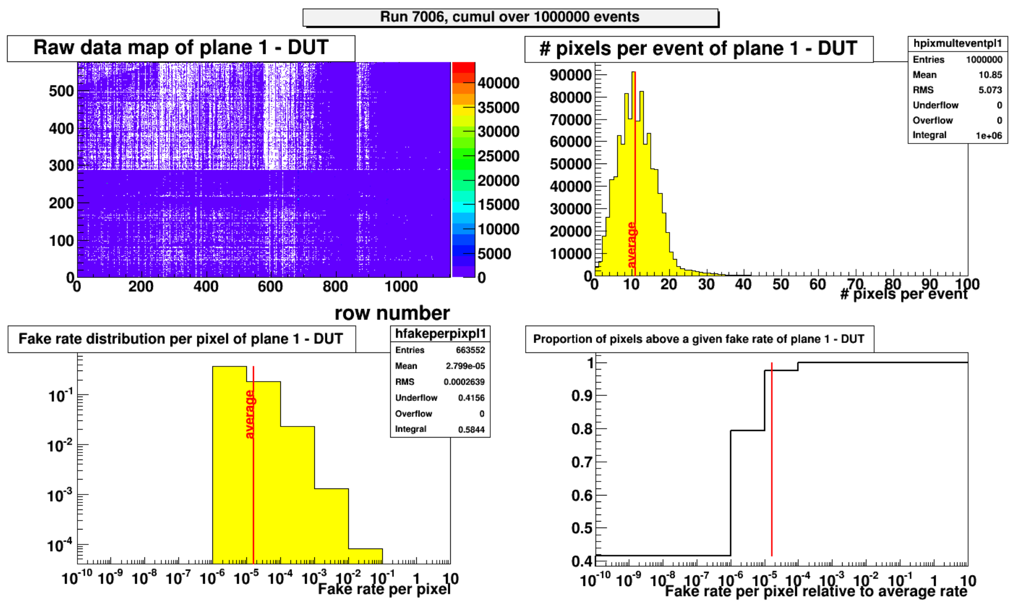

Figure 5.14 – Results of the fake hit rate measurement for a threshold three times bigger than the noise. The top left plot represents a raw picture of the million events accumulated over the whole matrix. The top right one is the distribution of the number of pixels hit per event. The bottom left plot is the fake hit rate per pixel distribution, while the bottom right one is the fake hit rate relative to the average rate distribution.

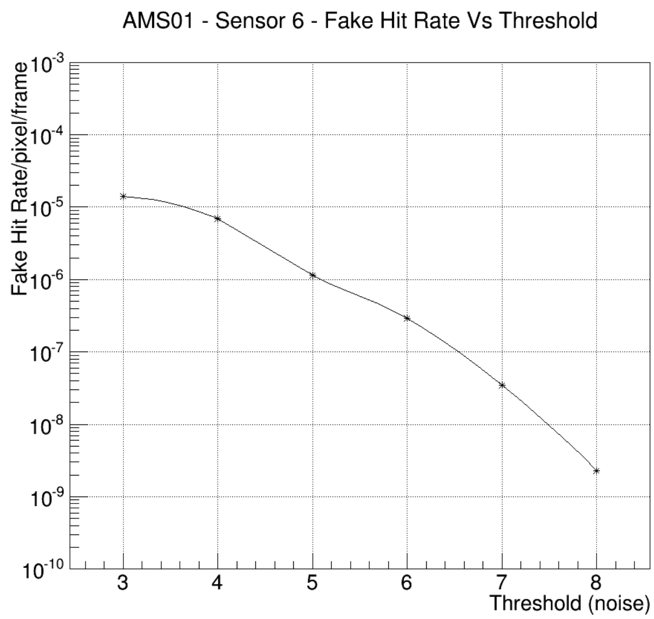

Figure 5.15 – Distribution of the fake hit rate per pixel.

then the root mean squared of the distribution divided by the number of entries and the number of pixels inside the matrix. This calculation is done for different thresholds and the figure 5.15 represents the average fake hit rate per pixel per event as a function of the threshold for one sensor of an aluminum module. The results are matching the expected behavior for a standalone MIMOSA-26 sensor as shown in figure 4.10.

5.4 Conclusions

The assembly procedures and the tests performed in the laboratory were introduced along this chapter. Only the results for one sensor were presented. Nonetheless, all the modules have a same behavior as the one expected for one single MIMOSA-26. So far, for the new PLUME versions which have a narrower flex-cable and which should embed only 0.35 % of the radiation length, different prototypes were built. The first ladder using copper module was assembled in January 2016. New ladders are currently being built and the collaboration is expecting to test them in the DESY test beam facility in November. Nevertheless, the aluminum ladder seems to be more challenging to build. Indeed, the three first mirrored versions produced have a connector problem, that could have been damaged by plugging and unplugging the jumper cable. This problem did not occur with the copper mirrored versions and this might come from a more fragile flex-cable. Ideally, each module should have is own jumper cable and this should not be disconnected. Nevertheless, for shipping them, there is no other solution. The collaboration is thinking of a tool which will reduce the stress applied to the connector.

The next chapter deals with the tests performed in real condition at the CERN-SPS facility with the PLUME-V1 prototype in 2011.

Chapter 6

Deformation studies of a ladder under the test beam

The first full-scale prototype which embeds twelve sensors glued on a copper flex-cable and a 8 % density SiC foam was tested in November 2011 at CERN-SPS facility with a pions beam of 120 GeV. The motivations to perform such a test in real conditions are first, to make sure that the ladder is working properly. Secondly, to verify the response homogeneity of each sensor. Finally, it has to prove the benefits of a double sided measurement. This chapter does not aim to present fully the test beam campaign and all the results but to focus on a specific study of the ladder's deformation observed during the alignment procedure. More results about this test beam are presented in Loic Cousin's thesis[33]. This chapter will present the test beam facility, as well as the experimental set-up. The alignment procedure is explained and some results for the ladder positioned in a normal incidence, as well as the ladder tilted in one direction, are discussed. The second part of the chapter will focus on the deviation observed during the alignment and will discuss a method to overcome these deformations. Finally, the benefits of double-sided measurements will be introduced.

Contents

6.1 Test beam of the full complete PLUME ladder at CERN

6.1.1 Test beam facility and beam test set-up

The test beam was performed at CERN-SPS in the North hall on the H6 beam line. Negative pions with an energy of 120 GeV were used. The spill structure was 9.6 s with a dead time of 45.6 s. The bench set-up is composed of a telescope equipped with four standard MIMOSA-26 sensors, thinned down to 120 μm and used as reference planes. It is made of two arms and the distance between two sensors of the same arm is 5 mm. The reference planes are stabilised to a temperature of 15 degrees Celsius and a 8 sigma S/N threshold cut was applied. The PLUME ladder is positioned between the two telescope arms for the tests. For the rest of the chapter, the ladder is called the Device Under Test (DUT). The bench has also 7×7 scintillators used for triggering the data. Most of the runs were taken with a trigger frequency between 2 and 8 kHz, except for two days where the frequency was oscillating between 1 and 1.3 kHz. The acquisition system is limited to eight inputs and four of them are used by the telescope. Thus, only four sensors of the DUT were connected to the acquisition, two on each side. The temperature of the DUT was stabilised thanks to an air flow cooling system, provided by a fan.

6.1.2 Cartesian coordinate systems

Although the sensors have their own ID to distinguish them during the analysis, the position of each plane has to be known exactly. Two Cartesian coordinate systems are then defined. The first one is the global one and is determined by the position of each sensor of the telescope. The notation used for this coordinate system is (x, y, z). The x-axis corresponds to the horizontal direction, the y-axis is the vertical one and the z-axis is along the beam direction. The origin $(0, 0, 0)$ of the system is usually defined by the position of the first plane hit. The second coordinate system is the local one and is determined by a single sensor. To differentiate this reference system to the other one, the (u, v, w) notation is used. The u-axis corresponds to the pixel rows, the v-axis is along the pixel columns and the w-axis is perpendicular to the matrix. The origin of the local system is the center of the pixel matrix. The figure 6.1 summarises the definition of the two coordinate systems.

Draw a better figure

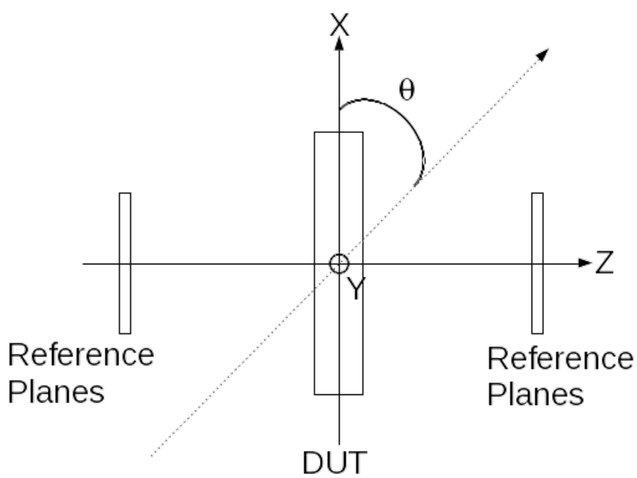

Figure 6.1 – Drawing of the laboratory coordinates.

6.1.3 Measurements

The prototype validation was done under several conditions. Firstly, three different geometric configurations were used. On the first one presented on the figure 6.2a, the DUT is parallel to the telescope planes and the beam is hitting the device in a normal incidence. The ladder is placed in between the two arms. The middle of the foam is at equal distance from both inner telescope planes. For the second configuration, as shown on the figure 6.2b, the distance between the telescope planes are the same, but the DUT is tilted between 28 and 40 degrees along the y-axis. Runs with a larger angle (60 degrees) were done. Due to the PLUME box's size, the cabling for the acquisition, the air cooling system and the design of the telescope stage, limiting the spacing between the two arms, the DUT was placed behind the two arms, as presented on the figure 6.2c. For both configurations, different parameters were modified. The thresholds were set to 5 and 6 mV, different sensors were aimed and the air flow speed was set to 3 m.s^{-1} and 6 m.s^{-1}.

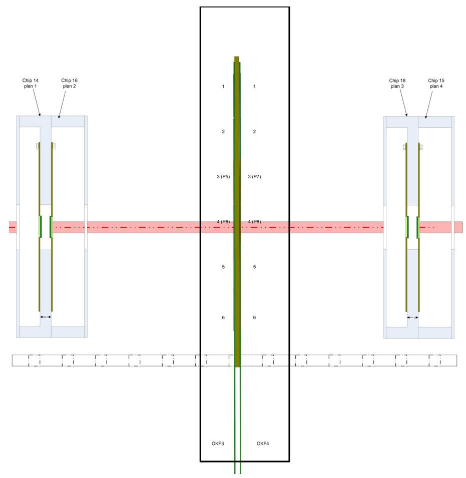

(a) Configuration for normal incidence with respect to the beam direction.

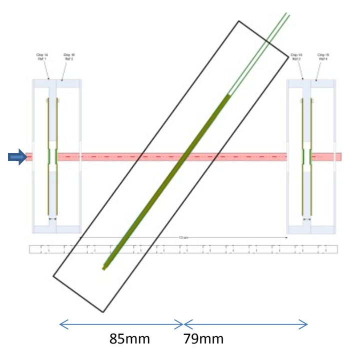

(b) Configuration for an angle between 28 and 40 degrees.

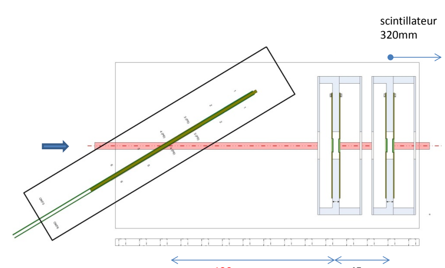

(c) Configuration for an angle of 60 degrees.

Figure 6.2 – Top view sketches of the test beam configuration for different ladder positions: 6.2a is for normal incidence, 6.2b and 6.2c are for tilted ladder.

The analysis and the results shown in the following sections were performed with TAF, the analysis software developed by the IPHC and presented in chapter 5.

6.2 Spatial resolution studies

One of the measurements performed during the analysis is to determine the pointing resolution of the ladder. As the sensors used are well-known, the performance of the ladder should be similar to the one expected. Any deviations on the pointing resolution or the efficiency might point out an unexpected impact of the mechanical structure or the flex-cable design over the whole system. The alignment steps to obtained the pointing resolution of the ladders are explained below for different run configurations.

6.2.1 Normal incidence track

For each event, the acquisition is recording the position of the pixels hit, the frame number, as well as the sensor ID. The binary file created contains no information about the relative position of each sensor. To perform an analysis, the telescope planes have to be aligned each other. The hits information of every plane is combined in order to create tracks. A track corresponds to the path of a particle through the system. Thanks to this information, the tracks are then compared to the hits position on the DUT to give some information, such as the detection efficiency (the ratio of tracks matched to the hits on the DUT) or the spatial resolution (minimum distance to distinguish two incoming tracks).

The alignment procedure is done in two steps: firstly the telescope planes are aligned to minimise the mismatch of particles' tracks and to improve the tracking resolution. Afterward, the DUT is aligned with respect to the information provided by the reference planes and then, the analysis itself is performed. Although the position of each sensor is measured during the test beam with a precision of the millimeter, for the analysis, a precision of the micron level has to be achieved. Three degrees of freedom were taken into account for the alignment here: two translations for the x and y-axes and one rotation around the z-axis. The z position is determined by the position measured during the test beam campaign and is not considered as a free parameter due to the beam used.

Alignment procedure and telescope alignment

Firstly, the data acquired during the test beam are processed to extract the signal and the hit information. For each frame, the position of the pixel(s) having a signal above the discriminator threshold is stored and assigned to an ID corresponding to a sensor. The analysis software is in charge to assign correctly the hit to the sensors and then to group the pixel fired into clusters. As the sensors used during the test beam have a binary output, no information on the seed pixel is available. Thus, the hit position is obtained from a centre-of-gravity calculation.

Secondly, with the analysis software, one plane is considered as the origin of the telescope coordinate system and is used as a reference for the alignment. Usually, the first sensor hit by the beam is the main reference. The alignment means to correct the offset for the view angles and the hit position of the telescope planes and the DUT. These offsets are found thanks to scattering plots where the residuals are represented as a function of predicted hit position. An alignment is considered as a good one when the residuals are not correlated to the predicted hit position. If it is not centered around zero, an offset has to be applied in this direction, whereas a slope indicates that a tilt has to be applied. First off, the hit positions of the first plane are extrapolated to the next planes in order to perform the alignment. These tracks extrapolated are straight lines perpendicular to the hits position. Thus, the hit position of the last telescope plane is adjusted to match the hit position of the first plane. The alignment is an iterative procedure which consists to minimise the residual. It corresponds to the distance between the extrapolated track to the closest hit on the sensor. Afterward, the track candidates are built by matching a hit on the first plane to a hit on the last one. The second and third telescope planes are aligned with respect to the information provided by the extrapolated tracks. For example, the figure 6.3a and 6.3b show the residual distributions of the second and third planes in the u and v direction with respect to the tracks built by the first and the last planes.

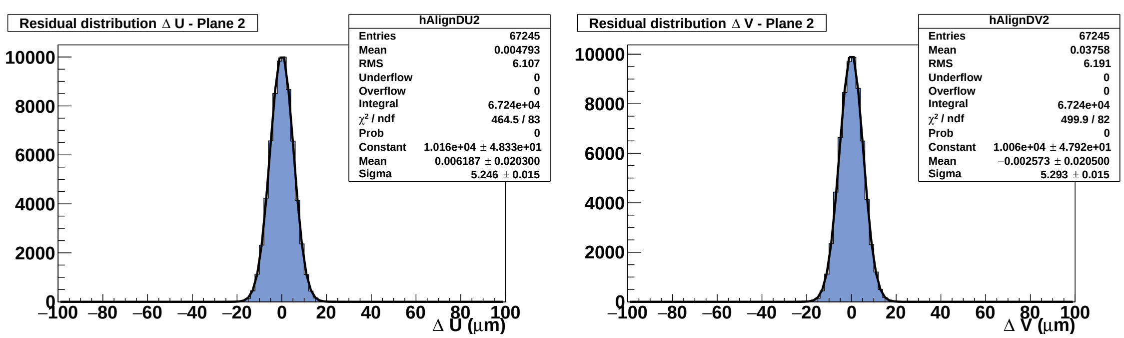

(a) Along u direction.

(b) Along v direction.

Figure 6.3 – Residual distributions in the u and v directions for the middle telescope planes.

As already explained, the alignment is an iterative procedure. At the beginning, a region of interest of 1000×1000 μm around the extrapolated is used to find a matching hit. Step by step, this region of interest is restricted to achieve a region of six times the pitch of the sensor.

After aligning the telescope, a candidate track is dismissed if it is made of less than four hits or if the χ^2 fit is greater than a fixed value determined by the user. Two assumptions are used during the alignment. The telescope planes are parallel each other. Thus the alignment consists of a translation along x and y and a rotation around the z-axis. As the test beam was performed without a magnetic field and pions of 120 GeV were used, the Coulomb multiple scattering is neglected. So, the tracks are perpendicular to the detectors and the alignment is not sensitive to the z position. A precision of the millimeter level for the position does not have a huge impact on the alignment.

Alignment of the DUT

When the telescope alignment is done, the reference tracks reconstructed by the reference planes are used to align the DUT. Its z position is fixed, nonetheless, two degrees of freedom are added to the three degrees defined above: the rotations along the x and y-axes. To assist the user in the alignment steps, several scatter plots are produced (see figure 6.4). For examples, the figures 6.4a and 6.4b help to indicate a tilt in the z-direction, whereas figures 6.4c and 6.4d help to find shift and/or tilt in the respective u and v-directions. The figures 6.4e and 6.4f show the residuals distribution in both direction for one sensor of the DUT. The width of these distributions, called spatial residual σ_{Res}, is approximately 4.1 μm and is a combination of the telescope resolution σ_{tel}, the multiple scattering $\sigma_{M.S}$ and the pointing resolution or spatial resolution of the sensor σ_{DUT}, as described in equation 6.1.

$$\sigma_{Res}^2 = \sigma_{tel}^2 + \sigma_{DUT}^2 + \sigma_{M.S}^2 \tag{6.1}$$

With 120 GeV pions, the effects of the Coulomb multiple scattering are neglected, thus the pointing resolution of the sensor is:

$$\sigma_{DUT} = \sqrt{\sigma_{Res}^2 - \sigma_{tel}^2} \tag{6.2}$$

For the configuration of the telescope used, the spatial resolution of the whole system measured is $\sigma_{tel} \simeq 1.8$ μm, thus the sensor studied here has a pointing resolution $\sigma_{DUT} \simeq 3.7$ μm for a threshold of 6 mV. This result is corroborating the pointing resolution of a single MIMOSA-26, as shown on figure 4.10 in chapter 4.

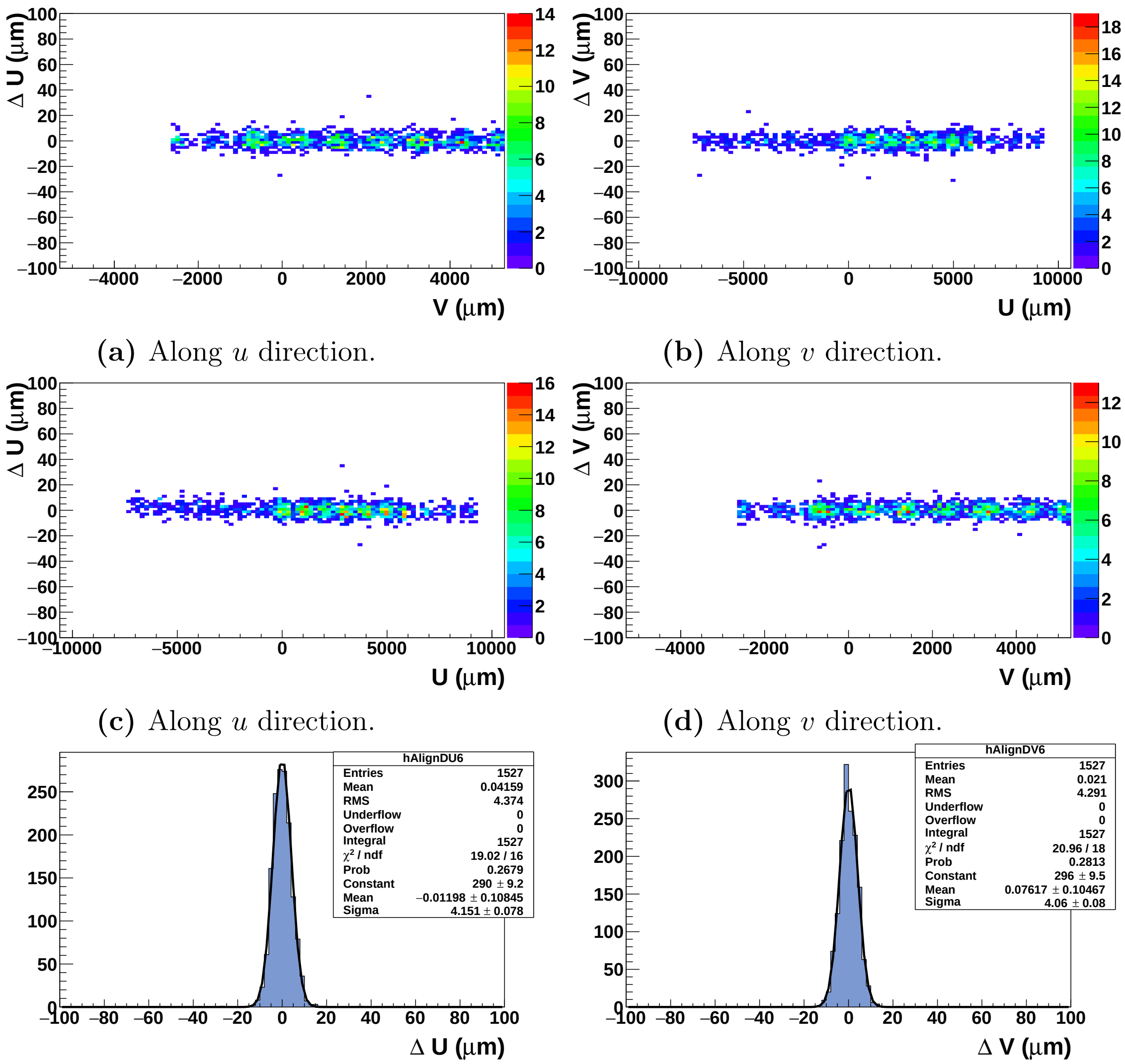

(a) Along u direction.

(b) Along v direction.

(c) Along u direction.

(d) Along v direction.

(e) Along u direction.

(f) Along v direction.

Figure 6.4 – Results of the DUT alignment: 6.4a is the residual ΔU as a function of the hit position on the v-direction, 6.4b is the residual ΔV as a function of the hit position on the u-direction, 6.4c is the residual ΔU as a function of the hit position on the same direction, 6.4d is the same plot for the other direction, 6.4e and 6.4f are the residuals distributions in the two directions.

6.2.2 Ladder tilted in one direction

The performances of the DUT are also studied for tilted tracks by rotating the ladder with respect to the beam axis along the v-direction. Three different angles were tested (28°, 36° and 60°), as well as different threshold cuts and air flow speed. The results presented below are for a run with a 36° tilt, a threshold sets to 5 mV and an air flow speed of 3 m.s^{-1}. The same alignment procedure as presented in the subsection above is used, nevertheless, the alignment of the plane along the u-direction is more complicated than the other direction. Indeed, the scatter plot in the v-direction for the front plane which is shown on figure 6.5d represents a good alignment and the spatial residual (see figure 6.5f) is comparable to the one find for normal incidence tracks. But, the scatter plot $\Delta u = f(u_{hit})$ as presented on figure 6.5c shows a banana shape that can not be flatten with a traditional alignment procedure. Moreover, the spatial residual measured on figure 6.5e is larger (6.8 μm instead of $\sim$ 4 μm in the v-direction) and the distribution has a large tail on the positive values. Concerning the back plane, the deformation is also visible on figure 6.6c but have a different form. The spatial residual measured for this plane is more than two times larger than the other side (14.1 μm) as it is depicted on figure 6.6e.

Origin of the deviations

The deviations observed are mainly caused by the characteristics of the ladder. Indeed, ultra-thin sensors with a thickness of approximately 50 μm are used. Naturally, without any mechanical structure, the sensors tend to be very flexible and not self-supporting. Nevertheless, the gluing procedure to the flex-cable and the SiC foam induces permanent deformations of the surface that can not be flattened. Also, the foam has an open-cell structure with small bumps and the glue spots might be more or less important on some positions. The Bristol group has performed a mechanical survey on a mechanical prototype, which has non-functioning MIMOSA-20 sensors. The chips were thinned and attached to the standard flex-circuits. The measurements done with an optical survey equipment have revealed a peak-to-peak flatness of the order of the 100 μm on both sides. The figure 6.7 shows the result of this survey. The overall shape is due to the intrinsic shape of the foam.

Another parameter has to be taken into account to explain the deviation observed. During the analysis, this non-flatness structure is not taken into account. The sensors are modelled as completely flat planes and the

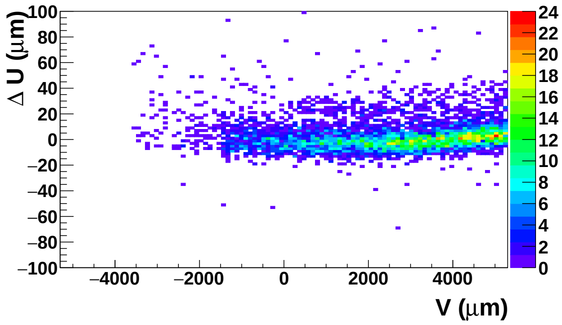

(a)

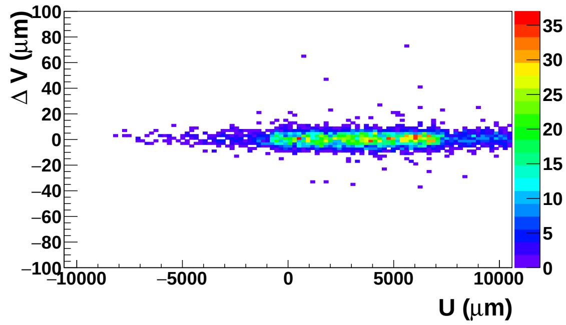

(b)

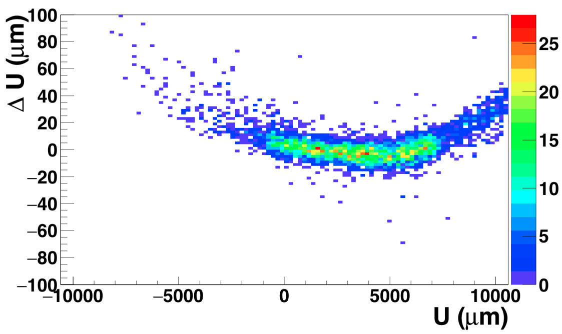

(c)

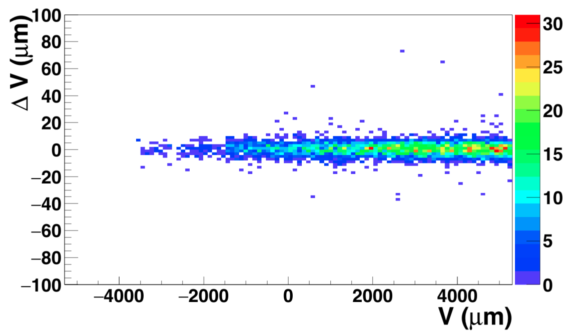

(d)

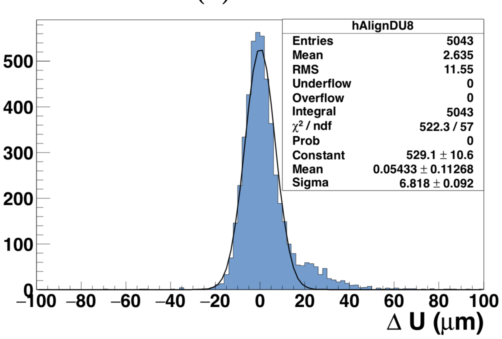

(e)

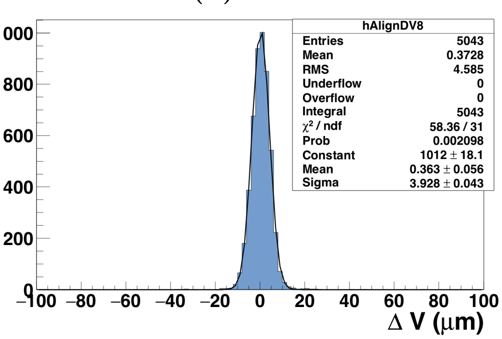

(f)

Figure 6.5 – Distribution of the residuals obtained for the front sensor with a tilt of 36°: 6.5a $\Delta u = f(v_{hit})$, 6.5b $\Delta v = f(u_{hit})$, 6.5c $\Delta u = f(u_{hit})$, 6.5d $\Delta v = f(v_{hit})$, 6.5e distribution of the residual Δu and 6.5f distribution of the residual Δv.

z-position is fixed. However, the sensor's position in three dimensions is actually different due to the deformations. When the particles are not striking the sensor in normal incidence, the hit predicted with respect to the flat

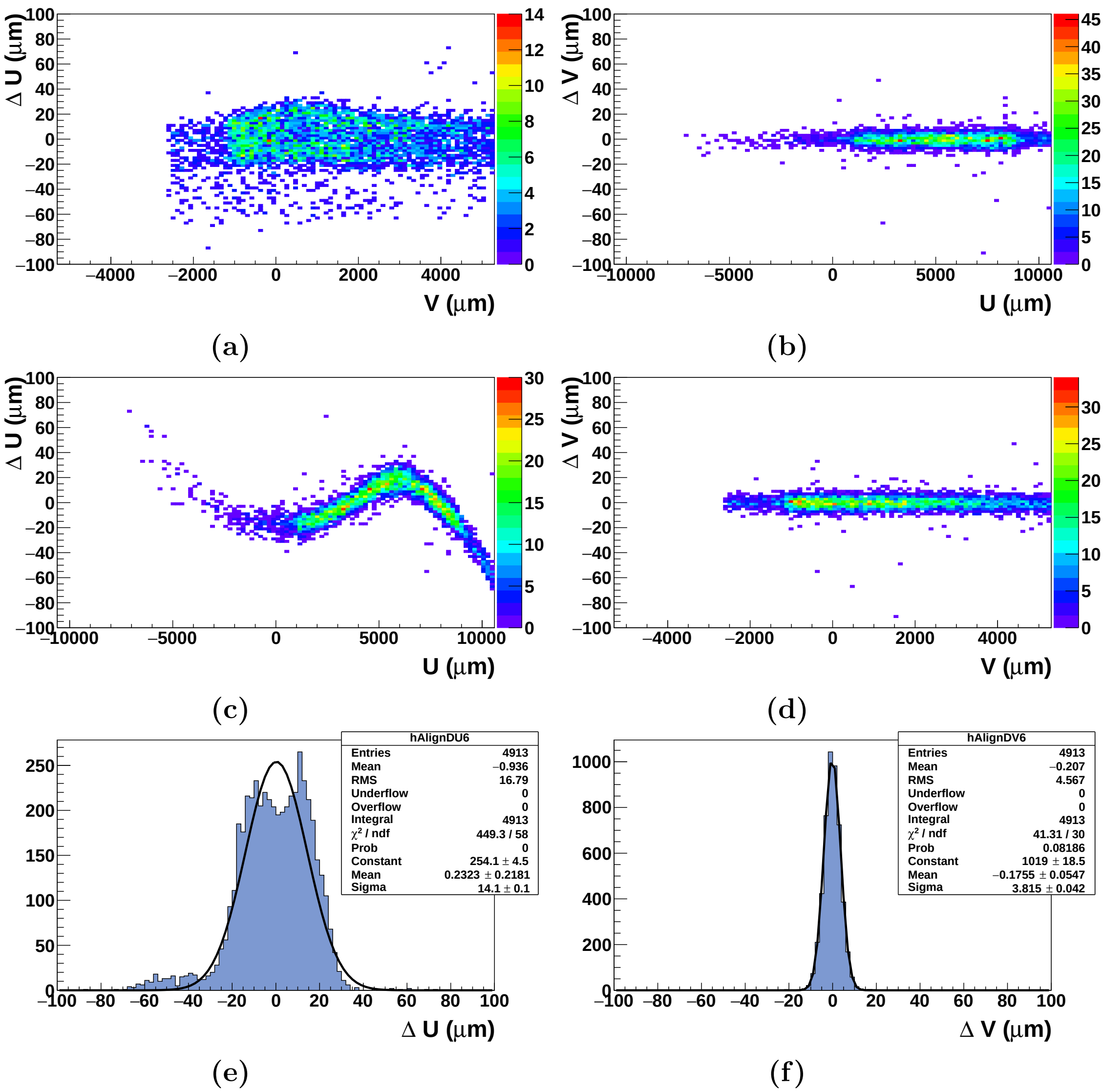

Figure 6.6 – Distribution of the residuals obtained for the back sensor with a tilt of 36°: 6.6a $\Delta u = f(v_{hit})$, 6.6b $\Delta v = f(u_{hit})$, 6.6c $\Delta u = f(u_{hit})$, 6.6d $\Delta v = f(v_{hit})$, 6.6e distribution of the residual Δu and 6.6f distribution of the residual Δv.

plane does not have the same position anymore. Thus, the residual between the position of the extrapolated track and the predicted hit is increasing. The figure 6.8 depicts the difference between the hit expected U_h on the flat

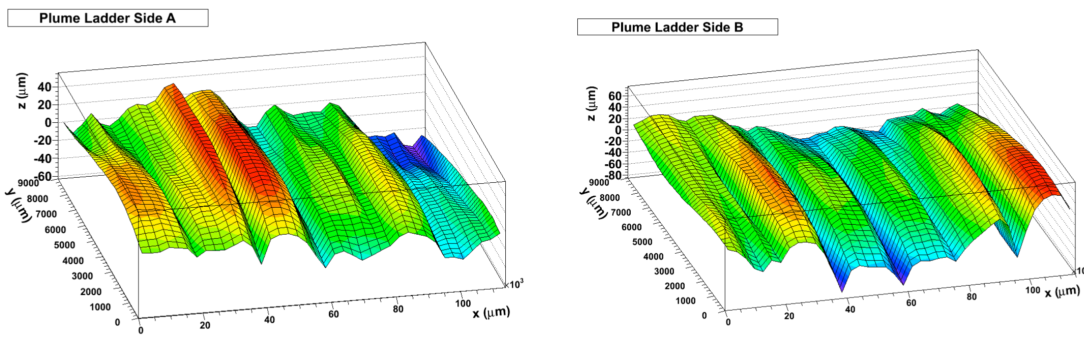

Figure 6.7 – Results of the mechanical survey of each side of the PLUME mechanical prototype.

plane and the extrapolation of the actual hit $U'_{\mathrm{h\ extrapolated}}$. For a normal incidence, these two hits are at the same position, but larger is the angle, larger is the difference between the expected hit and the extrapolated one. The deformation height δw can be expressed as a function of the angle θ and the residual δu of the track:

$$\delta w = \frac{\delta u}{\tan(\theta)} \tag{6.3}$$

Thus, the visible deformation of the surface is sensitive to the angle of the incoming track. In the case presented above, the angle of the incoming track is only in one direction and so, the deformations are visible only in the u-direction and the other one is not affected, even if the deformations are in two dimensions.

Algorithm to estimate the deformations

The sensor deformations were already studied in Strasbourg by Maria Robert Daniel. The sensor was mapped for the alignment in order to remove the contribution of the deviation on the residual[39]. As this method is done manually and is time-consuming, an automatic method has to be implemented. A similar effect was observed in the CMS tracker during the alignment procedure with cosmic rays and a method was developed to compensate the deformations[1]. They have used modified two-dimensions Legendre polynomials to parametrise the sensors' deformations and therefore, they were

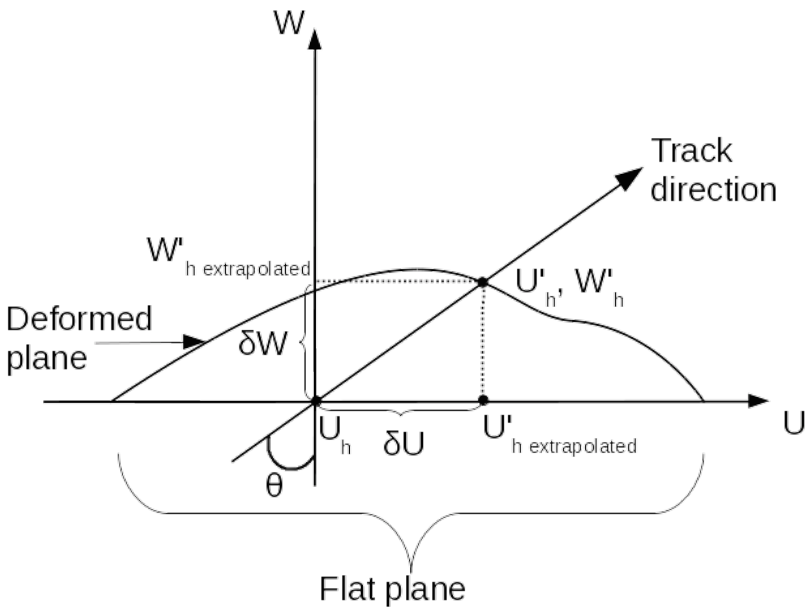

Figure 6.8 – Side view of the sensor's deformation.

able to minimise the effect of the deviations during the alignment procedure of the tracker. The method implemented in TAF was inspired by the work which was done by the CMS collaboration. Nonetheless, contrary to the CMS tracker, the tilt was produced only in one direction. Hence, the two-dimensions Legendre polynomials can not be used to parametrise the sensor's deformations, but the problem is still the same. Tracks with a large angle of incidence are more sensitive to the exact position of the plane in three dimensions, so the coordinates of the hits have to be exactly known. The deviations observed on the figure 6.5c provide an information on the behaviour of the deformation, that is extrapolated to the position of the plane on the w-direction. Thus, the hit position is calculated again with respect to the sensor's surface shape extrapolated. This shape is guessed from the track-hit residuals as a function of the hit position in the same direction. A Legendre function is used to fit the curve and the coefficient given by the fit steps are used to calculate the deformation of the plane. The equation 6.4 represents the extrapolated shape of the plane in the w-direction calculated with respect to the expected hit position u_r, which is normalised to the sensor width.

$$w\left(u_r\right) = \sum_{k=0}^{n} \omega_k P_k\left(u_r\right) \tag{6.4}$$

The ω_k are the coefficients that quantify the sensor curvature and $P_k(u_r)$ are the Legendre polynomials defined by the equation 6.5:

$$P_k\left(u_r\right) = \frac{1}{2^k!}\frac{d^k}{du_r^k}\left(\left(u_r^2 - 1\right)^k\right) \tag{6.5}$$

Then, the exact hit position is calculated by correcting the hit position extrapolated by $(-\omega(u_r).\tan\theta)$, according to the equation 6.3 and the residual Δu is determined by taking into account the tracks' angle during the analysis.

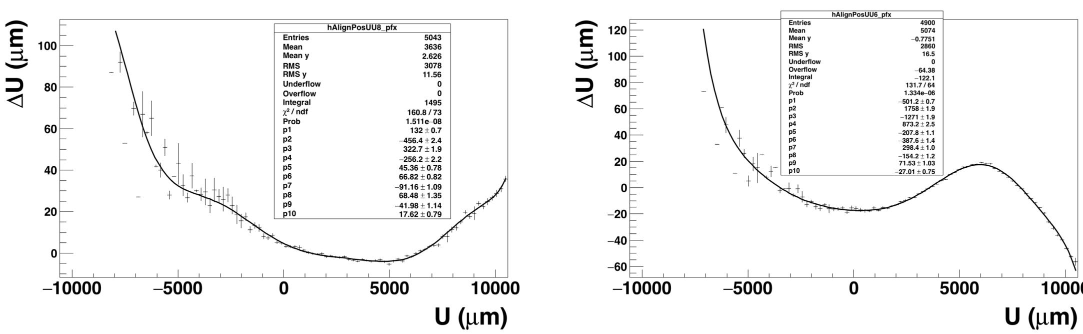

(a) (b)

Figure 6.9 – Profile of the scatter plot showing the track-hit residual in the u-direction as a function of the hit position on the plane for the same direction: 6.9a is the profile of the front plane and 6.9b is the profile of the back plane. Both profiles were fitted with a sum of Legendre polynomials up to the eleventh order.

Correction of the deformation

Contrary to the CMS case, the Legendre polynomials used here are calculated in one dimension as the tilt is only in one direction. The scatter plot displayed in subsection 6.2.2 was profiled and fitted with a Legendre function. The sum of Legendre polynomials up to different orders was tried to find the function fitting the best the profile. The coefficients obtained after fitting are used to parametrise the surface's shape and the position of the hit. The table 6.1 summarises the different χ^2/NDF obtained for the different orders, as well as the residual measured in the u-direction after correction.

A second-order Legendre function does not fit well the profile of $\Delta U = f(u_{hit})$ and does not provide a good improvement on the compensation of

	Front plane		Back plane	
Order	χ^2/NDF	σ_U^{front}	χ^2/NDF	σ_U^{back}
3	21683.9/84	6.508	35575.2/72	13.28
4	1449.91/83	6.176	25129.8/71	12.38
5	1449.79/82	5.998	1718.81/70	6.918
6	653.738/81	5.924	1480.55/69	6.817
7	304.206/80	5.922	634.696/68	6.406
8	288.376/79	5.937	269.296/67	6.228
9	225.376/78	5.9	250.565/66	6.239
10	225.353/77	5.914	152.236/65	6.159
11	158.053/76	5.913	131.727/64	6.176

Table 6.1 – Fit results of the scatter plot $\Delta U = f(U)$ for Legendre polynomials order and the residual obtained on each side of the PLUME ladder.

deformation. The best improvement was achieved on both sides from the 8^{th} order Legendre polynomials to higher values. Although the χ^2/NDF is better for higher order, the width of the residual distribution is of the same order ($\sigma_{front} \simeq 5.9$ μm and $\sigma_{back} \simeq 6.2$ μm). The figure 6.9a depicts the fit results for the front plane ans the figure 6.9b is for the back plane. For both figures, the deviation is not well fitted for the negative values. The dispersion of the residuals is wider.

For example, using a 11^{th} order Legendre polynomials has improved the spatial residual for both planes. Instead of $\sigma_u \simeq 6.8$ μm for the front plane, the spatial residual is $\sigma_u \simeq 5.9$ μm, namely an improvement of 13.2 % of the measured spatial residual and achieving a pointing resolution of 5.6 μm for a tilt at 36°. Concerning the back plane, the spatial residual measured was 14.1 μm and after the correction it achieves 6.2 μm, namely an improvement of 56.0 % on the measured spatial residual. The point resolution of the plane is then 5.9 μm As it can be seen on figure 6.10c, the deviations are reduced. Nevertheless, the edges of the plot are less corrected. This is due to the fact that the length of the sensor used to parametrise the Legendre function is a bit different to the real size of the sensor due to the deformation. On the back plane, a bump is still visible in the middle of the scatter plot (see figure 6.11c). This may be due to a missing information on the deformation of the sensor in the other direction.

This method was applied for different angles and the results are summarised in the table 6.2. The correction based on Legendre polynomials shows good results for the 28 degrees angle with a pointing resolution of 4.6 μm. Although for larger angles the precision is not expecting to reach the

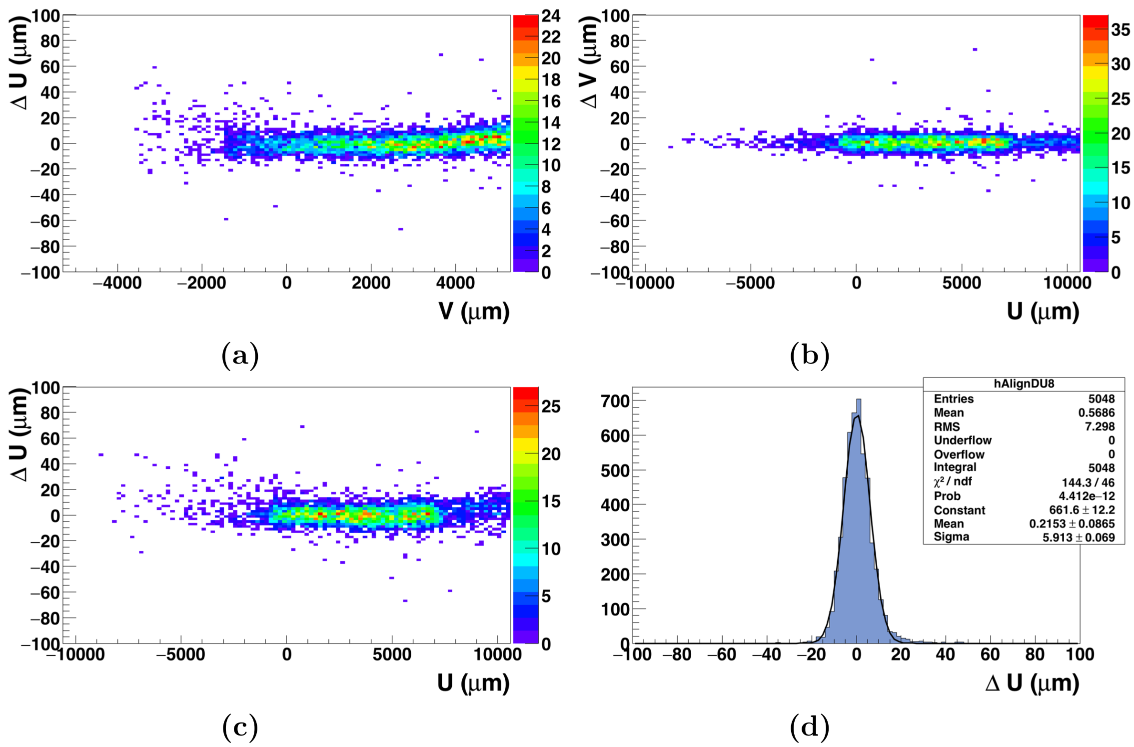

Figure 6.10 – Results of the alignment after applying the Legendre polynomials correction and tacking into account the angle of the incoming particles for the front sensor: **??** $\Delta u = f(u_{hit})$ and 6.10d distribution of the residuals.

normal value, the results obtained are less positive. For the large angle (60 degrees), the position of the DUT on the outside of the telescope arms does not provide a good telescope resolution (σ_{tel} = 18.8 μm). The pointing resolution achieved for the front and back planes are respectively 10.8 μm and 17.7 μm. The sensitivity of the reconstruction to large tracks angle, as well as a unadapted telescope configuration impact severely the spatial resolution of the sensors.

A hypothesis on the deformation of the origin might come from heating or the cooling system that induces vibration. Although few runs were performed with a different air flow speed, the impact of the cooling system and the heat was not planned for this test beam. Thus, the results are not relevant enough to conclude for any vibration or the heat that tends to deform more the surface.

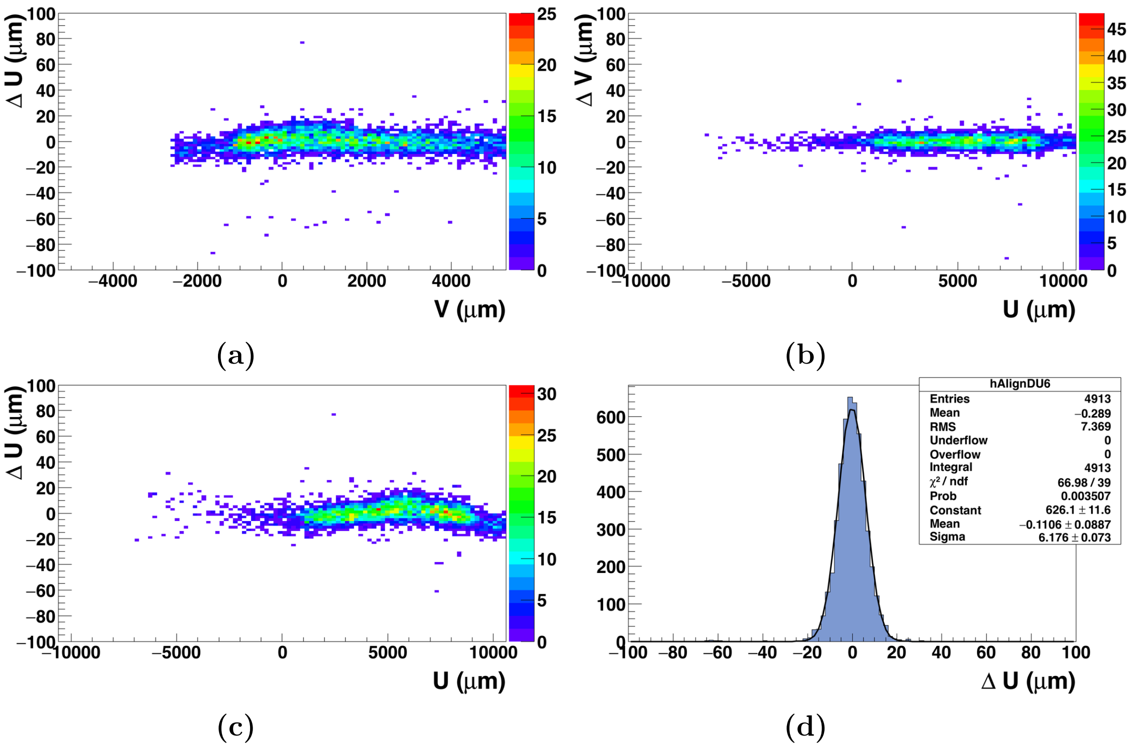

Figure 6.11 – Results of the alignment after applying the Legendre polynomials correction and tacking into account the angle of the incoming particles for the back sensor: **??** $\Delta u = f(u_{hit})$ and 6.11d distribution of the residuals.

Side	Tilted angle	σ_U^{Def} (μm)	σ_U^{Cor} (μm)	Improvement
Front	28	9.0 $\pm$ 0.1	4.9 $\pm$ 0.1	46.6 %
Back	28	5.7 $\pm$ 0.1	4.7 $\pm$ 0.1	17.5 %
Front	36	14.1 $\pm$ 0.1	6.1 $\pm$ 0.1	56.0 %
Back	36	6.8 $\pm$ 0.1	5.9 $\pm$ 0.1	13.2 %
Front	60	41.2 $\pm$ 0.15	25.8 $\pm$ 0.2	37.4 %
Back	60	23.3 $\pm$ 0.13	21.7 $\pm$ 0.1	6.8 %

Table 6.2 – Alignment results for different angles before and after using the correction based on Legendre polynomials.

6.3 Benefits of double-sided measurement

As two modules are sharing the same mechanical structure, the information provided by each side can be combined together. A mini-vector is created by connecting two hits on each side of the ladder for the same event. This combination gives access to a new information compared to a single sensor: the angular resolution.

6.3.1 Spatial resolution with mini-vectors

To study the benefits of the mini-vector, a virtual intermediate plane is defined at the center of the ladder. The two hits of each side of the DUT are connected to form a mini-vector and the intersection of this vector to the intermediate plane is determined. The intersection of the extrapolated track to the intermediate plane is also performed and the distance between the position of the track and the position of the mini is then measured.

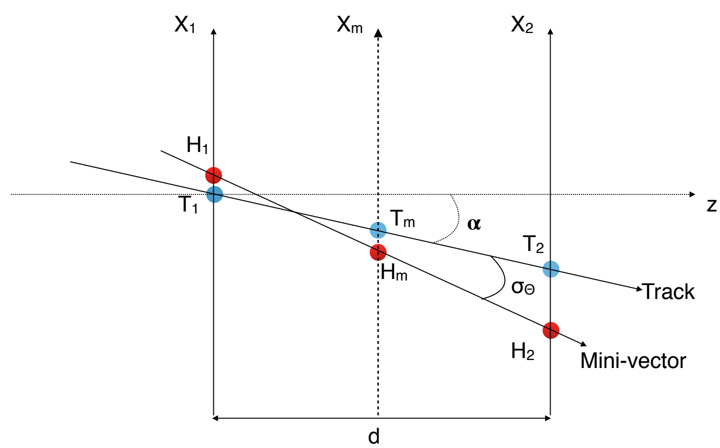

Figure 6.12 – Principle of the mini-vector. The two hits (in red) on the planes x_1 and x_2 are connected and the intersection on virtual intermediate plane x_m is then determined. The blue points represents the track extrapolated through the DUT.

A theoretical estimation of the spatial resolution for the mini-vector can be done thanks to the formula above:

$$\sigma_m^2 = \frac{\sigma_{front}^2 + \sigma_{back}^2}{(d_{front} - d_{back})^2} \cdot d_m^2 + \sigma_{tel}^2 \tag{6.6}$$

Where σ_m is the resolution on the intermediate plane, σ_{front} and σ_{back} are the resolution of the two sides of the DUT, σ_{tel} the resolution of the telescope and $(d_{front} - d_{back})$ the distance between the front and back planes and d_m^2

the position of the intermediate plane. For the plume ladder, the SiC as a thickness of 2 mm and the intermediate plane is located in the middle, the equation 6.6 can be rewritten:

$$\sigma_m^2 = \frac{\sigma_{front}^2 + \sigma_{back}^2}{4} + \sigma_{tel}^2 \tag{6.7}$$

Thus, if the resolution on both side of the telescope are similar with $\sigma_{front} = \sigma_{back} = \sigma$, the resolution of the mini-vector σ_{res} is then:

$$\sigma_{res} = \frac{\sigma}{\sqrt{2}} \tag{6.8}$$

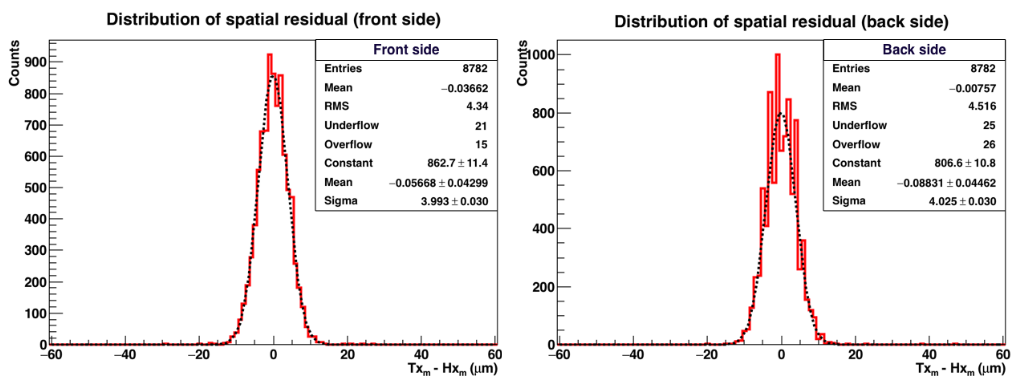

Figure 6.13 – Residual distribution for both side of the ladder in the u-direction

For a run in normal incidence, the spatial resolution measured on each side is $\sigma_{front} \simeq \sigma_{back} \simeq 4$ μm, according to the figure 6.13. The resolution of the mini-vector should be then $\sigma_{res} \simeq 2.8$ μm. The measurement of the residual for the mini-vector displayed on the figure 6.14 gives a residual of 3.2 μm. Taking into account the resolution of the telescope, the spatial resolution achieved by the mini-vector is $\sigma_{res} \simeq 2.9$ μm.

6.3.2 Angular resolution

The mini-vectors give an access to new information not provided by a single sensor, the angular resolution. The direction of the track can be compared to the direction of the mini-vector. The estimation of the angular resolution is given by:

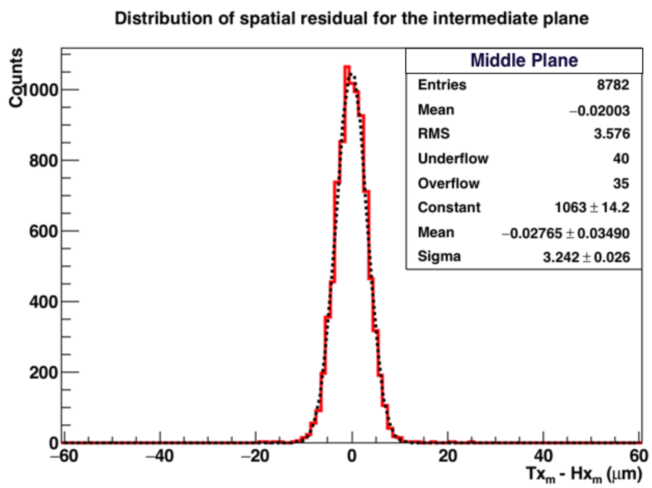

Figure 6.14 – Residual distribution of the mini-vector measured on the intermediate plane.

$$\sigma_{theta} = \frac{\sqrt{\sigma_{front}^2 + \sigma_{back}^2}}{d} \tag{6.9}$$

With σ_{front} and σ_{back} the spatial resolution on each side of the DUT in microns and d the distance between the two sides in microns. The spatial resolution here is $\sigma \simeq 3.6$ μm and the distance between the two planes 2000 microns. The angular resolution estimated is then $\sigma_\theta = 0.146°$.

The figure 6.15 depicts the distribution of the angle between the tracks direction and the mini-vectors direction. As it can be seen, several peaks are present and the distribution can't be extrapolated by a Gaussian fit. The sensors have a binary output and the hit position is determined by the centre-of-gravity of the clusters. If the cluster is only one pixel, the centre-of-gravity will be in the middle of the pixel, but if the clusters contain more pixels, this centre-of-gravity will be displaced. Moreover, they are some deviations in the distance between the hit projected to one side to the real hit position on this side. The figure 6.16 represents the minimum distance between one cluster on one side to the cluster on the other side.

Hence, for one pixel clusters, the displacement between the two pixels is the pitch $p = 18.4$ μm and the angle between the two minimal hit position is then $\theta \sim 0.52°$. A selection of the events where only clusters of 1 pixel are considered is shown on the figure 6.17a. The two peaks have a spacing

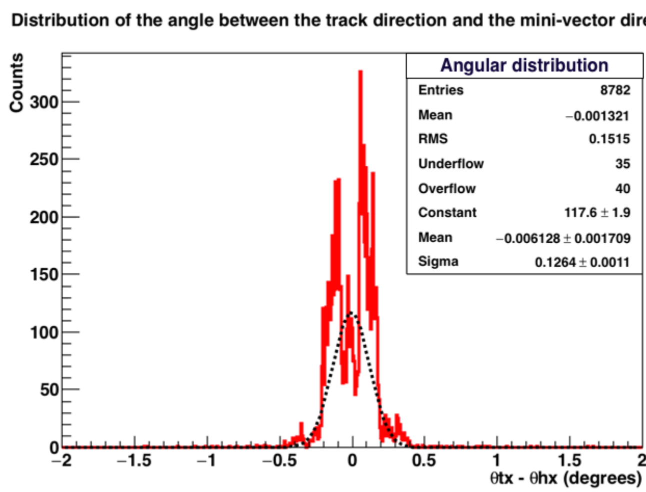

Figure 6.15 – Distribution of the angle between the tracks direction and the mini-vectors direction.

close to 0.5°. For clusters of 1×2 or 2×2 pixels, the distance between the two hit positions reconstructed via centre-of-gravity is half the pitch. Hence, the peaks are two times closer with a spacing of nearly 0.25°, as seen on the figures 6.17b and 6.17c. Nevertheless, for larger cluster sizes the angular distribution has only one peak around 0°.

6.4 Conclusions

Along this chapter, the test beam campaign done in November 2011 at CERN was discussed. The results were focused on the alignment procedure, as well as the performances of the ladder in normal and tilted positions. The runs in tilted position were challenging to align due to some deviations between the track-hit residual and the actual hit position on the plane. This has the effect of increasing the spatial residual measured. A higher pointing resolution is expected for bending tracks but in a smaller proportion. An algorithm using Legendre polynomials to describe the sensor's shape was discussed. The results obtained for small angles are close to the value expected for a single MIMOSA-26 sensor in normal incidence. Nevertheless, the pointing resolution depends strongly on the incidence angle. For 36° and higher, the correction is less efficient to achieve the normal performances. It might also be possible that the heating is increasing the deformation and that the cooling system could induce some vibrations which induce some deformation too.

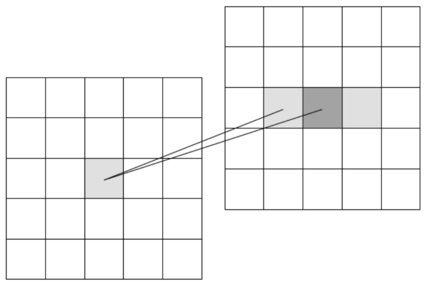

(a) One pixel per cluster.

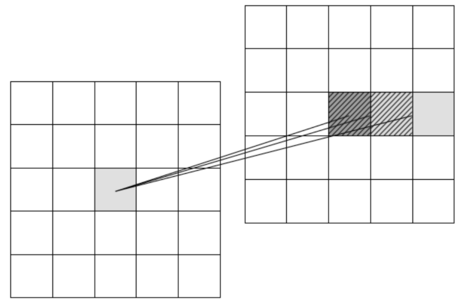

(b) 1×2 pixels per cluster.

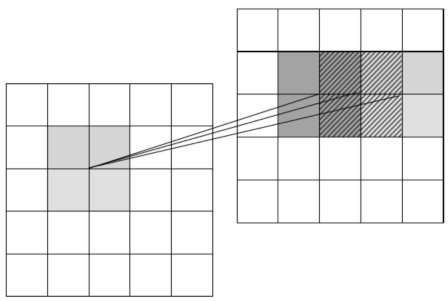

(c) 2×2 pixels per cluster.

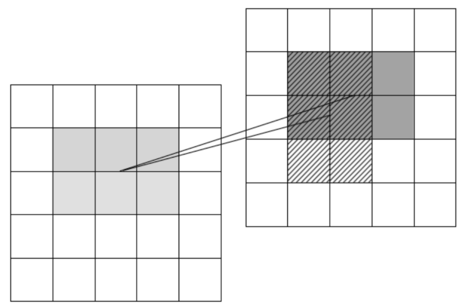

(d) 3×3 pixels per cluster.

Figure 6.16 – Minimum distance between the cluster projected on one side to the position of the cluster of this side.

Nevertheless, the results obtained here for different air flow speed can not lead to a conclusion on a possible impact of the cooling system.

The second part of this chapter was talking about the benefits of double-sided measurements. For normal incidence, the pointing resolution of the mini-vector, which is the combination of the pointing resolution on each side, is better than the spatial resolution of a single sensor. Moreover, the mini-vectors give access to another information: the angular resolution. Due to the binary output and the centre-of-gravity hit position reconstruction, multiple peaks are visible and a simple Gaussian fit can not be used. The same work has to be done with ladder titled with respect to the beam to study the impact of the deformation on the mini-vectors.

The first results obtained are encouraging the mechanical structure. Nevertheless, the material budget of the ladder is estimated theoretically. The next chapter will introduce a test beam performed at DESY in 2016 and will specifically talk about the measurement of the radiation length for a PLUME-V1 prototype.

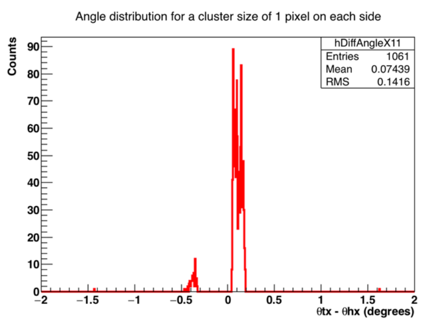

(a) One pixel per cluster.

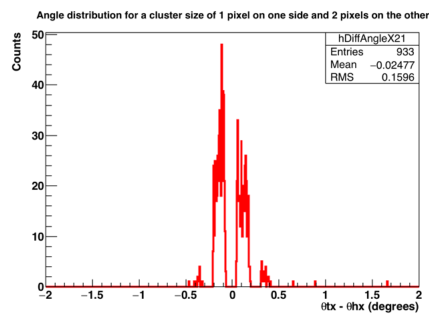

(b) 2×1 pixels per cluster.

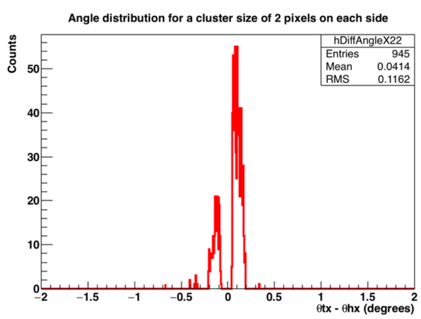

(c) 2×2 pixels per cluster.

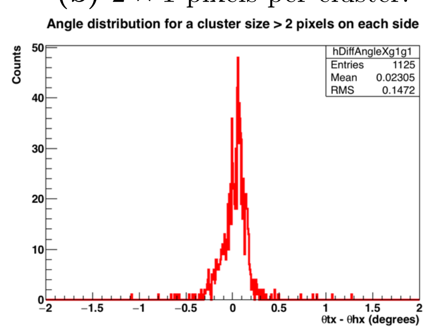

(d) Clusters bigger than 2×2 pixels.

Figure 6.17 – Minimum distance between the cluster projected on one side to the position of the cluster of this side.

Chapter 7

Determination of the material budget

The discovery of new physics and the characterisation of the already known particles is possible only with good detectors. As it was presented on the chapter 4, the fabrication of a vertex detector is constrained by two parameters: the pointing resolution and the material budget. The first fully functional prototype of PLUME was tested in November 2011 a CERN with 120 GeV pions. The results have shown that the pointing resolution of the ladder is correlating the expected value for the ILD and moreover, the use of a double-sided structure improves this pointing resolution. Nevertheless, the material budget ($X0$) of such device is estimated only by calculation and the beam provided by SPS does not allow to measure it. Therefore, a test beam campaign was done in April 2016 at DESY test beam 21 with positrons up to 5 GeV. The ladder which was tested is also the first prototype (PLUME-V1). The reason to test an already known prototype is that the performances have to be the same at low and high-momentum particles. The preparation of the test beam is firstly discussed. Then, the test beam facility, as well as the tools used for the analysis are presented. Finally, the radiation length measurements are shown.

Contents

7.1 Preparation of the test beam

A second test beam was performed in April 2016 at DESY with positrons up to 5 GeV. The goal of this test beam was to study the performance of this device with low-momentum particles. The ladder tested as a version-1, but not the one already tested at CERN. The steps, from the preparation to the analysis are explained here. Different measurements were planned to fully test the ladder. Nevertheless, as this test beam was at the end of my Ph. D., I could not perform all the measurements. The preparation are presented for all the measurements, but the analysis itself is focused only on the radiation length measurement.

7.1.1 Test beam preparation

The test beam last two weeks, hence several measurements were performed to completely test the ladder. The measurements scheduled were:

- Spatial resolution
- Mini-vectors
- deformation:
  - Tilt up to 60°
  - Air flow speed between 3 and 5 m.s^{-1}
- radiation length

To get the best telescope pointing resolution, the inner planes of the telescope have to be as closed as possible to the DUT. Nevertheless, to perform the deformation measurements and to avoid to move the telescope planes and perform again the alignment later, the two inner planes have a distance of .... Due to the design of the box, on which the ladder is not centered, the distance between the upstream inner plane and the box is different from the distance between the down stream inner plane and the box.

For the first time, the collaboration has decided to use the EUDET telescope and EUDAQ for the acquisition, instead of the Strasbourg telescope and the IPHC acquisition. Several solutions were available. The first one consists to use the six telescope planes of EUDET and a separate acquisition for PLUME. As the acquisition is limited to six inputs and the ladder requires at least one sensor on each side to be acquired, a solution to merge the

Energy	σ_{res} (μm)	
	4 planes	6 planes
2	4.85	4.78
3	3.79	3.83
4	3.35	3.40
5	3.12	3.15
6	2.98	2.99

Table 7.1 – Estimation of the resolution measured σ_{res} at the DUT position for a telescope with four planes and six planes.

data has to be thought. As the EUDET telescope and PLUME are equipped with the same sensors, the acquisition can be simplified by having only four telescope planes and connecting directly two sensors of DUT. A simulation tool was used to define which configuration is giving the best pointing resolution at the DUT positions. This toolkit was developed by Simon Spannagel and is based on GBL. For different energy, the resolution at the PLUME position was calculated for a set-up with four telescope planes and a set-up with six. The material budget of the DUT is determined by the material budget of PLUME plus two kapton foils used to insulate the ladder from light. For both configuration, the telescope is made of two arms on each side of the DUT. With six sensors, the maximal distance between each plane of one frame is $d_{\text{max}} = 150$ mm, whereas for the four sensors configuration it is $d_{\text{max=300 mm}}$.

The results shown on figure 7.1 depicts the measured resolution at the position of the DUT as a function of the distance between two telescope planes of the same arm.

7.1.2 experimental set-up

- beam structure
- telescope
- Fan

7.1.3 Software analysis

Due to the specific acquisition which was done with EUDAQ, the analysis was a bit complicated. EUTelescope was coded to expect six telescope planes plus

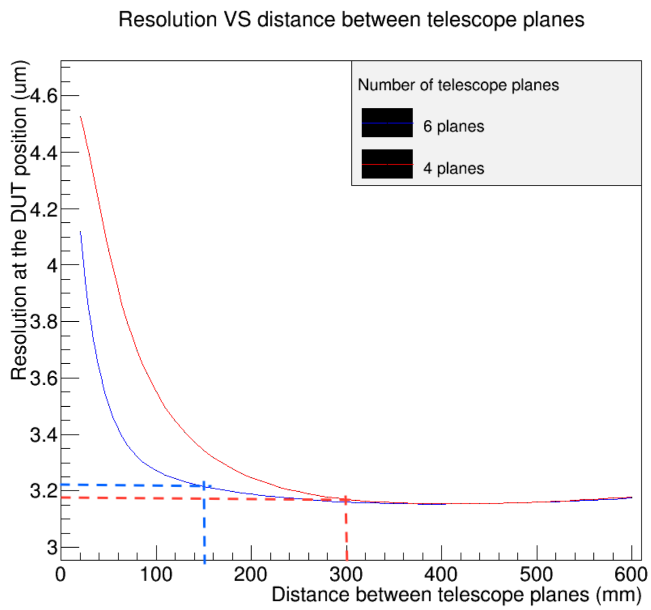

Figure 7.1 – Estimation of the resolution measured at the DUT position as a function of the distance between two telescope planes of the same arm. The blue lines is the results for six planes, whereas the red line is for four planes. The dashed lines are the maximal distance between two planes due to the rail limitation of the telescope frame.

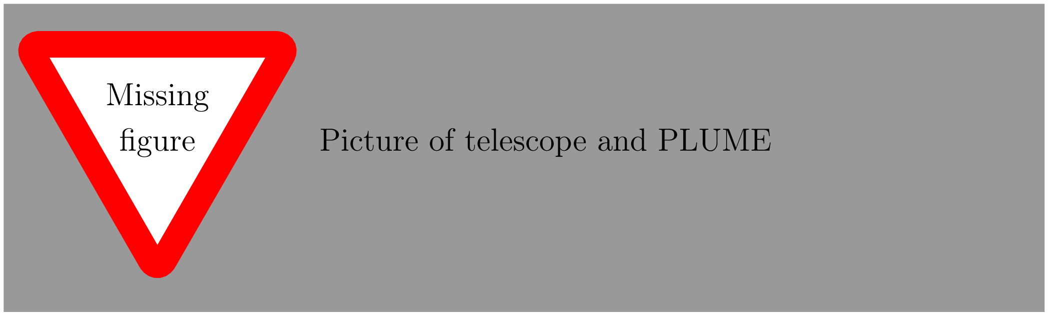

a single DUT. One way to overcome this problem was to perform a biased analysis. Instead of performing the alignment of the telescopes and then the DUT for an analysis, this step has to be done in one way. Nevertheless, the alignment procedure was not working.

To perform the alignment, I have used a python script written by Claus Kleinwort, which reads the hit position of every sensor and use GBL and MP-II to perform the alignment.

Acronyms

AHCAL Analogue HCAL. 36

APS Active Pixel Sensor. 53

ASIC Application-Specified Integrated Circuit. 53

BDS Beam Delivery System. 25

CCD Charged Coupled-Device. 52

CDS Correlated Double Sampling. 66

CLIC Compact LInear Collider. 24

CMOS Complementary Metal Oxide Semi-conductor. 49

DAQ Data AcQuisition. 54

DC Direct-current. 25

DEPFET Depleted P- Channel Field Effect Transistor. 53

DUT Device Under Test. 90

ECAL Electromagnetic CALorimeter. 33

EM electromagnetic interaction. 1

ETD End-cap Tracking Detector. 33

FPCCD Fine Pixels Charged Coupled-Device. 52

FPN Fixed Pattern Noise. 65

FTD Forward Tracking Detector. 33

GEAR GEometry Api for Reconstruction. 46

GRPC Glass Resistive Plate Chamber. 36

HCAL HAdronic CALanalogue HCALorimeter. 35

ILC International Linear Collider. 24

ILD International Large Detector. 21

IP interaction point. 28

IR interaction region. 25

ISR Initial State Radiation. 46

LCIO Linear Collider I/O. 45

LHC Large Hadron Collider. 19

LHCAL Low angle Hadron CALorimeter. 36

MAPS Monolithic Active Pixel Sensor. 35

Marlin Modular Analysis and Reconstruction for the LINear collider. 46

MIMOSA Minimum Ionizing MOS Active pixel sensor. 53

MIP Minimum Ionizing Particle. 60

OKF Optiprint-Kapton-Flex-cable. 56

PFA Particle Flow Algorithm. 30

PLUME Pixelated Ladder with Ultra-low Material Embedding. 49

QCD Quantum Chromodynamics. 8

QED Quantum Electrodynamic. 5

QFT Quantum Field Theory. 5

RTML Ring To the Main Linac. 26

SDHCAL Semi-Digital HCAL. 36

SET Silicon External Tracking. 33

SiC Silicon Carbide. 55

SiD Silicon Detector. 30

SIT Silicon Internal Tracker. 33

SM Standard Model. 2

SNR Signal to Noise ratio. 66

SRF Superconducting Radio-Frequency. 24

SUZE Suppression de zéro. 65

TAF TAPI Analysis Framework. 85

TN Temporal Noise. 65

TPC Time-Projection-Chamber. 30

VXD Vertex Detector. 31

ZIF Zero Insertion Force. 55

Bibliography

[1] Alignment of the CMS tracker with LHC and cosmic ray data. pages 1748–221, 1088.

[2] DEPFET Pixels as a Vertex Detector for the Belle II Experiment. 2013.

[3] Georges Aad et al. Observation of a new particle in the search for the Standard Model Higgs boson with the ATLAS detector at the LHC. *Phys. Lett.*, B716:1–29, 2012.

[4] R. Appleby, L. Keller, T. Markiewicz, A. Seryi, R. Sugahara, and D. Walz. The International Linear Collider Technica. 3, 2006.

[5] D. M. Asner, T. Barklow, C. Calancha, K. Fujii, N. Graf, H. E. Haber, A. Ishikawa, S. Kanemura, S. Kawada, M. Kurata, A. Miyamoto, H. Neal, H. Ono, C. Potter, J. Strube, T. Suehara, T. Tanabe, J. Tian, K. Tsumura, S. Watanuki, G. Weiglein, K. Yagyu, and H. Yokoya. ILC Higgs White Paper. page 152, oct 2013.

[6] H Baer, T Barklow, K Fujii, Y Gao, and a Hoang. [1306.6352] The International Linear Collider Technical Design Report - Volume 2: Physics. *... preprint arXiv:13066352*, 2, jun 2013.

[7] M. Battaglia. Vertex tracking at a future linear collider. *Nucl. Instruments Methods Phys. Res. Sect. A Accel. Spectrometers, Detect. Assoc. Equip.*, 650(1):55–58, sep 2011.

[8] Jerome Baudot, Olena Bashinska, Nathalie Chon-Sen, Wojciech Dulinski, Franziska Hegner, Marie Gelin-Galibel, Rhorry Gauld, Mathieu Goffe, Joel Goldstein, Ingrid Gregor, Christine Hu-Guo, Ulrich Koetz, Andrei Nomerotski, and Marc Winter. Development of Single- and Double-sided Ladders for the ILD Vertex Detectors. mar 2012.

[9] T. Behnke, J. E. Brau, B. Foster, J. Fuster, M. Harrison, J. P. Paterson, M. Peskin, M. Stanitzki, N. Walker, and H. Yamamoto. ILC Technical Design Report Volume 1: Executive Summary. *ILC Tech. Des. Rep. Vol. 1 Exec. Summ.*, 1:1–60, 2013.

[10] Ties Behnke. The international linear collider. *Fortschritte der Phys.*, 58(7-9):622–627, 2010.

[11] Constantino Calancha Paredes, A Dubey, H Ikeda, A Ishikawa, S Ito, E Kato, A Miyamoto, T Mori, H Sato, T Suehara, Y Sugimoto, and H Yamamoto. Progress in the development of the vertex detector with fine pixel CCD at the ILC.

[12] Serguei Chatrchyan et al. Observation of a new boson at a mass of 125 GeV with the CMS experiment at the LHC. *Phys. Lett.*, B716:30–61, 2012.

[13] Donut Collaboration, K Kodama, N Ushida, C Andreopoulos, N Saoulidou, G Tzanakos, P Yager, B Baller, W Freeman, B Lundberg, J Morrn, R Rameika, J C Yun, J S Song, C S Yoon, S H Chung, P Berghaus, M Kubanstev, N W Reay, R Sidwell, N Stanton, S Yoshida, S Aoki, T Hara, and J T Rhee. Observation of Tau Neutrino Interactions. 2000.

[14] A. Denner, S. Heinemeyer, I. Puljak, D. Rebuzzi, and M. Spira. Standard Model Higgs-Boson Branching Ratios with Uncertainties. *Eur. Phys. J.*, C71:1753, 2011.

[15] Deutsches Elektronen-synchrotron Desy and Hamburg Germany. A review of e+ e- Linear Colliders. 22:529–539, 1988.

[16] M Deveaux, S Amar-Youcef, A Besson, G Claus, C Colledani, M Dorokhov, C Dritsa, W Dulinski, I Fröhlich, M Goffe, D Grandjean, S Heini, A Himmi, C Hu, K Jaaskelainen, C Müntz, A Shabetai, J Stroth, M Szelezniak, I Valin, and M Winter. Radiation Tolerance of CMOS Monolithic Active Pixel Sensors with Self-Biased Pixels. 2009.

[17] F. Englert and R. Brout. Broken Symmetry and the Mass of Gauge Vector Mesons. *Physical Review Letters*, 13:321–323, August 1964.

[18] ˜a R Erwin, R H March, W D Walker, M Goldhaber, T D Lee, C N Yang, G Danby, J-M Gaillard, K Goulianos, L M Lederman, N Mistry, M Schwartz, and Z Steinbergert. OBSERVATION OF HIGH-ENERGY NEUTRINO REACTIONS AND THE EXISTENCE OF TWO KINDS OF NEUTRINOS. *Phys. Rev. Phys. Rev. Phys. Rev. Lett.*, 9(6):101–1640, 1961.

[19] E. Fermi. An attempt of a theory of beta radiation. 1. *Z. Phys.*, 88:161–177, 1934.

[20] R. P. Feynman and M. Gell-Mann. Theory of the fermi interaction. *Phys. Rev.*, 109:193–198, Jan 1958.

[21] Y. Fukuda, T. Hayakawa, E. Ichihara, K. Inoue, K. Ishihara, H. Ishino, Y. Itow, T. Kajita, J. Kameda, S. Kasuga, K. Kobayashi, Y. Kobayashi, Y. Koshio, M. Miura, M. Nakahata, S. Nakayama, A. Okada, K. Okumura, N. Sakurai, M. Shiozawa, Y. Suzuki, Y. Takeuchi, Y. Totsuka, S. Yamada, M. Earl, A. Habig, E. Kearns, M. D. Messier, K. Scholberg, J. L. Stone, L. R. Sulak, C. W. Walter, M. Goldhaber, T. Barszczxak, D. Casper, W. Gajewski, P. G. Halverson, J. Hsu, W. R. Kropp, L. R. Price, F. Reines, M. Smy, H. W. Sobel, M. R. Vagins, K. S. Ganezer, W. E. Keig, R. W. Ellsworth, S. Tasaka, J. W. Flanagan, A. Kibayashi, J. G. Learned, S. Matsuno, V. J. Stenger, D. Takemori, T. Ishii, J. Kanzaki, T. Kobayashi, S. Mine, K. Nakamura, K. Nishikawa, Y. Oyama, A. Sakai, M. Sakuda, O. Sasaki, S. Echigo, M. Kohama, A. T. Suzuki, T. J. Haines, E. Blaufuss, B. K. Kim, R. Sanford, R. Svoboda, M. L. Chen, Z. Conner, J. A. Goodman, G. W. Sullivan, J. Hill, C. K. Jung, K. Martens, C. Mauger, C. McGrew, E. Sharkey, B. Viren, C. Yanagisawa, W. Doki, K. Miyano, H. Okazawa, C. Saji, M. Takahata, Y. Nagashima, M. Takita, T. Yamaguchi, M. Yoshida, S. B. Kim, M. Etoh, K. Fujita, A. Hasegawa, T. Hasegawa, S. Hatakeyama, T. Iwamoto, M. Koga, T. Maruyama, H. Ogawa, J. Shirai, A. Suzuki, F. Tsushima, M. Koshiba, M. Nemoto, K. Nishijima, T. Futagami, Y. Hayato, Y. Kanaya, K. Kaneyuki, Y. Watanabe, D. Kielczewska, R. A. Doyle, J. S. George, A. L. Stachyra, L. L. Wai, R. J. Wilkes, and K. K. Young. Evidence for oscillation of atmospheric neutrinos. *Phys. Rev. Lett.*, 81:1562–1567, Aug 1998.

[22] Steven Green, John Marshall, Mark Thomson, and Boruo Xu. Cambridge linear collider group - home page. http://www.hep.phy.cam.ac.uk/linearcollider/calorimetry/.

[23] Peter W. Higgs. Broken symmetries and the masses of gauge bosons. *Phys. Rev. Lett.*, 13:508–509, Oct 1964.

[24] ICFA. Final International Technology Recommendation Panel Report. (September), 2004.

[25] Ilcsoft homepage. http://ilcsoft.desy.de. Accessed: 2010-09-30.

[26] IPHC. *MIMOSA26 User Manual*.

[27] Jérôme Baudot. TAF short manual. 2015.

[28] Oleg Kuprash. Power pulsing of the CMOS sensor Mimosa 26. *Nucl. Instruments Methods Phys. Res. Sect. A Accel. Spectrometers, Detect. Assoc. Equip.*, 732:519–522, 2013.

[29] Lcio homepage. http://lcio.desy.de.

[30] T. D. Lee and C. N. Yang. Question of Parity Conservation in Weak Interactions. *Physical Review*, 104:254–258, October 1956.

[31] Yiming Li, Chris Damerell, Rui Gao, Rhorry Gauld, Jaya John John, Peter Murray, Andrei Nomerotski, Konstantin Stefanov, Steve Thomas, Helena Wilding, and Zhige Zhang. ISIS2: Pixel Sensor with Local Charge Storage for ILC Vertex Detector. page 11, jun 2010.

[32] Ronald Lipton. Muon Collider: Plans, Progress and Challenges. page 6, apr 2012.

[33] Cousin Loïc. Trajectométrie dans le cadre du projet européen aida, 2015.

[34] O. Markin. Backgrounds at future linear colliders. feb 2014.

[35] A Nomerotski, L Bachynska, J Baudot, N Chon-Sen, G Claus, R De Masi, M Deveaux, W Dulinski, R Gauld, M Goffe, J Goldstein, I.-M Gregor, Ch Hu-Guo, M Imhoff, U Koetz, W Lau, C Muntz, C Santos, C Schrader, M Specht, J Stroth, M Winter, and S Yang. PLUME collaboration: Ultra-light ladders for linear collider vertex detector.

[36] K. A. Olive et al. Review of Particle Physics. *Chin. Phys.*, C38:090001, 2014.

[37] PLUME project. http://www.iphc.cnrs.fr/PLUME.html.

[38] RH Richter, L Andricek, P Fischer, K Heinzinger, P Lechner, G Lutz, I Peric, M Reiche, G Schaller, M Schnecke, F Schopper, H Soltau, L Str uder, J Treis, M Trimpl, J Ulrici, and N Wermes. Design and technology of DEPFET pixel sensors for linear collider applications. *Nucl. Instruments Methods Phys. Res. A*, 511:250–256, 2003.

[39] Maria Robert. Study of the time-dependent cp asymmetry in d^0 decays in the belle ii experiment, 2015.

[40] Adrian Signer. ABC of SUSY. *Journal of Physics G: Nuclear and Particle Physics*, 36(7):073002, jul 2009.

[41] The standard model of particle physics. http://www.brighthub.com/science/space/articles/84750.aspx.

[42] Junping Tian and Keisuke Fujii. Measurement of Higgs couplings and self-coupling at the ILC. *Eur. Phys. Soc. Conf. High Energy Phys.*

[43] Marc Winter. Development of Swift, High Resolution, Pixel Sensor Systems for a High Precision Vertex Detector suited to the ILC Running Conditions. 2009.

[44] C. S. Wu, E. Ambler, R. W. Hayward, D. D. Hoppes, and R. P. Hudson. Experimental Test of Parity Conservation in Beta Decay. *Physical Review*, 105:1413–1415, February 1957.